CELLULAR AND SUBCELLULAR LOCALIZATION OF MERCAPTOUNDECAHYDRO-*CLOSO*-DODECABORATE (BSH) IN HUMAN GLIOBLASTOMA MULTIFORME

Dissertation

zur Erlangung des Doktorgrades der Naturwissenschaften

- Dr. rer. nat. -

vorgelegt dem Promotionsausschuss

des Fachbereichs 2 (Biologie/Chemie) der Universität Bremen

von

Michael Neumann

Universität Bremen

2001

ACKNOWLEDGEMENTS

I wish to express my sincere gratitude to:

- Professor Detlef Gabel, my scientific supervisor, who gave me his excellent guidance, helpfulness and encouragement.
- Prof. Dr. Dietmar Beyersmann, Prof. Dr. Sørge Kelm and Prof. Dr. Reimer Stick for rating this work.
- Ulrike Kuntz, Prof. Dr. Heiner Lehmann, Dr. Benjamin Gilbert and Prof. Dr. Gelsomina De Stasio for fruitful collaboration.
- Dr. Martin Kölling and Dr. Fabian Fehlauer for helpful support and cooperation.
- all my friends.
- and most of all Juliane Steffen for never-ending support, understanding and encouragement.

CONTENTS

1 SUMMARY

During this study the cellular and subcellular distribution of mercaptoundecahydro-*closo*-dodecaborate (BSH) were investigated in glioblastoma multiforme tissue sections of seven patients, whom having received BSH prior to surgery. To achieve this, several microscopic techniques were used. Direct detection of boron was performed by x-ray photoelectron emission spectromicroscopy (X-PEEM), electron energy loss spectroscopy (EELS) and electron spectroscopic imaging (ESI). For visualization of BSH in light-, fluorescence microscopy and transmission electron microscopy (TEM) antibodies against BSH were used.

These microscopic techniques show that BSH is associated with the cell membrane as well as with the chromatin in the nucleus. With use of specific antibodies against different tumor specific epitopes, BSH could be found predominantly (approx. 90 %) in the cytoplasm of GFAP-positive cells of all but two patients. The latter were significantly younger (33 and 38 years versus to 46-71 (mean 60) years). Based on the expression of EGFR and p53, the tumors of five patients could be characterized as primary or secondary glioblastoma. Although the tissue regions of EGFR and p53 overexpression do not seem to correspond with the regions of high BSH uptake, mutations during tumor development could be the reason for the distinct accumulation of BSH. No direct correlation between BSH uptake and expression of CD44, vWF, laminin and Ki-67 has been observed.

By x-ray photoelectron emission spectromicroscopy boron was found in a reduced chemical state (with respect to boron in BSH). The reduced boron species was found in tissue in the same general areas, which stained positive for BSH in light microscopy. The present work presents for the first time evidence that a proportion of the BSH injected into the patient could have been bound or metabolized *in vivo*.

Additionally, during optimization of immunohistochemistry in this work, a new method for reduction of autofluorescence in aldehyde-fixed tissue could be found. Background fluorescence can be notably reduced by irradiation with light before treatment with fluorescence probes, resulting in a higher contrast without adversely affecting the staining probabilities.

2 INTRODUCTION

2.1 GLIOBLASTOMA MULTIFORME (GBM)

Primary tumors of the central nervous system are the fifth most common primary neoplasm, with an average incidence of about five cases per 100000 population and year (Bondy and Wrensch, 1993; Lantos et al., 1996). Approximately 50 % of these tumors are astrocytomas (Collins, 1993), which are divided into two basic categories: circumscribed (grade I) or diffuse (grades II, III, and IV). Grade I tumors do not share the inherent tendencies of other gliomas to progress to tumors of higher grade (Bailey and Cushing, 1972). Within the diffuse astrocytomas, the specific criteria differentiate between the less biologically aggressive forms (grades II and III) and GBM (grade IV). Regardless of their grade at the time of diagnosis, all diffuse astrocytomas tend to progress to GBM (grade IV) (Kleihues and Cavenee, 1997). Criteria used to distinguish grade IV lesions include marked neovascularity, variable mitotic activity, increased cellularity, nuclear pleomorphism, and microscopic evidence of necrosis. One common and distinctive histopathologic feature of GBM is pseudopalisading (Fig. 1), in which areas of viable neoplastic cells form an irregular border surrounding areas of necrotic debris. This feature is indicative of the uncontrolled growth within the tumor.

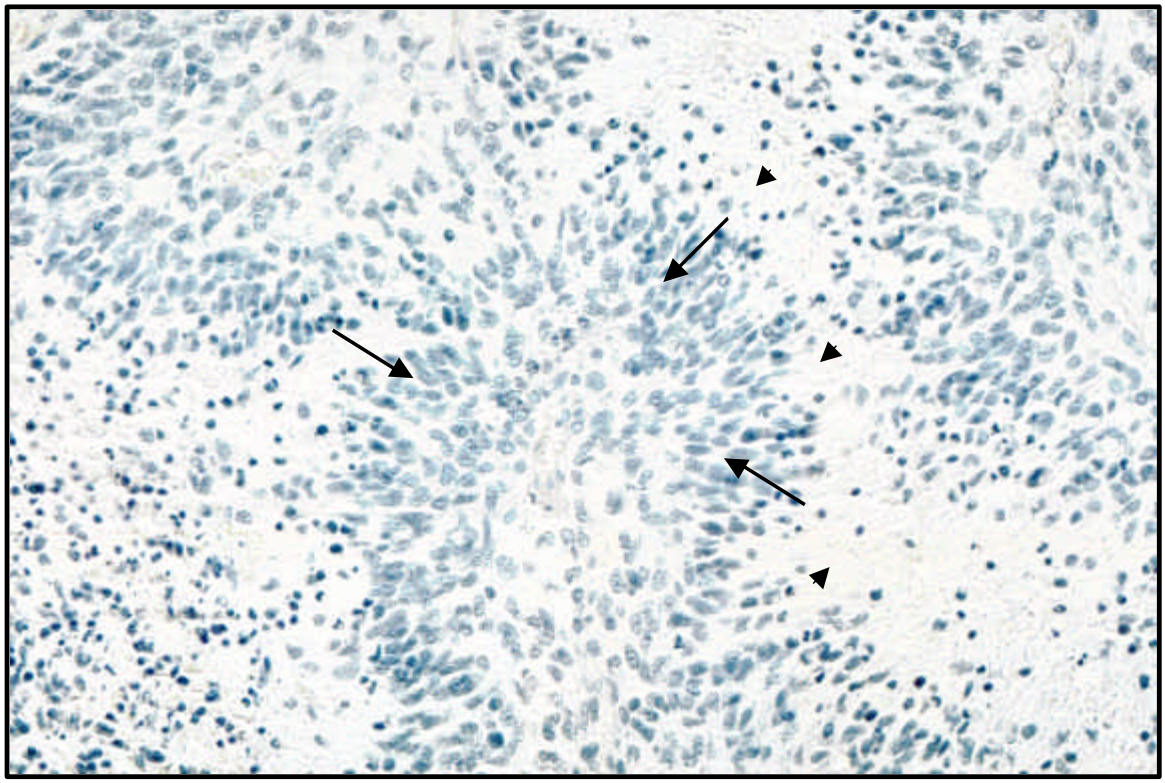

Fig. 1: Photomicrograph (Patient BE, hematoxylin stain) of a typical GBM shows a ring of viable tumor cells (straight arrows) bordering on areas of necrosis (arrowheads), referred to as pseudopalisading.

Fifty percent of the astrocytomas are classified as glioblastoma multiforme (Bruner, 1994). In spite of the fact that it represents only 1 % - 2 % of all malignancies, GBM is diagnosed in 15000 - 20000 patients per year (Boring et al., 1993).

Although GBM has been reported in patients of all age groups, it is most common in late adulthood, with a peak prevalence between 45 and 70 years of age (Mao et al., 1991; Kleihues and Cavenee, 1997). There is a slight male predilection for GBM (3:2) (Zulch, 1986) and it occurs more commonly in whites than in persons of African, Asian, or Latin American descent (Radhakrishnan et al., 1994).

The greatest morbidity and mortality from GBM is caused by local growth and direct extension from the site of origin within the brain (Vertosick and Selker, 1990). Despite the term “glioblastoma multiforme”, current neuropathologic theory is, that GBMs arise from the progressive dedifferentiation of mature cells, rather than from persistent embryonic cells or glioblasts. Frequently, this transformation occurs within a preexisting low-grade astrocytoma (Kleihues et al., 1993; Lang et al., 1994). Both genetic and histopathologic data support the concept of a stepwise increase in degree of malignancy from low-grade glioma to high-grade glioma, culminating in the GBM (Debiec-Richter and Liberski, 1994; Louis and Seizinger, 1994; Steck et al., 1993) (Fig. 2). Current research indicates that different genetic lesions are responsible for primary (de novo) GBM, compared with secondary GBM that arises in a preexisting glioma (Watanabe et al., 1996).

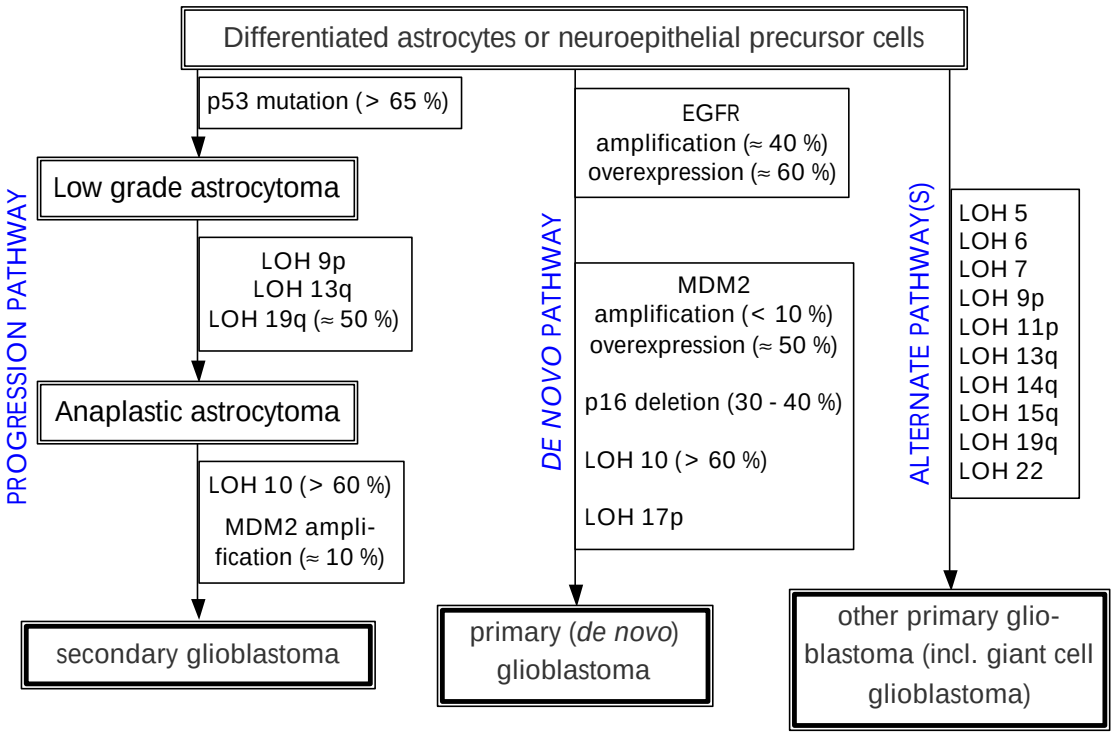

Fig. 2: Pathways leading to glioblastoma [modified from Lang et al., 1994 and Kleihues and Ohgaki, 1997].

The term oncogene is used to describe genes that encode for proteins that directly promote neoplastic transformation and stimulate tumor growth. These abnormal genes may occur from a mutation or may be inherited. Tumor suppressor genes on the other hand, are normal genes present in most people. They encode for proteins that control the growth of normal tissues and prevent neoplastic growth and transformation. Either the absence of a tumor suppressor gene or the mutation into an oncogene can lead to increased prevalence of neoplasms in various body tissues. Both oncogenes and malfunctioning tumor suppressor genes have been identified in patients with GBMs (Finlay et al., 1989; Lang et al., 1994).

One of the best-studied tumor suppressor genes is p53, which is located on the short arm of chromosome 17 (Lang et al., 1994). An abnormal p53 gene has been implicated in a wide variety of tumors throughout the body and studies have shown that at least 40 % of GBMs have this mutation (Wu et al., 1993; Posner, 1995). Because an abnormal p53 gene seems to be more common in higher-grade astrocytomas, it is thought to contribute to the natural progression of low-grade to higher-grade astrocytomas (Haapasalo et al., 1993). There is also evidence that it plays a role in the initial neoplastic transformation of a normal glial cell into an astrocytoma. In vitro studies have demonstrated partial growth stoppage in GBM after insertion of a normal p53 gene into GBM cells (Van Meir et al., 1995) and after direct administration of normal p53 protein to GBM cell colonies. Many other tumor suppressor gene mutations and oncogenes have been identified and there is a direct relationship between the number and degree of detectable genetic abnormalities and the type and grade of the glioma (James et al., 1988; Lang et al., 1994; Kleihues and Ohgaki, 1997). One specific pathway for the development of GBM involves mutation of p53 at the astrocytoma stage; loss of tumor suppressor genes on chromosomes 9, 13, or 19 to produce an anaplastic astrocytoma; and subsequent loss of tumor suppressor genes on chromosome 10 in the transformation to a GBM (Westermark and Nister, 1995) (Fig. 2). Although not as well studied as p53 mutation, allelic loss from chromosome 10 appears to be the most common genetic lesion in GBM and is found in up to 80 % of specimens (Rasheed et al., 1992). Unlike p53 mutation, chromosome 10 damage does not appear to be common in other tumors in the body nor in lower grades of glioma, a finding that suggests it may be specific for GBM (Ransom et al., 1992).

Current research suggests that primary GBM, which arises de novo, may have a genetic basis different from that of secondary GBM, which arises within a preexisting lower grade glioma (Lang et al., 1994; Watanabe et al., 1996). The overexpression of epidermal growth factor receptor (EGFR) appears to occur in the absence of p53 mutations in 80 - 90% of GBMs that are clinically considered likely to be primary (Lang et al., 1994).

An important consequence of the histologic variations seen within infiltrative astrocytomas is the lack of correlation between the radiologic or even the gross pathologic margin of the tumor and the true margins of the area of neoplastic infiltration. Studies of tumor angiogenesis have shown that the tumor cells secrete various substances, including vascular

endothelial growth factor (Plate et al., 1994) and renin (Ariza et al., 1988), which induce the rapid growth of new blood vessels. These new tumor-induced vascular channels are structurally abnormal and to varying degrees lack the normal blood-brain barrier. This characteristic leads to transudation of fluids and protein into the extracellular space (Plate et al., 1994).

Initial treatment of GBM involves surgical resection and debulking of the tumor. Surgery is usually followed by radiation therapy and various forms of chemotherapy. Radiation treatment may be administered as whole-brain irradiation, focused beam therapy, or brachytherapy (Kortmann et al., 1998). Chemotherapeutic response is optimized with use of multiple drug combinations, although some single-drug regimens are nearly as effective (Valk et al., 1988).

After decades of intensive research, GBMs are still extremely resistant to all current forms of therapy (Barth et al., 1999). The average life span of the patient who undergoes treatment with surgery, radiation, and chemotherapy from time of diagnosis is estimated at 16 - 18 months (Salcman, 1980) and the 5-year survival rate of patients with GBMs in the USA is less than 1 % (Davis et al., 1998). Without therapy, average survival is less than six months.

2.2 BORON NEUTRON CAPTURE THERAPY (BNCT)

The aggressive behavior of glioblastoma multiforme and the resistance against common radiation- and chemotherapy forms make the search for a successful therapy an important task.

Limited clinical trials of adjunctive gene therapy have been performed; in these trials, antigenic viral particles (primarily herpes simplex virus type 1) are inserted into neoplastic tissue in attempt to induce a host immune response against the tumor (Mineta et al., 1995). These attempts have met with some limited success, as has the use of interleukin therapy to activate killer T cells and thereby increase the role of cell-mediated immunity in the host (Rosenberg et al., 1987).

Boron neutron capture therapy is an approach of radiation therapy. Due to its binary model it could be possible to destroy tumor cells while minimizing damage to healthy tissue. It is based on the nuclear reaction that occurs when boron-10 is irradiated with low-energy neutrons. The ^{10}B-nucleus undergoes a neutron capture reaction and disintegrates into two fission particles ($^{10}B(n,\alpha)^{7}Li$) (Taylor et al., 1935) (Fig. 3) with a range of approximately one cell radius (Northcliffe and Schilling, 1970). When these particles hit cell nuclei they can cause severe damage which lead to cell death. The inherent advantage of binary therapies over radiotherapy and over chemotherapy is that neither the radiation nor the compound alone is toxic. Only the combination of boron-10 and thermal neutrons in the same cell lead to cell death. The stable isotope ^{10}B, which is present in natural boron to 20 %, has a high efficiency of capturing neutrons. The main elements that occur in human tissue (hydrogen, nitrogen, carbon, oxygen) have much smaller cross sections for thermal neutrons (Table 1).

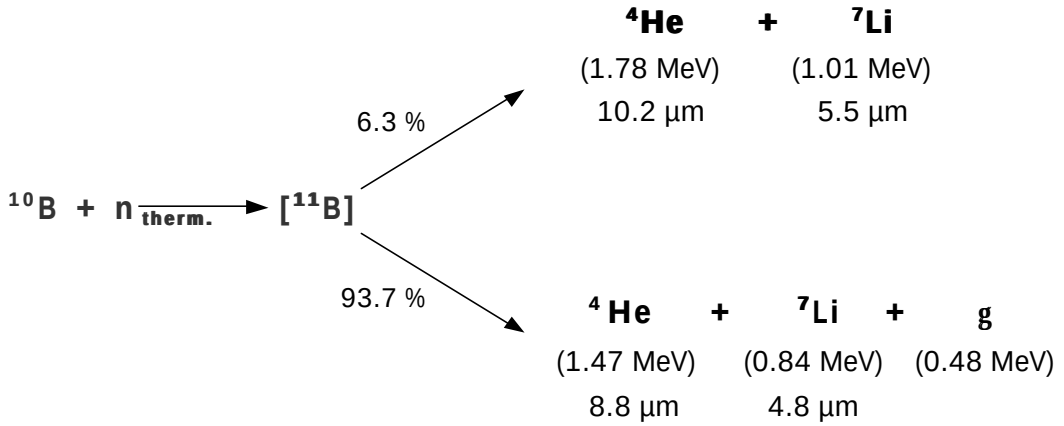

Fig. 3: The boron neutron capture reaction occurs when boron-10 is irradiated with low-energy neutrons ($n_{therm.}$) to yield an unstable boron-11, which disintegrates into high-energetic helium-4 and lithium-7 nuclei. The energy and range of each particle is shown below each of the reaction products (from Northcliffe and Schilling, 1970).

Isotope	Natural abundance [%]	Cross section [barn]	Reaction
^{10}B	19.61	3837	$^{10}B(n,\alpha\gamma)^{7}Li$ $^{10}B(n,\alpha)^{7}Li$
^{14}N	99.64	1.83	$^{14}N(n,p)^{14}C$
^{16}O	99.76	$1.8 * 10^{-4}$	$^{16}O(n,\alpha)^{17}O$
^{1}H	99.99	0.33	$^{1}H(n,\gamma)^{2}H$
^{12}C	98.89	$3.4 * 10^{-3}$	$^{12}C(n,\gamma)^{13}C$
^{13}C	1.11	$9 * 10^{-4}$	$^{13}C(n,\gamma)^{14}C$

Table 1: Cross-sections and capture reactions of several physiological relevant nuclides compared to boron-10 [from Northcliffe and Schilling, 1970].

For a successful treatment, it is required that the boron compounds possess the following properties (Barth et al., 1999):

- selectively target tumor versus normal cells, preferably with intracellular localization near at the cell nucleus
- attain cellular concentrations of about 10^9 boron-10 atoms/cell or about 20 - 35 µg/g tumor (Javid et al., 1952)
- achieve tumor-to-normal tissue ratios in excess of 3 to 4:1
- persist at constant concentrations in the tumor during the radiation procedure
- be sufficient non-toxic to attain adequate in vivo tumor concentrations

To date, two low-molecular weight boron compounds have been identified that possess some of the requisite properties for BNCT: Mercaptoundecahydro-*closo*-dodecaborate (2-) (BSH) and L-4-dihydroxyborylphenylalanine (BPA) (Fig. 4) (Hawthorne, 1998). BPA also has been used as a capture agent for BNCT of cutaneous melanomas (Mishima et al., 1989; Mishima, 1996).

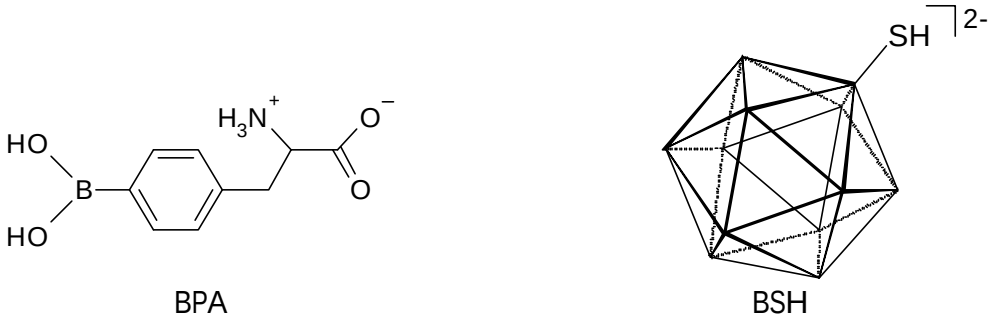

BPA BSH

Fig. 4: L-4-dihydroxyborylphenylalanine und Mercaptoundecahydro-*closo*-dodecaborate (2-). At each corner of the BSH cage is a BH-group located with exception of the one corner where the hydrogen is substituted by a mercapto-group. For clearness the boron and hydrogen atoms are not shown.

BSH has been established as a suitable boron carrier and has been used by Hatanaka et al. since 1968 with encouraging success (Hatanaka and Nakagawa, 1994) (Fig. 5).

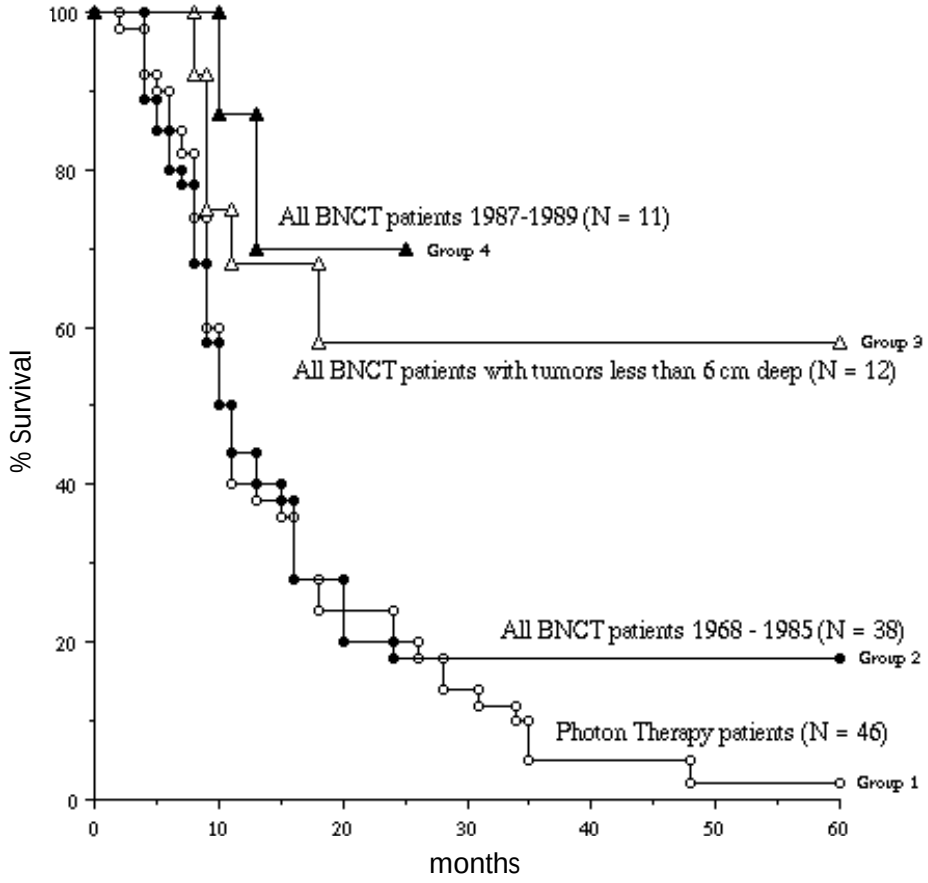

Fig. 5: Postoperative survival time of patients with malignant gliomas treated with BNCT [from: Hatanaka, 1989].

Despite of the long use of BSH in BNCT little is known about its uptake mechanism and distribution within the tumor cell. Furthermore, different studies with various methods have shown different results for the localization of BSH (table 2).

Authors, year	Method	Location of BSH
Amano, 1986	neutron-induced alpha-autoradiography	predominantly near the nuclear membrane
Haselsberger et al., 1994	Laser microprobe mass analysis	In the nuclei
Ceberg et al., 1995	Atomic emission spectroscopy of subcellular fractions	nuclei, mitochondria, other cell organelles, cytosol and extracellular fluids
Otersen et al., 1997	Immunohistochemistry	in the nuclei and cytoplasm with a correlation between the amount of BSH in the nuclei and time between infusion and tumor sampling

Table 2: Earlier investigations of the subcellular localization of BSH in tumor tissue.

Due to the limited range of the fission particles (about 5 and 10 µm), the localization of boron-10 on a subcellular level has a great influence on the biological effectiveness of BNCT (Kobayashi and Kanda, 1982; Gabel et al., 1987). Its outstanding importance makes the nucleus the preferred target of BNCT. Gabel et al. (1987) has calculated the energy deposited by the neutron capture reaction to the nucleus for different boron distribution pattern and compared it to the biological effects resulting by these distributions. The Relative Local Efficiency (RLE) which indicates the effectiveness of a given intracellular boron concentration to produce cell death in relation to a uniform distribution throughout the cell was found to be six times higher for boron localization in the nucleus than for a localization in the cytoplasm and 15 times higher for a localization on the cell surface.

2.3 AIMS OF THE PRESENT STUDY

Although BSH is being used clinically, the chemical basis for its tumor cell selectivity is still unknown. Elucidation of the mechanism by which this compound is taken up and persists in tumor cells is critical for the design of new and possibly more effective boron delivery agents (Barth et al., 1999). It was the goal of this study to find characteristic properties of the BSH-containing cells that could be responsible for the tumor selective uptake of BSH after infusion. Therefore the distribution of BSH should be compared with the incidents of structural modifications of tumor cells. To achieve this, BSH and tumor-selective antigens should be visualized by immunohistochemistry of identical tissue regions and the obtained distribution maps compared to each other. In this way the requirements of BSH uptake and accumulation possibly could be determined which could lead to optimized boron carriers for BNCT.

The effectiveness of the $^{10}B(n,\alpha)^{7}Li$ depends not only on the amount of boron in tumor tissue compared to that in healthy brain, but highly on an intracellular occurrence in tumor. Modeling studies showed that the subcellular distribution of boron has great influence on the radiobiological effect in BNCT (Gabel et al., 1987). Because the biodistribution of boron in tissue is of great importance, it was the aim to investigate the subcellular distribution pattern of boron respectively BSH in glioma tissue from infused patients. Therefore different direct (electron energy loss spectroscopy (EELS) combined with electron spectroscopic imaging (ESI), x-ray photoelectron emission spectromicroscopy (X-PEEM)) and indirect (transmission electron microscopy) methods for visualization of the subcellular localization of BSH were used. With X-PEEM investigations on the chemical state of BSH in vivo have also been made. Finally the suitability of spheroids as a three-dimensional tumor model for BSH-uptake and distribution studies has been investigated.

3 MATERIALS AND METHODS

3.1 X-RAY PHOTOELECTRON EMISSION SPECTROMICROSCOPY

The MEPHISTO (Microscope à Emission de Photoélectrons par Illumination Synchrotronique de Type Onduleur) spectromicroscope performs microchemical analysis by x-ray absorption near edge structure (XANES) spectroscopy and produces magnified images from microscopic areas (De Stasio, et al. 1998).

The MEPHISTO spectromicroscope uses an electron optics system to form a magnified image of the secondary electrons, originating from inelastic collisions of primary and Auger electrons, emitted by a specimen under soft x-ray illumination (Gilbert et al., 2000). The electron image intensity is amplified by a series of two microchannel plates, and converted into a visible image by a phosphor screen. This image is captured by a video camera linked to a computer for display and data acquisition. The image magnification is continuously variable up to 8,000 times, and the maximum lateral resolution has been measured to be 20 nm (De Stasio et al., 1999).

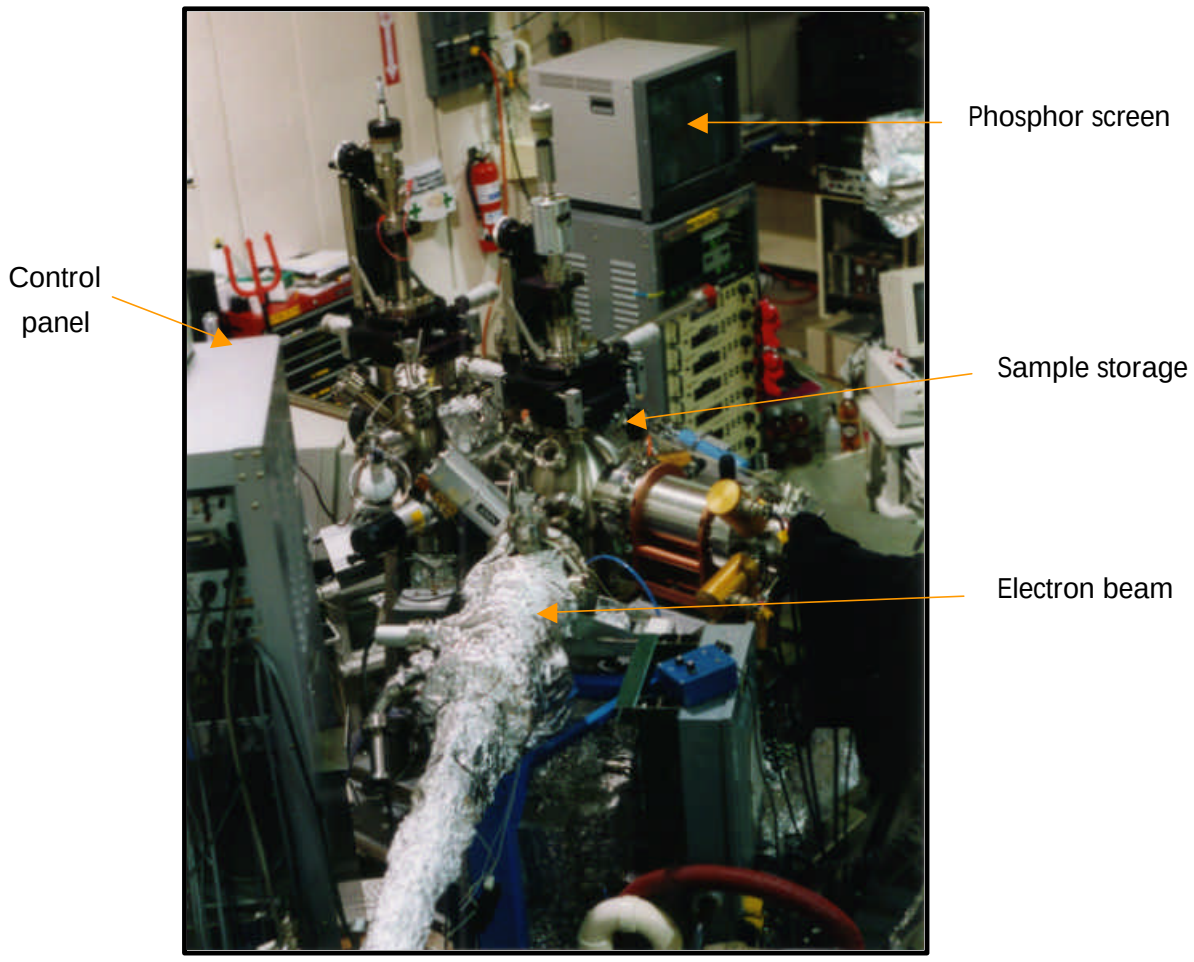

Fig. 6: The MEPHISTO spectromicroscope, developed and built by G. de Stasio, mounted on the 10m TGM beamline at the Wisconsin Synchrotron Radiation Center.

For comparison of the distribution of BSH with cell structures, it is necessary to enrich these with defined elements (preferable heavy metals like nickel or cobalt). To achieve this, immunoenzymic staining methods with substrates that contain these elements were used (see also 3.7.4). As a result of this marking, it is possible to obtain distribution maps of the stained antigen and compare them with the distribution of BSH.

3.2 TRANSMISSION ELECTRON MICROSCOPE (TEM)

Electron microscopy takes advantage of the wave nature of rapidly moving electrons. Where visible light has wavelengths from 400 nm to 700 nm, accelerated electrons have a wavelength of about 10 pm. Optical microscopes have their resolution limited by the diffraction of light to about 1000 times magnification. Electron microscopes are limited to magnifications of around 10^6 times, primarily because of spherical and chromatic aberrations (Amelinckx et al., 1997).

A transmission electron microscope generates a beam of electrons in a vacuum. The beam is collimated by magnetic condensor lenses and focused to a small spot on the surface of the sample by an objective lens. The sample must be very thin because the image is formed by the electrons that pass through the sample. Electrons interacting with elements in the sample (predominantly elements of high atomic number) are deflected by elastic scattering and hit the aperture resulting in a dark spot at the positions of the heavy elements in the sample. Electrons that pass through contain an image of the sample formed by the varying electron absorption of the sample. Those electrons then go through a series of projector lenses that magnify the image. The resulting image is displayed on a phosphor screen - the electrons leaving the sample causing the screen to glow. Photographs are taken by directly exposing a photographic emulsion to the electron beam. Because the predominant elements in organic tissue are of low atomic number the sample must be contrasted with heavy elements (normally uranium or lead) or labeled with antibodies conjugated to heavy atoms (e.g. gold, silver or iron) (see also 3.7.3). In this study the EM 10 (Zeiss, Germany) and an electron acceleration voltage of 60 kV were used.

3.3 EELS/ESI

The EELS technique probes the solid state environment of elements in a sample by analyzing the energy distribution of electrons that have been inelastically scattered during their passage through the material. Using a multi-channel diode array, a spectrum of a range of energy loss electrons can be acquired. The spectra have a characteristic feature of a fall off in intensity. Superimposed on these spectra are elemental characteristic peaks that correspond to the absorption edges for the elements that interact with the electron. These spectra are complementary to energy-dispersive x-ray spectroscopy (EDX) spectra in that they are of higher energy resolution (1 - 2eV) and more sensitive to light elements (≤ Li) (Amelinckx et al., 1997). However, these spectra are difficult to quantify. By combining electron spectroscopy and transmission electron microscopy, the analytical power of EELS is coupled with the ability to select, image and obtain diffraction patterns from small areas. In addition, EELS can provide detailed information about the electronic state and chemical bonding of the sample. Data about the energy loss can also be used to obtain electron spectroscopic images (ESI). In ESI, the distribution of a chosen element can be represented with high spatial resolution (Colliex, 1986), whereas EELS can supply the chemical analysis of the same area. Element analysis of untreated sections were performed with an energy filtering transmission electron microscope CEM 902 operated at 80 kV (Zeiss, Germany). Elemental maps were calculated with an image processing system (Kontron, Germany) based on the Two-Window-Method (Probst and Bauer 1987; Lehmann et al. 1990).

3.4 LIGHT/FLUORESCENCE MICROSCOPY

For picture acquisition in light and conventional fluorescence microscopy the digital camera DMC 1 (Polaroid, USA) mounted on a Axiovert S100 microscope (Zeiss, Germany) with the following objectives were used: Plan-Neofluar 5x (NA 0.15), Plan-Neofluar 20x (NA 0.5) and Plan-Apochromat 63x (NA 1.4 oil) (all from Zeiss, Germany). The resulting picture files were modified in Adobe Photoshop 5.0.

For fluorescence microscopy a mercury lamp HBO 100 (Zeiss, Germany) and the following filter sets were used (see also Fig. 7):

Filter set 02 for UV-excitation,
Filter set 17 for FITC-excitation and
Filter set 14 for Vector Red®-excitation
(all filter sets from Zeiss, Germany).

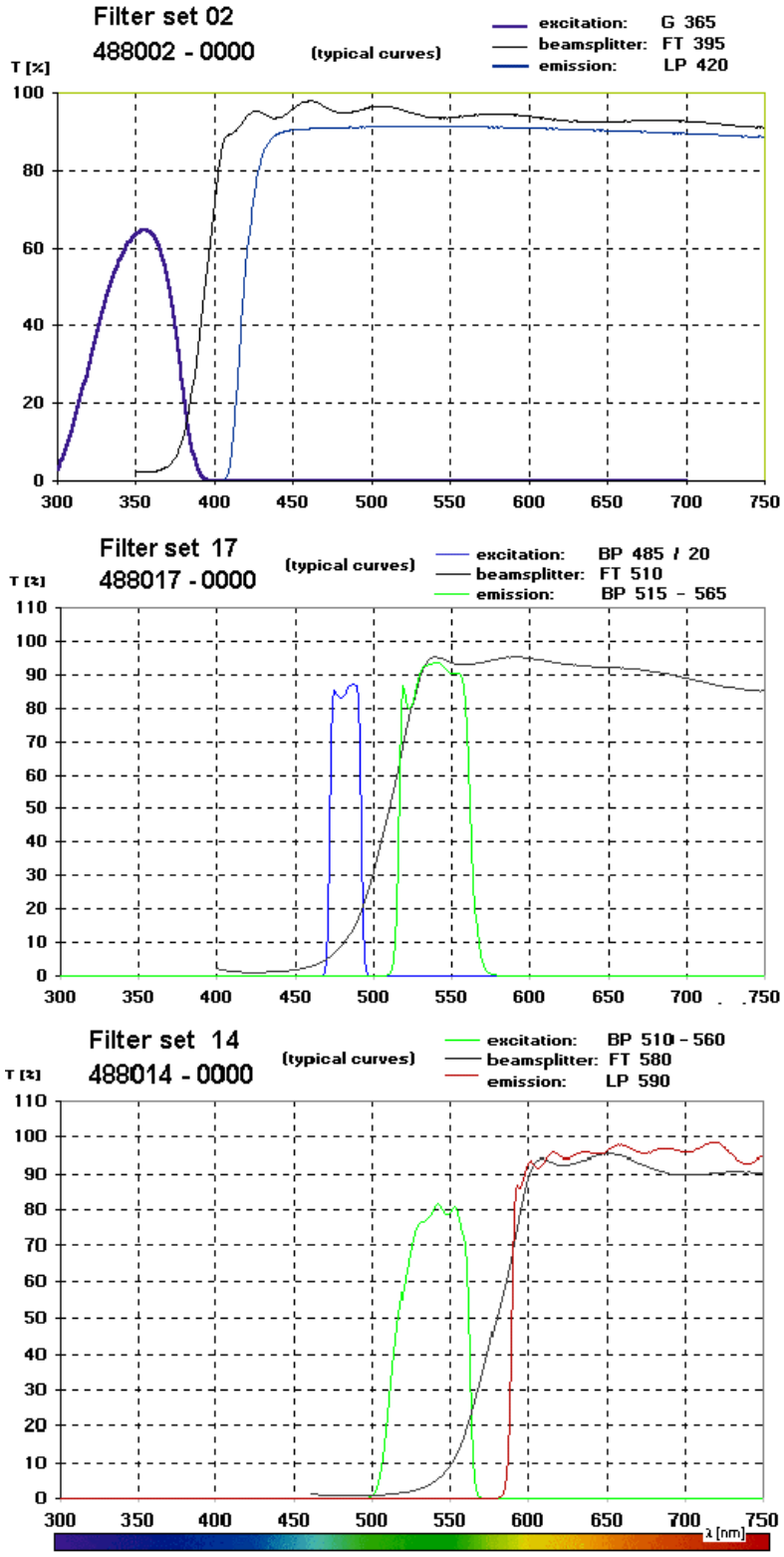

Fig. 7: Filter sets for conventional fluorescence microscopy used in this work. Wavelengths for excitation, beamsplitter and emission are shown beside the set number of each filter [modified from: www.zeiss.com]

3.4.1 CONFOCAL LASER SCANNING MICROSCOPY (CLSM)

Laser Scanning Confocal Microscopy (LSCM or CLSM, Confocal Laser Scanning Microscopy) is established as a valuable tool for obtaining high-resolution images and 3-D reconstructions of a variety of biological specimens (Stevens et al., 1994).

In CSLM, a laser light beam is expanded to make optimal use of the optics in the objective. Through a x-y deflection mechanism this beam is turned into a scanning beam, focused to a small spot by an objective lens onto a fluorescent specimen. The mixture of reflected light and emitted fluorescent light passes through the same objective and is focused onto a photodetector (photomultiplier) via a dichroic mirror (beamsplitter). The reflected light is deflected by the dichroic mirror while the emitted fluorescent light passes through in the direction of the photomultiplier (Fig. 8). The analog light signal, detected by the photomultiplier, is converted into a digital signal, contributing to a pixel-based image displayed on a computer monitor attached to the CLSM. The relative intensity of the fluorescent light, emitted from the laser point, corresponds to the intensity of the resulting pixel in the image (8-bit grayscale). A 3-D reconstruction of a specimen can be generated by stacking 2-D optical sections collected in series.

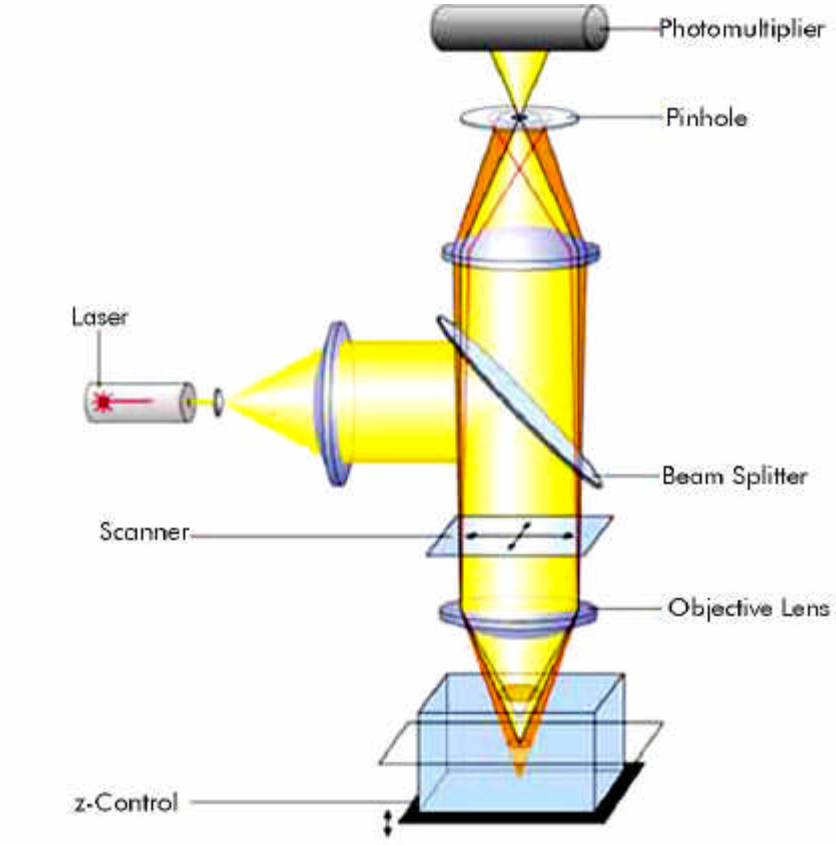

Fig. 8: The general setup of a CLSM [modified from: www.zeiss.com].

A confocal aperture (pinhole) is placed in front of the photodetector, so that the fluorescent light from points on the specimen that are not within the focal plane, where the laser beam was focused will be largely obstructed by the pinhole. In this way, blurred images from out-of-focus planes are greatly reduced. This becomes especially important when dealing with thick specimens (Fig. 9).

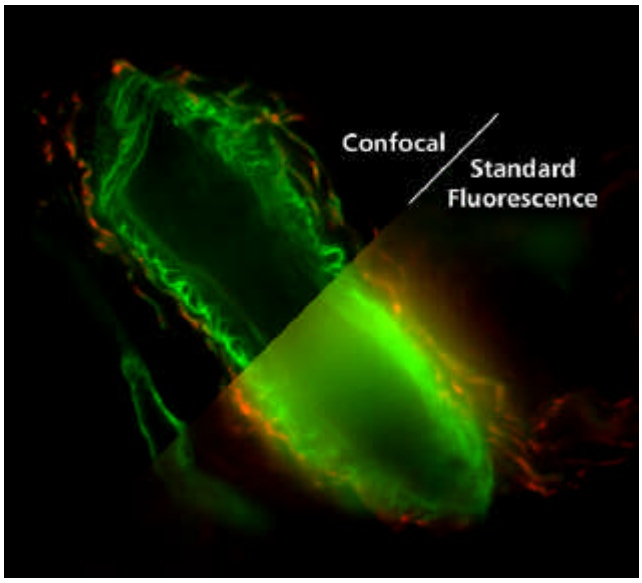

Fig 9: Human skin section (basement membrane - cy2 (green), neurons - cy3 (red)) [from: www.zeiss.com; specimen courtesy of Dr. William R. Kennedy and Gwen Wendelschafer-Crabb, Department of Neurology, University of Minnesota].

In this work the LSM 410 invert (Zeiss, Germany) was used. Fluorescence emission was recorded through a Plan-Neofluar x 40, NA 1,3 oil objective. All measurements were made with the following filter sets: chromatic beamsplitter FT510, bandpassfilter BP 515-565 for argon laser irradiation at 488 nm and FT 560 long pass filter LP 570 for helium neon laser irradiation at 543 nm.

3.5 ORIGIN OF TUMOR MATERIAL

Tumor material was collected in a pharmacokinetic study aimed at identifying optimal time point and dosage of BSH. Tissue samples were taken from glioma patients (grade IV, glioblastoma multiforme) who had received BSH prior to surgery in the Zentralkrankenhaus St. Jürgenstraße (Bremen, Germany). Intravenous infusions (40 - 102 mg BSH/kg body weight) were carried out for one hour, 14 to 22 hours before operation (Haritz et al., 1994). After surgery, the material was frozen rapidly and stored at -18 °C.

Patient code	Age	Administered amount of ^{10}B/ kg body weight	Time between infusion and tumor sampling	Average boron concentration in tumor at surgery
HO	71 years	31.3 mg	14 h	84.2 ppm
WB	66 years	54.0 mg	24 h	16.7 ppm
GO	59 years	21.1 mg	72 h	0.5 ppm
FJ	56 years	55.9 mg	17 h	39.0 ppm
WF	46 years	31.3 mg	24 h	16.4 ppm
BE	38 years	27.9 mg	47 h	8.7 ppm
JU	33 years	28.1 mg	22 h	12.2 ppm

Table 3: Data of the patients from whom the tumor material was taken.

The tumor material available for this study was originally prepared for light microscopy. Due to suboptimal freezing and storage for electron microscopy the tissue material was morphologically in bad condition. Organelles could rarely be found with exception of nuclei. Because of the unique study from which these samples were obtained no other BSH-containing tumor material was available and the investigations were performed on these samples.

3.6 PREPARATION OF THE TUMOR MATERIAL

For light and fluorescence microscopic use the tissue was fixed in 10 % buffered formalin for 20 h at room temperature (rt). Previously it had been shown that this treatment does not remove boron from this tissue (Otersen et al., 1996). The tissue was dehydrated in increasing concentrations of ethanol (70 %, 90 %, 100 %) for 3 times 30 min each concentration. Afterward, the material was incubated in toluene (about 1h) and embedded in paraffin. Thin section (5 µm) were cut and collected onto 3-aminopropyl-triethoxysilan-coated glass slides, dried and stored at room temperature until use.

For subcellular investigations the tissue was either fixed in 2 % glutaraldehyde in cacodylic buffer (0.1 M, pH 7.2) over night at 4 °C or already fixed tissue for light microscopy was used. The tissue was dehydrated in increasing concentrations of ethanol (50 %, 70 %, 90 %, 95 %, 100 %) for 30 min each and afterwards incubated in increasing concentrations of LR White (London Resin Company, England) in ethanol up to 100 %. The tissue material was placed in gelatin capsules filled with LR White and polymerized at 4 °C by addition of small amounts of a catalyst (London Resin Company, England). Ultra-thin sections (50 - 70 nm) were cut and mounted on nickel-grids (300 - 600 mesh) or silicon wafers.

3.7 IMMUNOHISTOCHEMISTRY

3.7.1 ANTIBODIES

3.7.1.1 Anti-BSH

At the Institut für Tierzucht und Tierverhalten (Mariensee, Germany) a goat was immunized with BSH, which was linked through sulfhydryl groups to bovine serum albumin (BSA). The resulting serum was freed from antibodies directed against BSA by affinity chromatography over a column of BSA bound to sepharose followed by a fast protein liquid chromatography (sepharose-12). The resulting fractions were collected separately and evaluated by ELISA (enzyme linked immunosorbant assay).

3.7.1.2 Anti-von Willebrand Factor

Clone: F8/86 (DAKO, Denmark)

Human von Willebrand Factor (vWF or factor VIII-related antigen) is a 270 kD, multimeric, multidomain glycoprotein. von Willebrand factor is synthesized by endothelial cells and is also present in platelets, megakaryocytes and a number of tumors. It mediates platelet adhesion to injured vessel walls and serves as a carrier and stabilizer for coagulation factor VIII. Deficiency of vWF, particularly mutations in the A1 and A2 domains, can cause von Willebrand disease (vWD), a common autosomally inherited bleeding disorder. vWF is synthesized by endothelial cells and is stored in Weibel Palade bodies or granules where it is released either constitutively or by a regulated pathway. It mediates platelet adhesion to injured blood vessel walls in thrombotic events. vWF has traditionally been used as a cell marker for identifying endothelial and megakaryocytes cells as well as a marker of angiogenesis, which reportedly predicts tumor recurrence (Chung-Welch et al., 1997a; Chung-Welch et al., 1997b). However, because not all endothelial cells synthesize or store vWF, about 30 % of the tumors of vascular origin fail to stain for factor VIII related antigen, regardless of whether they are benign or malignant (Perutelli and Mori, 1997).

3.7.1.3 Anti-Laminin

Laminin is a heterotrimeric glycoprotein that is found only in the basement membrane of tissues and carcinoma cells (Nomizu et al., 1994; Wewer et al., 1994). It is composed of α, β, and γ chains held together in an alpha-helical coiled-coil structure (Nomizu et al., 1994). Normal and neoplastic cells interact with laminin via a variety of different cell surface proteins including the intergrins (Cioce et al., 1993). The primary laminin receptor has a molecular weight of 68 - 72 kDa and is found in both normal tissues and carcinomas (Wewer et al., 1986). Expression of both laminin and its receptor has been shown to be regulated by fibronectin and its receptor (Huang et al., 1994).

3.7.1.4 Anti-EGFR

Clone: F4 (Sigma, USA)

Epidermal growth factor (EGF) initiates its effects on cell growth through interaction with a cell surface glycoprotein receptor (Hunter, 1984). Binding of EGF or transforming growth factor α to the receptor activates a tyrosine-specific protein kinase intrinsic to the EGF-receptor protein. The phosphotyrosine content of target cells increases rapidly and the EGF-receptor is phosphorylated on tyrosine residues (Ushiro and Cohen, 1980; Reynolds et al., 1981). As a result of EGF binding to its specific receptor, there is increased DNA synthesis as well as other events including cell proliferation, differentiation and repair of damaged epithelial tissue (Sigma product information). Among astrocytic tumors, amplification of the EGFR gene is most frequently observed in glioblastomas (Bigner et al., 1988; Ekstrand et al., 1992; Hurtt et al., 1992; Collins, 1993; von Deimling et al., 1993). The frequency of EGFR amplification is increasing with the tumor grade (Lang et al., 1994). Tumors demonstrating gene amplification have increased amounts of ribonucleic acid transcripts from the gene and immunohistochemically identifiable overexpression of the cell surface protein (Ekstrand et al., 1992; Collins, 1993).

3.7.1.5 Anti-p53

Clone: BP53-12-1 (BioGenex, USA)

The human p53 tumor suppressor gene encodes a 393 amino acid phosphoprotein that binds to specific DNA sequences and directly interacts with various cellular and viral proteins (Lane, 1992). p53 is the most commonly mutated gene in human cancer, with the majority of the mutations being amino acid substitutions (Greenblatt et al., 1994). The p53 gene resides on the p arm of chromosome 17 (Lang et al., 1994). Inactivation of the p53 gene occurs most commonly through the loss of one 17p allele with mutation in the remaining p53 allele (Saxena et al., 1992; von Deimling et al., 1992a). The normal function of p53 is to effect cell cycle arrest at the G1 and G2 checkpoints in response to DNA damage (Kastan et al., 1991; Kastan et al., 1992; Kuerbitz et al., 1992) thus allowing DNA repair to take place. This function is executed by accumulation of p53 followed by induction of various genes such as WAF1 and MDM2 (Kastan et al., 1992; Barak et al., 1993; El-Deiry et al., 1994). The WAF1 protein complex is a potent and reversible inhibitor of cell cycle progression at both the G1 and G2 checkpoints (El-Deiry et al., 1994; El-Deiry et al., 1995; Agarwal et al., 1995). Over-production of MDM2 results in inhibition of the ability of wild type p53 to stimulate expression of target genes (Oliner et al., 1992; Leach et al., 1993), including expression of MDM2 itself (Barak et al., 1993). If repair is not successful, p53 initiates programmed cell death, thus preventing the propagation of genetic defects to successive generations of cells.

Alteration of the p53 gene is an early event in astrocytic tumor progression (Lang et al., 1994). Altered p53 function results in deregulated cell growth and increased “genetic instability” (Lane, 1992). Therefore, low-grade astrocytomas with p53 alterations have a greater probability for further genetic aberrations, which could lead to progression of higher grades of malignancy (Lane, 1992).

3.7.1.6 Anti-GFAP

Clone: DP 46.10 (Immunotech, France)

Glial fibrillary acidic protein (GFAP) is an intermediate filament protein of 52 kD (Liem et al., 1978) found in glial cells e.g. astrocytes and ependymal cells. In the peripheral nervous system, GFAP has been demonstrated in Schwann cells, enteric glial cells and satellite cells of human sensory ganglia. GFAP can be found in great amounts in the cytoplasm of astrocytes, but not in the nucleus (Bignami and Dahl, 1977). While the incidence of GFAP in tumors of glial origin (e.g. astrocytomas, glioblastomas and oligodendrogliomas) is up to 85 times higher than in the gray matter of normal human brain, it is rarely found in tumor of other origin (Rasmussen et al., 1980) The amount of GFAP is directly proportional to the number of malignant astrocytes and indirectly proportional to the necrotic portion of the tissue (Delpech et al., 1978).

3.7.1.7 Anti-CD44

Clone: DF1485 (DAKO, Denmark)

The CD44 molecule belongs to a family of cellular adhesion molecules found on a wide range of normal and malignant cells in epithelial, mesothelial and haematopoietic tissues. CD44 has been shown to mediate cell–cell and cell–ECM (extra cellular matrix) interactions (Aruffo et al., 1990; Miyake et al., 1990), costimulate lymphocyte activation and tissue infiltration (Shimizu et al., 1989; Lesley et al., 1994), and promote growth and metastasis of some tumor types (Gunthert et al., 1991; Sy et al., 1991). CD44 is a single gene with 20 exons, of which 10 are normally expressed to encode the basic CD44 (H-CAM) molecule (Yu et al., 1993; Mackay et al., 1994). The additional 10 exons are only expressed by alternative splicing of the nuclear RNA. The expression of specific cell adhesion molecule CD44 splice variants has been shown to be associated with metastasis and poor prognosis in certain human malignancies, such as breast cancer (Yu et al., 1993). A complex pattern of CD44 variant expression in different tumors compared to the CD44 expression of the normal cell of origin has been reported (Fox et al., 1994).

3.7.1.8 Anti-Ki-67

Clone: MIB 1 (Dianova, Germany)

Ki-67 is a widely distributed protein whose expression is restricted to proliferating cells and which is widely used in routine pathology as a "proliferation marker" to measure the growth fraction of cells in human tumors (Schluter et al., 1993). Two isoforms exist for the protein, which differ by an alternative splicing event (Duchrow et al., 1995). The function of this DNA-binding protein, which is predominantly (90 - 95 %) located in the nucleus (Lopez et al., 1994), is still unknown. Ki-67 has a half-life of about 90 minutes and begins to accumulate in late G1 in a nuclear foci pattern and progresses in expression through S and is maximal in G2/M (Heidebrecht et al., 1996; Starborg et al., 1996) (Fig. 10). At the S/G2 border the Ki-67 protein is redistributed to become associated with the surface of condensed chromatin where its conformation is modulated by dsDNA thereby allowing the binding of the Ki-67 antibody (Lopez et al., 1994).

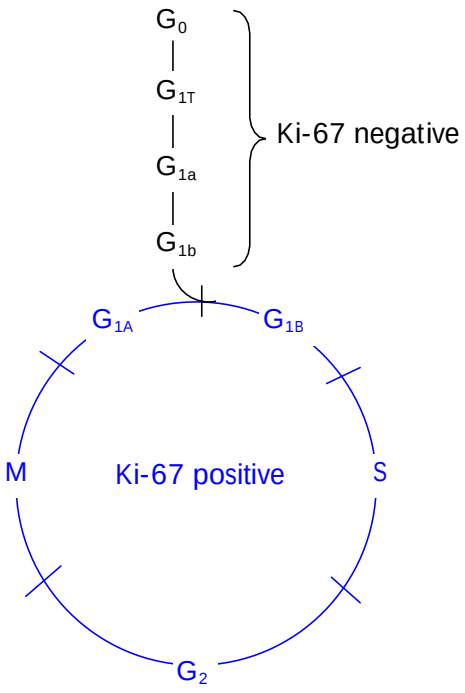

Fig. 10: Expression of the Ki-67 protein during cell cycle.

3.7.2 ANTIGEN RETRIEVAL

Formaldehyde has been used widely to the present day (Fox et al., 1985; Puchtler and Meloan, 1985). As a fixative, formalin is made up of concentrated formalin (37 - 40 % solution of formaldehyde) diluted to a 10 % solution (3.7 - 4 % formaldehyde). Although formaldehyde fixed tissue samples show good preservation of morphological detail, most antigens under investigation are influenced significantly and adversely by formalin fixation (Taylor, 1979, 1980, 1994; Leong and Gilham, 1989; Battifora and Kopinski, 1986). The critical importance of rendering the immunohistochemistry technique suitable for routine paraffin sections was pointed out by Taylor and Burns (1974). The utility of immunohistochemistry in surgical pathology increased with the use of enzyme digestion (Huang, 1975; Curran and Gregory, 1977) and the development of antibodies against formalin-modified antigens (Harrach and Robenek, 1990). Unfortunately the use of many antibodies for routinely processed paraffin sections continued to be limited in spite of these enhancement techniques and improvements in the detection system (Leong et al., 1988). Biochemical studies of the chemical reaction between protein and formalin by Fraenkel-Conrat and co-workers (1947, 1948a, b) indicated that hydrolysis of cross linkages between formalin and protein is limited by certain amino acid side chains, such as imidazol and indol, but that these cross linkages can be reversed by high-temperature heating (120 °C) or strong alkaline treatment. This observation formed the basis for the development of antigen retrieval techniques in 1991 (Shi et al., 1991). Another important factor, besides heat, is the pH of the solution (Shi et al. 1995; Evers and Uylings 1994). Although some antigens yield satisfactory results by antigen retrieval treatment with the use of distilled water, other antigens require heating in buffers of specific pH to obtain the strongest intensity of staining. A few antigens yield satisfactory results only when buffers in a limited pH range were used (Grossfeld et al., 1996).

For all antibodies used in this study the influence of trypsin digestion and microwave treatment at different pHs were tested (Table 4).

To achieve this, several tissue sections from different patients were stained with all antibodies used in this work after protein digestion with trypsin, after microwave heating in citrate buffer of pH 2 or 6[1] and without antigen retrieval methods. The influence of the power output of the microwave (400 W, 600 W, 750 W), number of heating intervals (all steps from 1 to 4) and their duration (2 min, 4 min, 6 min) were also studied.

[1] At pH 8 and higher the tissue came off from the glass slides during microwave heating. Therefore the influence of higher pH on antigen retrieval could not be tested.

Antigen	Optimal concentration of the used antibody without microwave treatment	Optimal concentration of the used antibody with microwave treatment in citrate buffer of pH 2 and 6		Protein digestion (Trypsin)
		pH 2	*pH 6*	
p53	1:100 (+ + +)	1:200 (+ + +)	1:200 (+ + +)	not tested
GFAP	1:10 (+)	1:150 (+)	1:150 (+ + +)	1:10 (+)
Ki-67	--	30 % (+ + +)	40 % (+ +)	--
BSH	1:100 or 1:120 (+ +)	--	--	1:100 or 1:120 (+ +)
EGFR	1:100 (+ +)	1:100 (+)	1:100 (+)	1:100 (+ +)
vWF	1:250 (+ + +)	1:350 (+ + +)	--	1:300 (+ +)
Laminin	1:1000 (+ + +)	1:2500 (+ + +)	--	1:1600 (+ +)
CD44	1:50 (+ +)	1:200 (+ + +)	1:200 (+ + +)	1:50 (+ +)

Table 4: Microwave treatment can enhance the sensitivity of certain antibodies dramatically, whereas for others it decreases or eliminates the staining. Furthermore the grade of antigen retrieval or masking depends on the pH of the buffer used during the treatment. In brackets behind the concentrations are the ratings of the staining quality in regard of amount of positive stained structures and contrast (intensity of positive staining vs. unspecific staining): -- no positive staining, + weak/intermediate staining and strong/intermediate background, + + good staining and strong/intermediate background, + + + good staining and weak or no background.

Microwave treatment enhanced dramatically the staining results for the antibodies against p53, CD44, Ki-67, laminin and GFAP (Fig. 10). For vWF, the gain in sensitivity was only intermediate. In the case of Ki-67 staining without microwave treatment gave no result. For vWF and laminin the staining was dependant on the pH used during heating: While microwave treatment in citrate buffer of pH 2 gave good staining results, no staining could be observed when heated in citrate buffer of pH 6 (Fig. 11). For BSH, the detection by the antibody after heating was weak or negative (depending on number of heating cycles). This was also observed by Otersen et al. (1997). Counterstains of the nuclei (DNA) with Mayer's Hematoxylin, Hoechst 33342 and acridine orange were negative after microwave heating in pH 2 but not in pH 6 (Fig. 11 and 12).

Power output of the microwave, duration and number of the heating intervals had no or only marginal effects when the slides were heated at least 10 min (all intervals added up) in boiling citrate buffer.

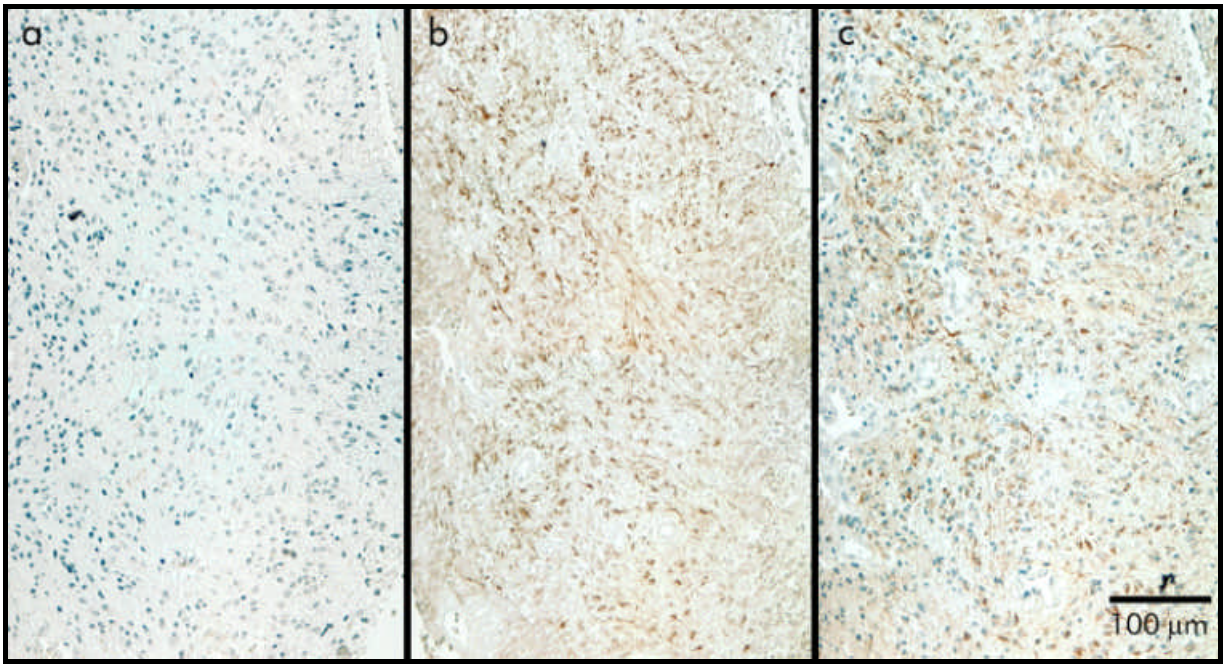

Fig. 11: Staining for GFAP with the same antibody concentration (1:150): a) without microwave heating, b) microwave heating in citrate buffer (pH 2), c) microwave heating in citrate buffer (pH 6). Hematoxylin counterstain (patient WF).

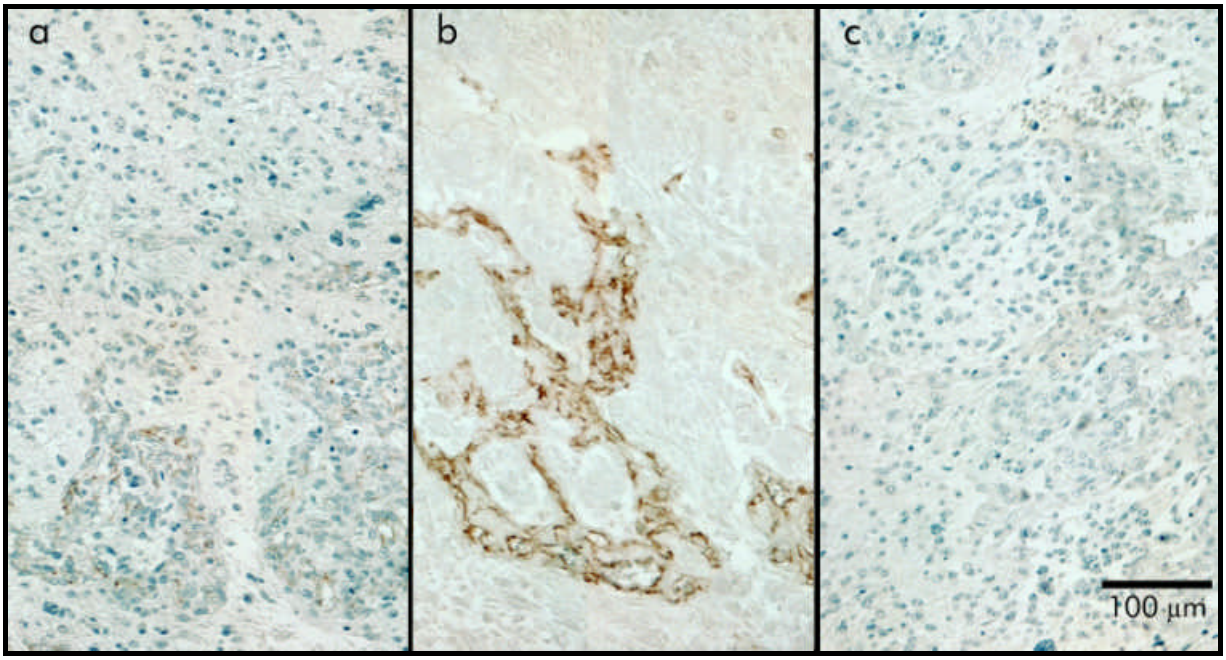

Fig. 12: Staining for vWF with the same antibody concentration (1:150): a) without microwave heating, b) microwave heating in citrate buffer (pH 2), c) microwave heating in citrate buffer (pH 6). Hematoxylin counterstain (patient JU).

3.7.3 STAINING PROCEDURE FOR LIGHT AND FLUORESCENCE MICROSCOPY

For fluorescence microscopic investigations autofluorescence was reduced by irradiating the glass slides with light (see also APPENDIX A) for 48 - 72 h.
All steps were performed at room temperature.

3.7.3.1 Immunohistochemical analysis of one antigen

Antibody	Optimal dilution	Microwave treatment
BSH	1:100	no
CD44	1:200	1 x 5 min at 600 W and 3 x 4 min at 400 W in pH 6
EGFR	1:100	no
GFAP	1:150	1 x 5 min at 600 W and 3 x 4 min at 400 W in pH 6
Ki-67	1:2.5	1 x 5 min at 600 W and 3 x 4 min at 400 W in pH 6
Laminin	1:2500	1 x 5 min at 600 W and 3 x 4 min at 400 W in pH 2
p53	1:200	1 x 5 min at 600 W and 3 x 4 min at 400 W in pH 6
vWF	1:250	no

Table 5: Antigen retrieval conditions and antibody dilutions for the detected antigens in this method.

Sections were deparaffinized with xylene (2 times 10 min) and rehydrated in sequential baths of decreasing concentration of ethanol (100 %, 96 %, 90 %, 70 %; 5 - 10 min each) and double distilled water (ddH_2O) (10 min). If laminin, vWF, CD44 or GFAP were the antigens of interest, microwave treatment (see also 3.7.2) was performed. If 3,3'-diaminobenzidine was used as substrate, endogenous peroxidase activity was eliminated by incubation with 2.5 % hydrogen peroxide in ddH_2O for 15 min, followed by two washes in ddH_2O (10 min each). To reduce nonspecific binding, the sections were incubated with 8 % normal rabbit serum (DAKO, Denmark) in incubation-buffer (for ingredients see APPENDIX E) for 1 h. After the serum was blotted off, the sections were covered with primary antibody at a predetermined optimum dilution in incubation-buffer (Table 5) and incubated in a humidified chamber for 20 h (all antigens with exception of BSH) or 40 h (BSH). Negative controls consisted of sections incubated with normal rabbit serum instead of primary antibody. Section were washed three times 10 min in TRIS-PBS (for ingredients see APPENDIX E) and incubated with biotinylated rabbit anti-mouse (DAKO, Denmark, dilution 1:200; for all antigens with exception of BSH) or anti-goat (DAKO, Denmark, dilution 1:200; for BSH) immunoglobulins for 30 min, followed by three washing steps in TRIS-PBS (10 min each). Then the slides were incubated for 40 min with avidin-biotin-complex-solution (Vectastain® Elite ABC for 3,3'-diaminobenzidine or Vectastain® ABC-AP for Vector Red® as substrate; both Kits were from Vector Laboratories, USA; preparation of the solutions were performed as recommended on the data sheet). After three additional washes in TRIS-PBS the staining was developed with 3,3'-diaminobenzidine tetra hydrochloride for 9 min (all antigens with exception of BSH) or with Vector Red® for 25 - 35 min (BSH; lower time limit for fluorescence microscopy, higher time limit for light microscopy) (both substrate kits were from Vector laboratories, USA; preparation of the solutions were performed as recommended on the data sheet). After washing in ddH_2O (3,3'-diaminobenzidine) or 0,1 M Tris-buffer pH 8.3 (Vector Red®) the slides were counterstained with Mayer's Hematoxylin, dehydrated in a series of increasing ethanol concentrations (70 %, 90 %, 96 %, 100 %; 5 - 10 min each) followed by a xylene bath for 5 min and mounted with Entellan® (Merck, Germany).

3.7.3.2 *Immunohistochemical analysis of two antigens*

When two antigens were detected simultaneously the first staining was always BSH with Vector Red®. Second staining consisted of the desired antigen and DAB or FITC.

3.7.3.2.1 Staining of the second antigen with DAB

Antibody	Optimal dilution	Microwave treatment
BSH	1:120	no
CD44	1:200	1 x 5 min at 600 W and 2 x 4 min at 400 W in pH 6
EGFR	1:100	no
GFAP	1:150	1 x 5 min at 600 W and 2 x 4 min at 400 W in pH 6
Ki-67	40 %	1 x 5 min at 600 W and 2 x 4 min at 400 W in pH 6
Laminin	1:1000	no
p53	1:200	1 x 5 min at 600 W and 2 x 4 min at 400 W in pH 6
vWF	1:250	no

Table 6: Antigen retrieval conditions and antibody dilutions for the detected antigens in this method.

Up to the development of Vector Red® all steps were in accordance with the single staining procedure for BSH/Vector Red®. After substrate development the sections were washed in Tris-buffer pH 8.3 and ddH_2O (5 min each). If GFAP was the second antigen to be detected, microwave treatment (see also 3.7.2) was performed. Endogenous peroxidase activity was eliminated by incubation with 2.5 % hydrogen peroxide in ddH_2O for 15 min, followed by two washes in ddH_2O (10 min each). Then the sections were incubated with 8 % normal rabbit serum (DAKO, Denmark) in incubation-buffer for 1 h. After the serum was blotted off, the sections were covered with primary antibody at a predetermined optimum dilution in incubation-buffer (Table 6) and incubated in a humidified chamber for 20 h. Section were washed three times 10 min in TRIS-PBS and incubated with biotinylated rabbit anti-mouse (DAKO, Denmark, dilution 1:200) immunoglobulins for 30 min, followed by three washing steps in TRIS-PBS (10 min each). Then the slides were incubated for 40 min with avidin-biotin-complex-solution (Vectastain® Elite ABC, Vector Laboratories, USA; preparation of the solution was performed as recommended on the data sheet). After three additional washes in TRIS-PBS the staining was developed with 3,3'-diaminobenzidine tetrahydrochloride for 9 min. Counterstaining, dehydration and mounting were identical with the single staining procedure.

3.7.3.2.2 Visualization of the second antigen with FITC

Antibody	Optimal dilution	Microwave treatment
BSH	1:120	no
GFAP	1:30	1 x 5 min at 600 W and 2 x 4 min at 400 W in pH 6
Laminin	1:800	1 x 5 min at 600 W and 2 x 4 min at 400 W in pH 2
vWF	1:50	no

Table 7: Antigen retrieval conditions and antibody dilutions for the detected antigens in this method.

Up to the development of Vector Red® all steps were in accordance with the single staining procedure for BSH/Vector Red®. After substrate development the sections were washed in Tris pH 8.3 and ddH_2O (5 min each). If GFAP was the second antigen to be detected, microwave treatment (see also 3.7.2) was performed. Then the sections were incubated with 8 % normal rabbit serum (DAKO, Denmark) in incubation-buffer for 1 h. After the serum was blotted off, the sections were covered with primary antibody at a predetermined optimum dilution in incubation-buffer (Table 7) and incubated in a humidified chamber for 20 h. Section were washed three times 10 min in TRIS-PBS and incubated with FITC-conjugated rabbit anti-mouse immunoglobulins (Jackson Immunoresearch, USA; 1:150 diluted with incubation-buffer) for 20 h, followed by three washing steps in TRIS-PBS (10 min each). For counterstaining the slides were incubated for 15 min with a solution of Hoechst 33342 (1µg/ml in PBS-buffer pH 7.4). After washing two times in PBS-buffer pH 7.4 and one time in pH 8.1 (5 min each) the slides were mounted with Molwiol (for preparation see APPENDIX E).

3.7.4 STAINING PROCEDURE FOR TRANSMISSION ELECTRON MICROSCOPY

Nickel grids with ultra-thin tissue sections (< 70 nm) were rehydrated in ethanol (90 % and 70 %) and double distilled water for 10 min each. To reduce nonspecific binding, the sections were incubated with 8 % normal rabbit serum (DAKO, Denmark) in incubation-buffer for 1h. After the serum was blotted off, the sections were covered with antibody solution against BSH (dilution 1:100 in incubation-buffer) and incubated in a humidified chamber for 20 h. Section were washed three times 10 min in TRIS-PBS and incubated with gold-labeled anti-goat secondary antibody (Nanoprobes Inc., USA, dilution 1:200 in incubation-buffer) for 20 h possibly followed by silver enhancement (HQ silver, Nanoprobes Inc., USA) for 15 min. Silver enhancement magnifies through gold-catalyzed precipitation the original 1.4 nm sized gold particle conjugated with the secondary antibody for detection at lower magnifications (< 40000x) (Fig. 13).

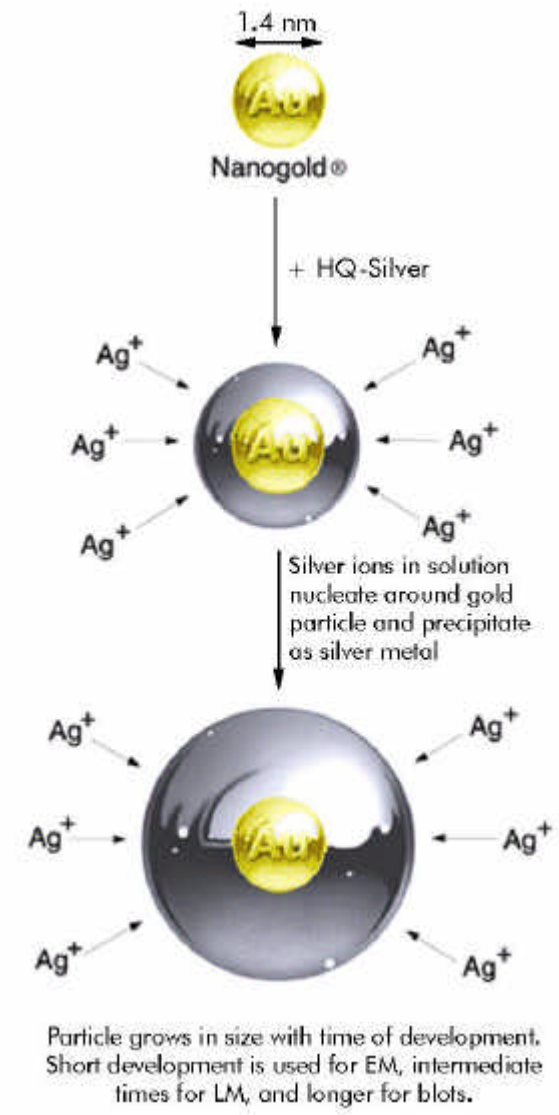

Fig. 13: Scheme for silver enhancement of gold particles [modified from: www.nanoprobes.com]

3.7.5 STAINING PROCEDURE FOR X-PEEM

Desired antigens were stained according to the staining procedure for one antigen with 3,3'-diaminobenzidine (2.7.2) with addition of nickel or cobalt chloride solution (Vector Laboratories, USA; dilution 1:90).

3.7.6 QUANTITATIVE DETECTION OF BORON WITH INDUCTIVELY COUPLED PLASMA MASS SPECTROMETRY (ICP-MS)

About 200 GAMG-spheroids were incubated for different time periods (1 h, 2 h, 4 h, 8 h, 24 h) in Eagle's minimum essential medium (MEM) containing 1 mM Na_2BSH. Negative controls consisted of spheroids incubated in BSH-free MEM. Further two experiments consisted of spheroids that were incubated for 24 h in BSH-containing medium followed by incubation in BSH-free medium for 8 h and 24 h. After incubation the spheroids were washed carefully in PBS (pH 7.4) and in 70 % ethanol for 30 sec then transferred in 2 ml-plastic container (Eppendorf, Germany). The spheroids were dried in an exsiccator under reduced pressure for 48 h and weighed. Then organic carbon were eliminated by heating the spheroids in concentrated nitric acid-hydrogen peroxide solution (1:2) for 72 h at temperatures between 60 and 90 °C. Evaporating liquid were replaced several times. Finally the remaining solution were diluted in 5 % nitric acid and measured with ICP-MS.

4 RESULTS

4.1 LIGHT/FLUORESCENCE MICROSCOPY

4.1.1 BSH

Patient						
FJ	WB	HO	BE	JU	GO	WF
+	+ + +	+ + +	+ +	+ +	+ + +	+ +

Table 8: Number of BSH-positive cells in comparison to tissue size: - no positive cells, + to + + + increasing number of positive cells/tissue area.

Tissue samples from patients with high boron concentrations at surgery (Table 3) do not always have high numbers of BSH-containing cells and vice versa (Table 8). This could possibly be explained by the heterogeneous distribution of BSH in tumor tissue, already shown by different authors (Finkel et al., 1989; Haritz et al., 1992; Otersen et al., 1997). In this work BSH could never be found in regions of necrotic tissue (Fig. 14).

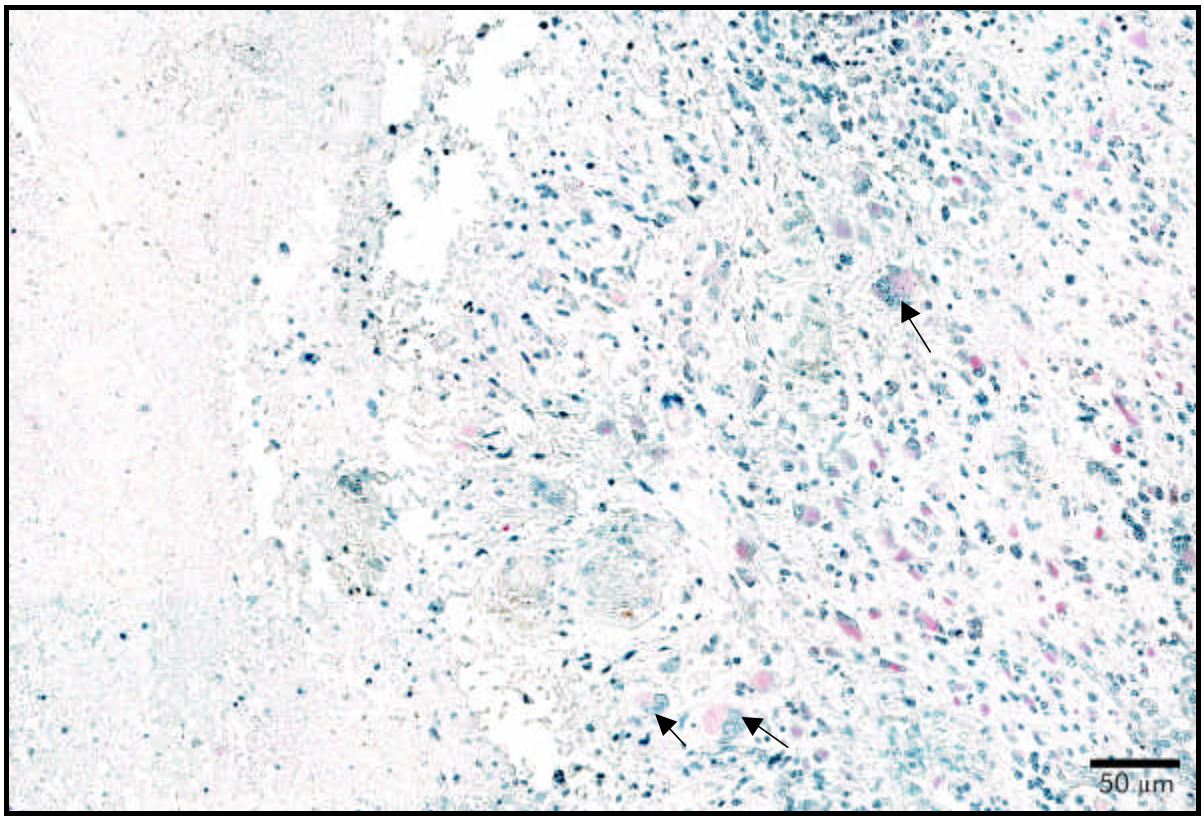

Fig. 14: BSH, stained in magenta, cannot be detected in areas of necrosis (left side). Several cells with multiple nuclei (arrows) (hematoxylin counterstain, patient JU).

Due to the inability of necrotic tissue to accumulate BSH, its distribution in tumor tissue with many areas of necrosis seems less homogenous. Tissue samples from patients GO and HO show no necrosis and a more uniform distribution of BSH than tissue from the remaining patients. BSH can be found in the basement membrane of blood vessels (Fig. 15), in BSH-containing blood (Fig. 34), in the cytoplasm of cells (Fig. 16) and in intercellular space (not shown). No dependence between BSH uptake and morphological characteristics, such as multiple or giant nuclei or cell size could be observed. BSH containing cells show no uniform appearance neither in size nor form (Fig 17).

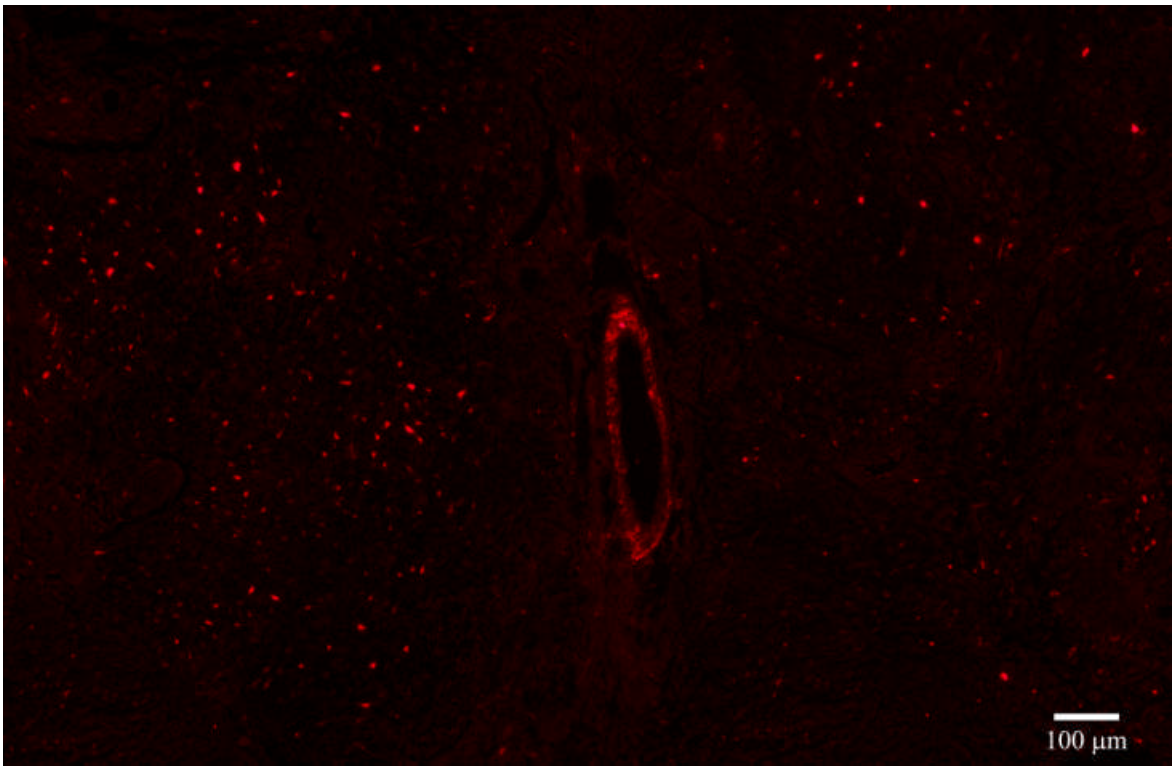

Fig. 15: BSH-containing basement membrane of a blood vessel (middle). On either side of the blood vessel cluster of BSH containing cells are visible (patient HO).

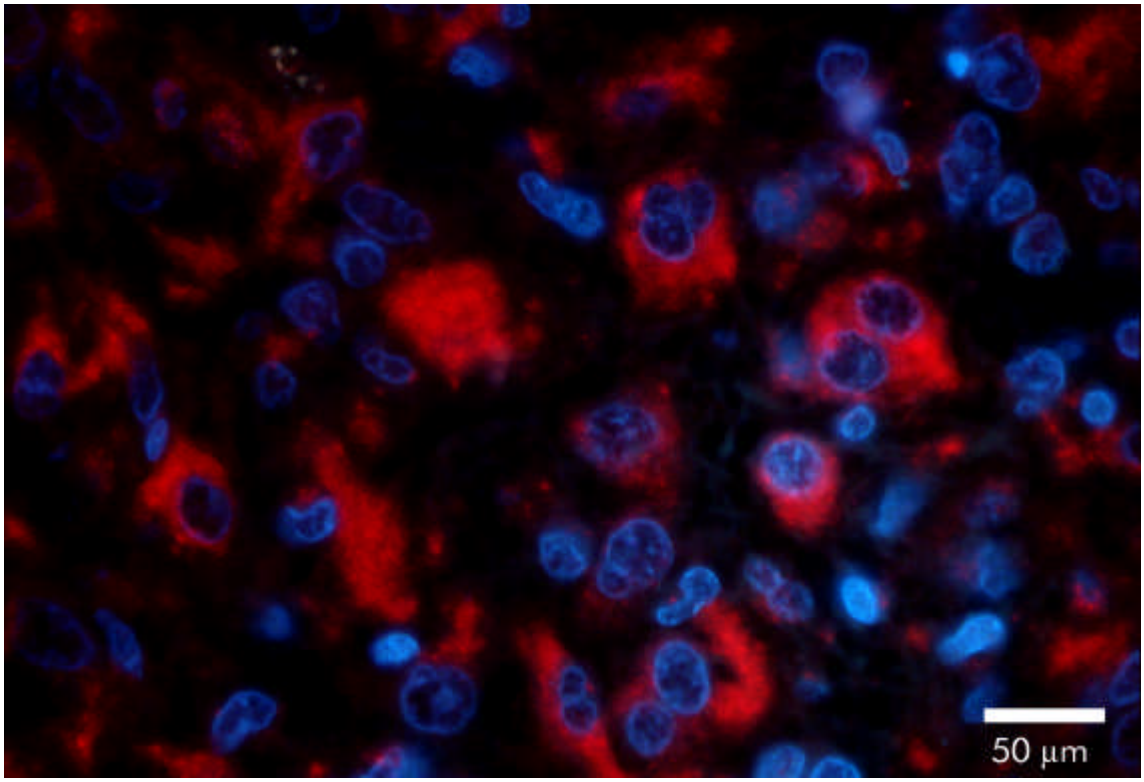

Fig. 16: BSH (red) is located predominantly in the cytoplasm of cells (Hoechst counterstain, patient WB).

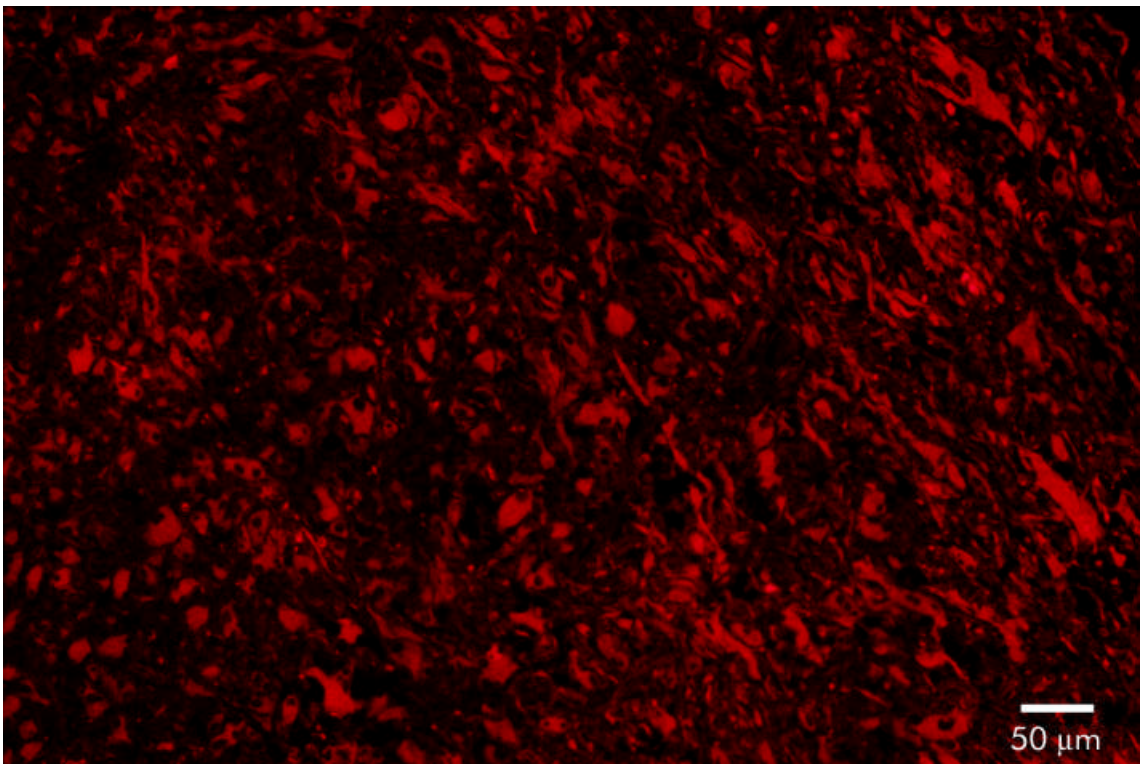

Fig. 17: BSH containing cells have no uniform appearance neither in size nor form (patient HO).

4.1.2 VON WILLEBRAND FACTOR

Patient						
FJ	WB	HO	BE	JU	GO	WF
+	+ + +	+ +	+ +	+ + +	+	+

Table 9: Number of vWF-positive structures in comparison to tissue size: - no positive cells, + to + + + increasing number of positive cells/tissue area.

Intensive neovascularity in tissue from patients HO, JU and BE was observed. Tissue from patients JU and BE show vessels lined up in chains (Fig. 18) whereas in tissue sections from patient HO new blood vessels were distributed homogenously over great parts of the tissue (Fig. 19). Only seldom BSH could be detected in vWF-positive structures (Fig. 20).

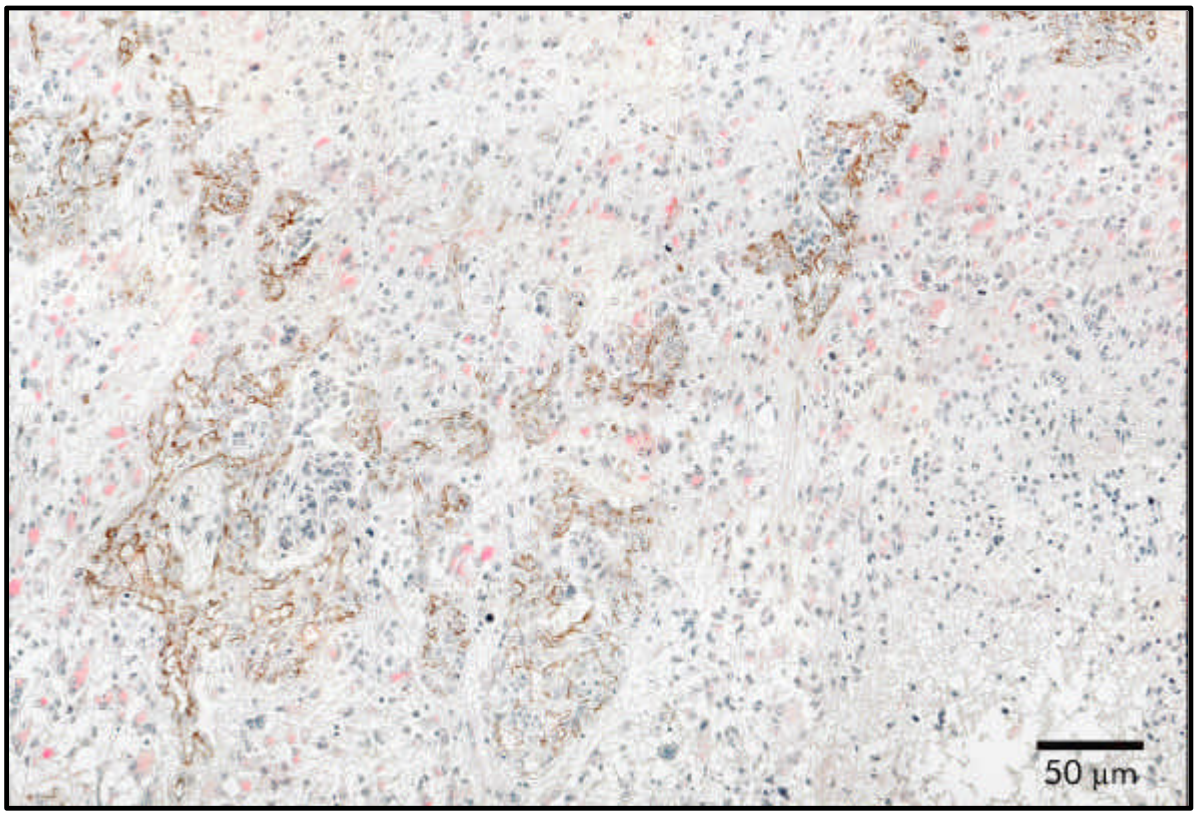

Fig. 18: Long chains of lined up blood vessels (brown) are spread throughout the tissue. BSH (red) is located in the intermediate surrounding (hematoxylin counterstain, patient JU).

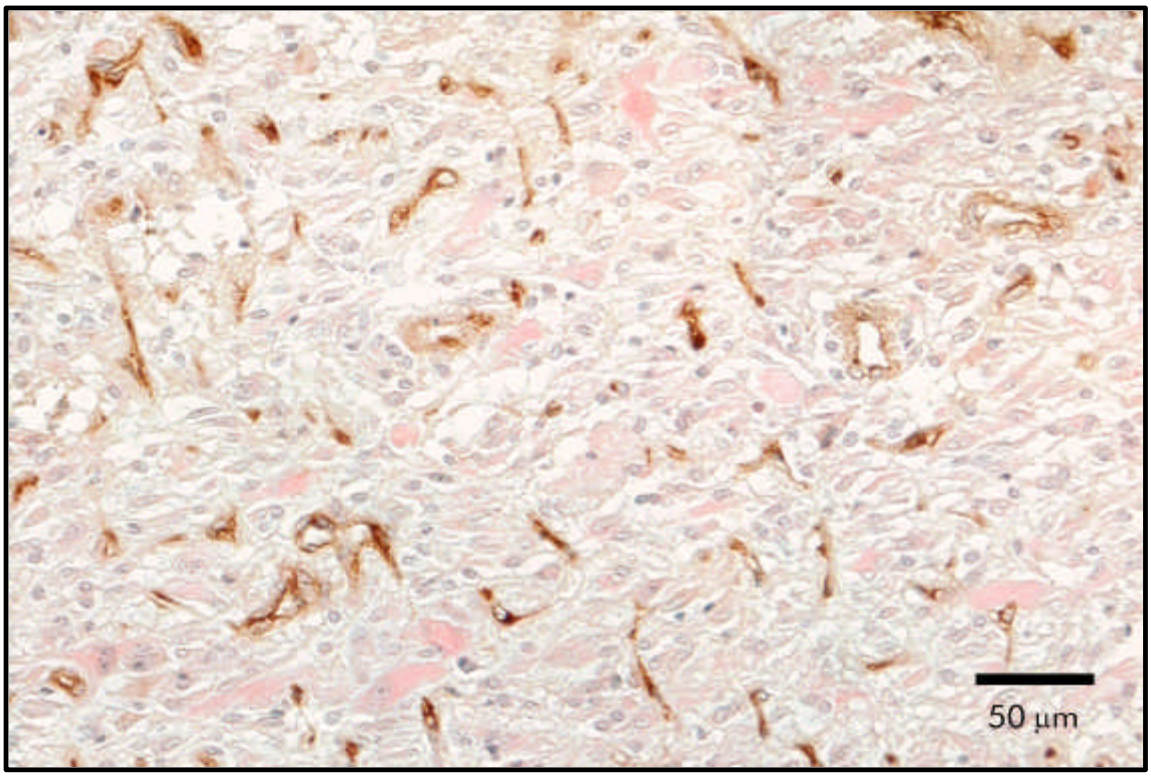

Fig. 19: Small, newly formed blood vessels (brown) are homogenously distributed in the tissue. BSH (red) could be found in the space between the vessels (hematoxylin counterstain, patient HO).

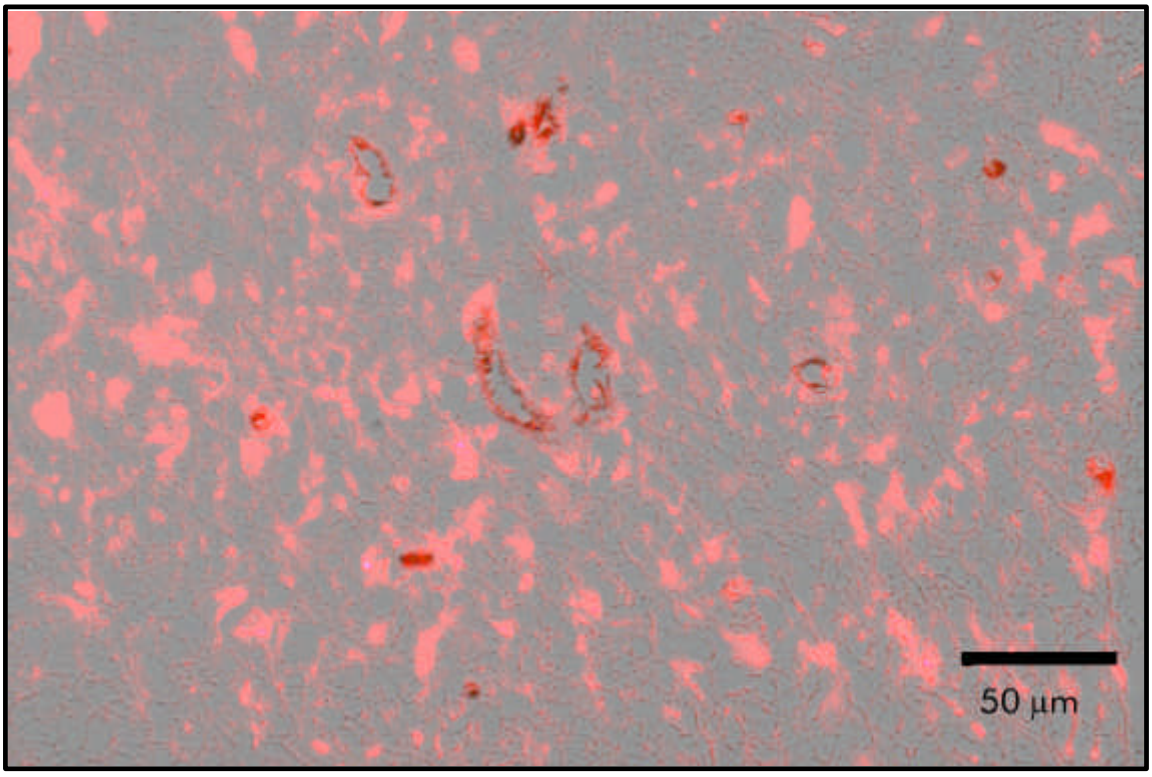

Fig. 20: BSH (red) rarely could be detected in vWF-positive structures (dark). Overlay, obtained by negative multiplication of fluorescence and light microscopic images, patient HO).

4.1.3 CD44

No structures stained positively for CD44 by immunohistochemistry could be found in the tumor samples studied. Positive controls consisting of tissue from patients with glioblastoma multiforme showed strong staining for CD44 (not shown).

4.1.4 LAMININ

Patient						
FJ	WB	HO	BE	JU	GO	WF
+	+	+ + +	+ + +	+	-	+

Table 10: Number of laminin-positive structures in comparison to tissue size: - no positive cells, + to + + + increasing number of positive cells/tissue area.

Laminin, in contrast to all other antigens used in this study, could be found in areas of necrosis (Fig. 21). Furthermore two different types of laminin-staining could be observed: A loose, almost fibrillary type (Fig. 21) (patients HO, JU, BE and FJ) and a dense staining limited to single cells (Fig. 22) (patients HO, BE and WF). For the latter only occasional cells stained positive for both BSH and laminin could be found, whereas for the first type, none was found.

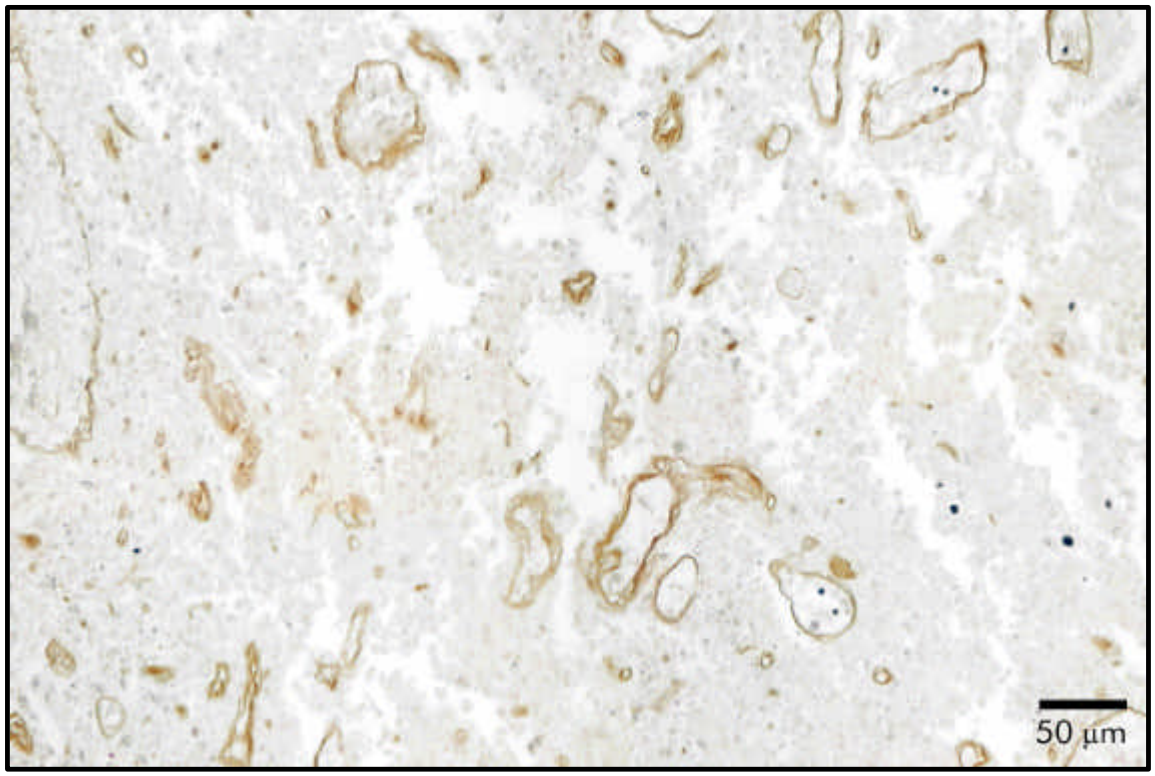

Fig. 21: In contrast to the other antigens used in this work, laminin (brown) often could be found in necrotic areas (hematoxylin counterstain, patient BE).

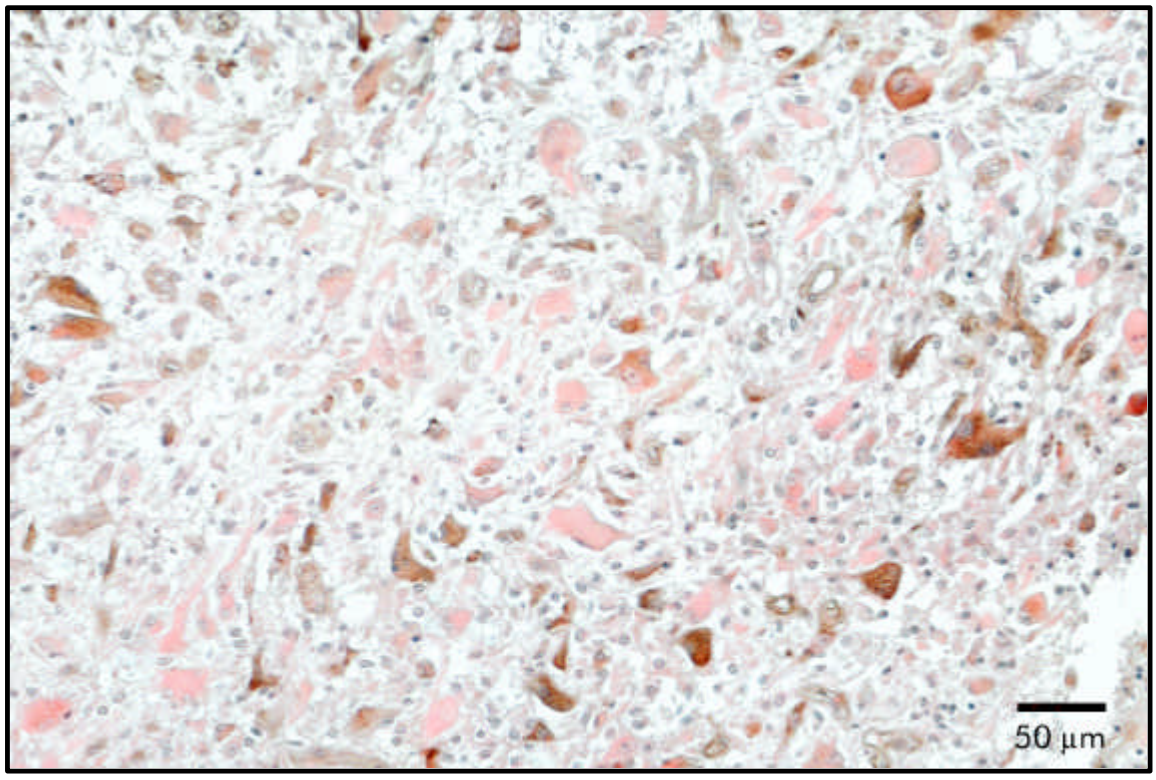

Fig. 22: In addition to the fibrillary staining pattern, laminin could be detected in the cytoplasm of single cells (hematoxylin counterstain, patient HO).

4.1.5 KI-67

Patient						
FJ	WB	HO	BE	JU	GO	WF
-	+ +	+	not tested	+ +	+ +	-

Table 11: Number of Ki-67-positive cells in comparison to tissue size: - no positive cells, + to + + + increasing number of positive cells/tissue area.

Ki-67 as a proliferation marker should be found strongly expressed in tumor tissue, due to its rapid growth. But in the tissue samples tested for Ki-67 only four of six showed positive staining. In the cases where Ki-67 could be found, no correlation of its localization and the distribution of BSH could be observed (Fig. 23)

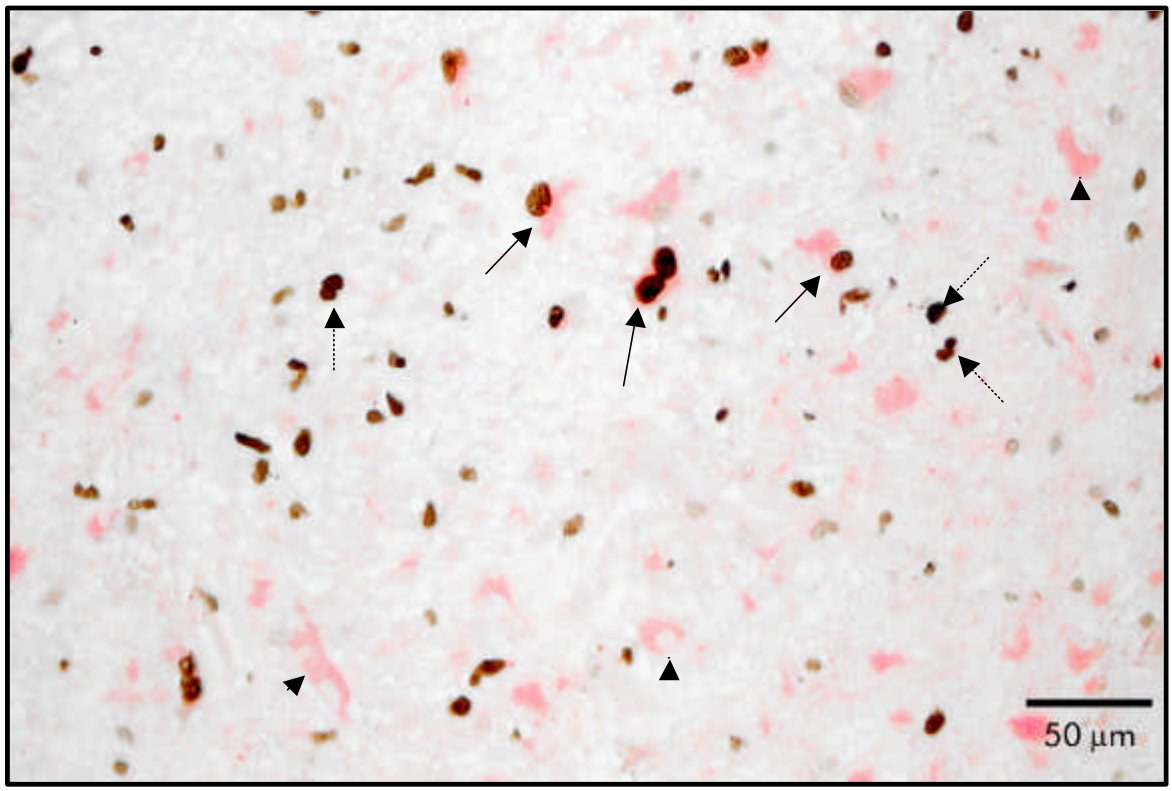

Fig. 23: Distribution of Ki-67expression and BSH uptake show no correlation. Some cells are positively stained for both antigens (solid arrows), some for BSH only (arrow heads) and some cells are only positive for Ki-67 (pointed arrows) (patient WB).

4.1.6 GFAP

Patient						
FJ	WB	HO	BE	JU	GO	WF
+ +	+ +	+ + +	+ +	+ + +	+ +	+ +

Table 12: Number of GFAP-positive cells in comparison to tissue size: - no positive cells, + to + + + increasing number of positive cells/tissue area.

Tissue samples from all patients gave strong staining for GFAP. However, only in sections of patients FJ, WF and JU, normal (star-shaped) astrocytes could be detected (Fig. 24), of which only some were positive for BSH and only in sections of JU.

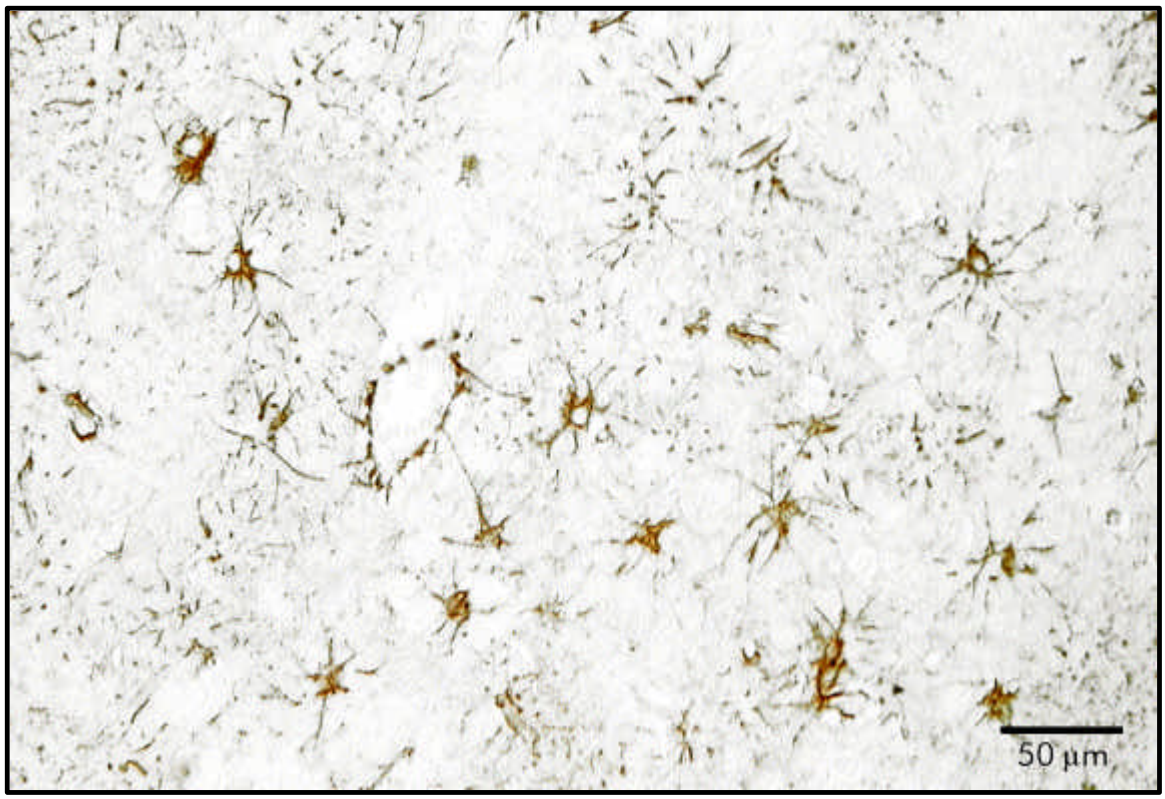

Fig. 24: Astrocytes can be distinguished by their star-shaped structure. They have long processes that attach to and cover the outer surface of blood vessels, thus limiting the entrance of molecules from the blood into the brain. These footplates form part of the blood-brain barrier (Abbott, 1987).

In all tissue samples most of the GFAP-positive cells showed neoplastic features (oversized, plump features without or shorten processes and nuclear pleomorphism) (Fig. 25). These cells showed a very high correlation with the staining for BSH (see also APPENDIX B).

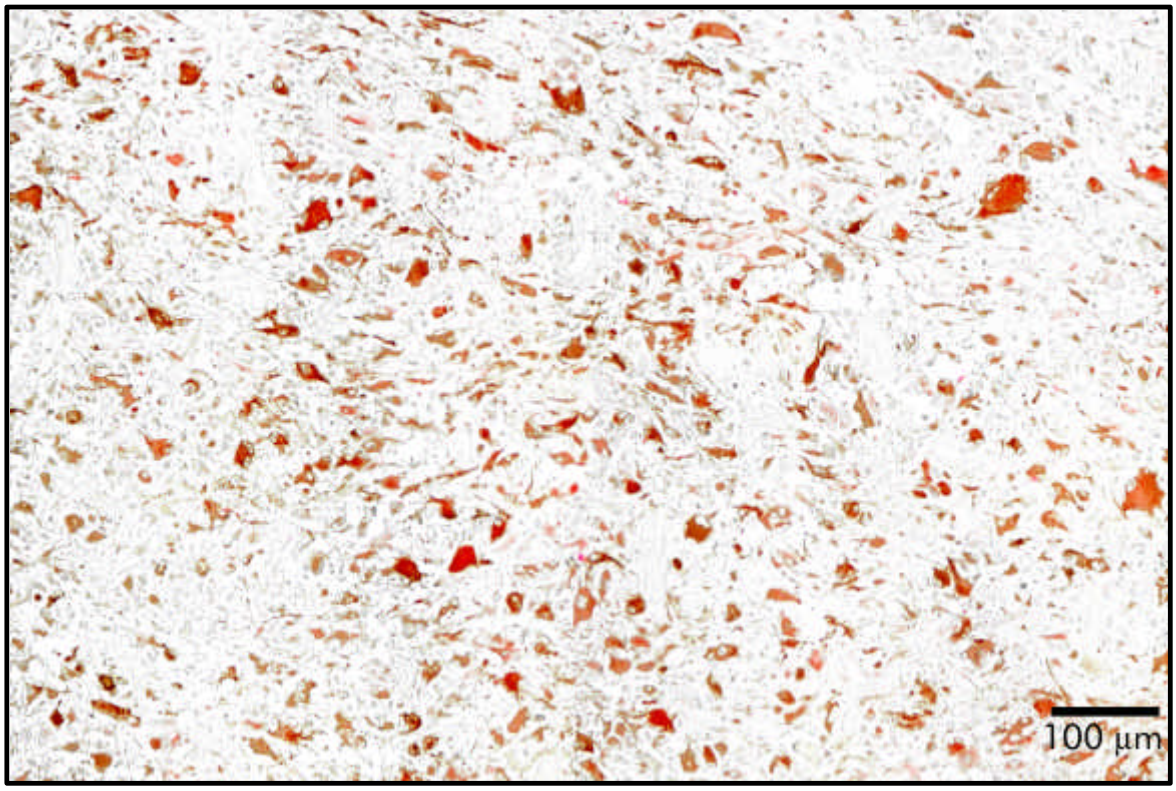

Fig. 25: A high correspondence between the distribution of GFAP-positive tumor cells of glial origin and BSH could be found in all tissue samples (patient HO).

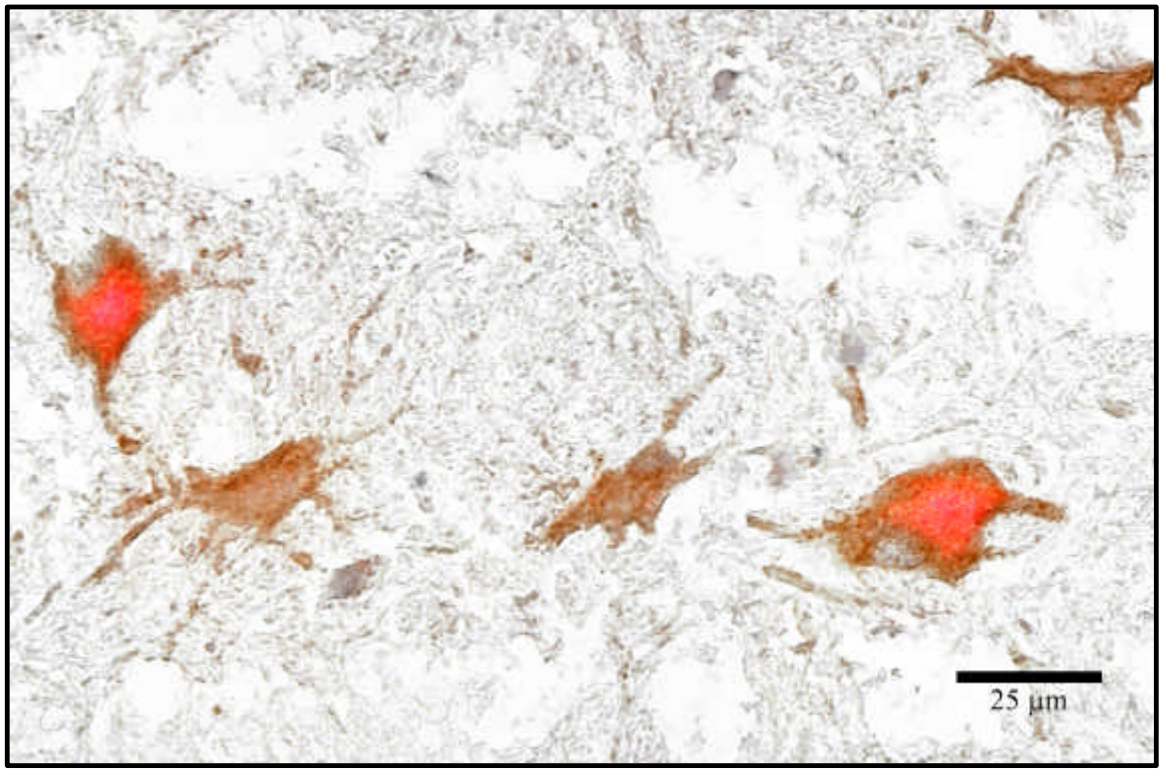

Fig. 26: Double staining of BSH (red) and GFAP (brown). Not all GFAP-positive cells contain BSH but in all but two patients nearly all BSH was in these cells (patient WF).

Because of the differences in the correlations of GFAP and BSH in the tumor samples of older patients (FJ, GO, HO, WF, WB) and younger patients (JU, BE), attempts were made to classify the glioblastomas according to their development (primary and secondary glioblastoma; see also 2.1 and Fig. 2). According to von Deimling et al. (1993) EGFR amplification occurs significantly more often in elderly patients with primary (de novo) glioblastoma. Lang et al. (1994) characterized primary glioblastoma as tumors without p53 mutation but with amplification of EGFR whereas for secondary glioblastoma p53 amplification and lack of EGFR overexpression are characteristic.

4.1.7 p53

Patient						
FJ	WB	HO	BE	JU	GO	WF
-	-	+	+	+ + +	-	+

Table 13: Number of p53-positive cells in comparison to tissue size: - no positive cells, + to + + + increasing number of positive cells/tissue area.

Only patient JU showed regions with high number of p53-positive cells. Although a local correlation between BSH and p53 could be found in patient JU, cells positive for both BSH and p53 were rare (Fig. 27).

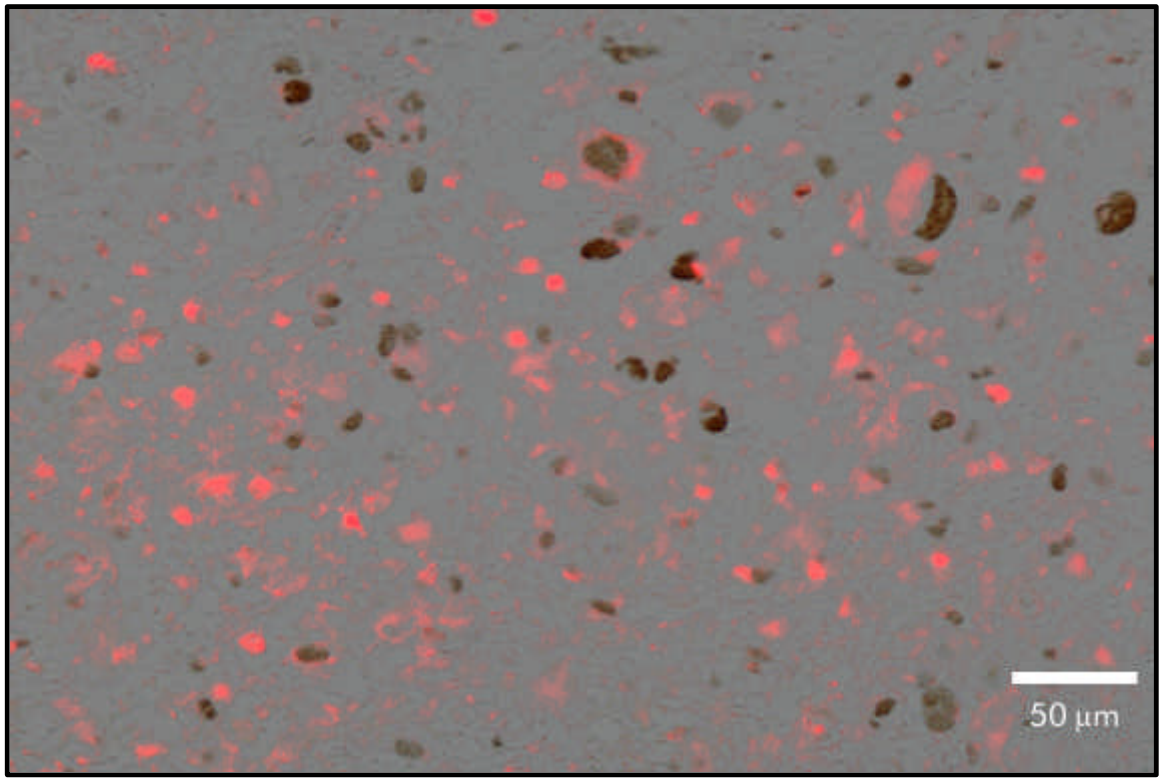

Fig. 27: A regional correspondence between the distribution of p53-positive cells (brown) and BSH (red) could be found in tissue sections of patient JU. However, positive staining for BSH and p53 in the same cell was rare.

4.1.8 EGFR

Patient						
FJ	WB	HO	BE	JU	GO	WF
+	+ + +	+ + +	+ +	-	+ +	+

Table 14: Number of EGFR-positive cells in comparison to tissue size: - no positive cells, + to + + + increasing number of positive cells/tissue area.

Two different types of EGFR-staining could be observed: A concentrated spot in the cytoplasm (Fig. 28) or staining of the cell membrane (Fig. 29). Only for the latter positive staining for BSH in the same cell could be found (Fig. 30). However, positive staining for both antigens in the same cell was rare.

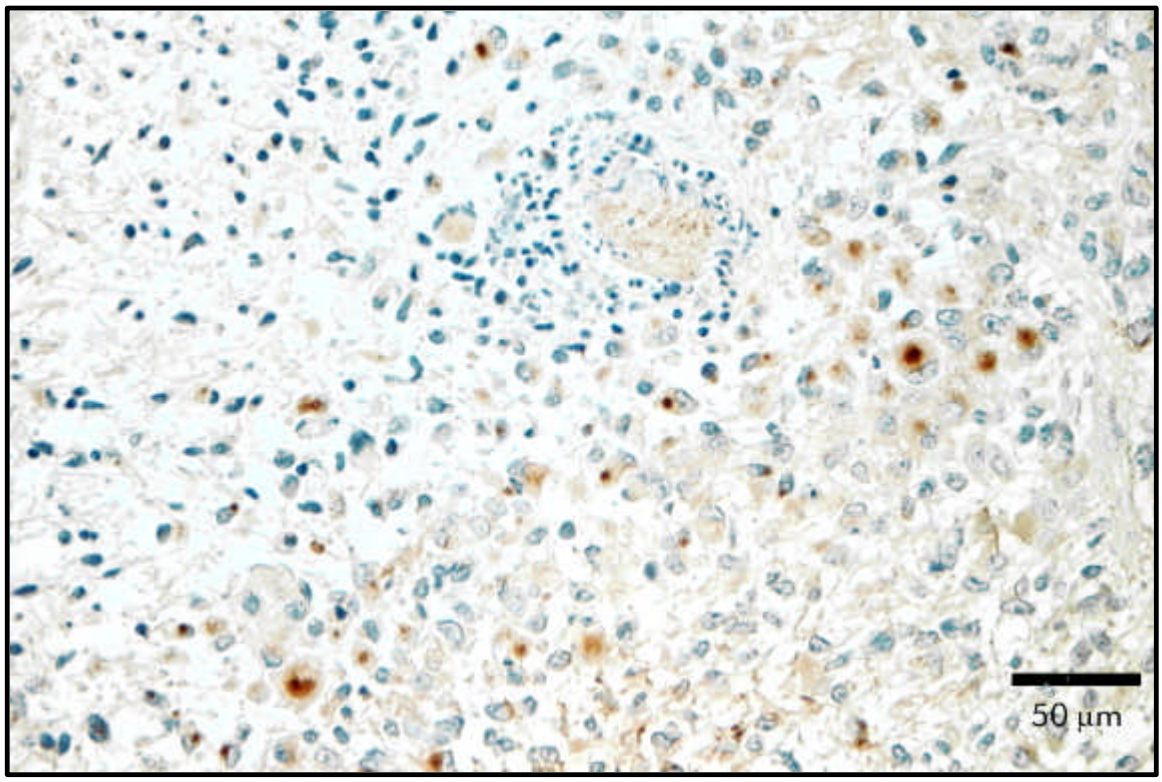

Fig. 28: Staining of EGFR (brown) in tumor tissue of patient WB (hematoxylin counterstain).

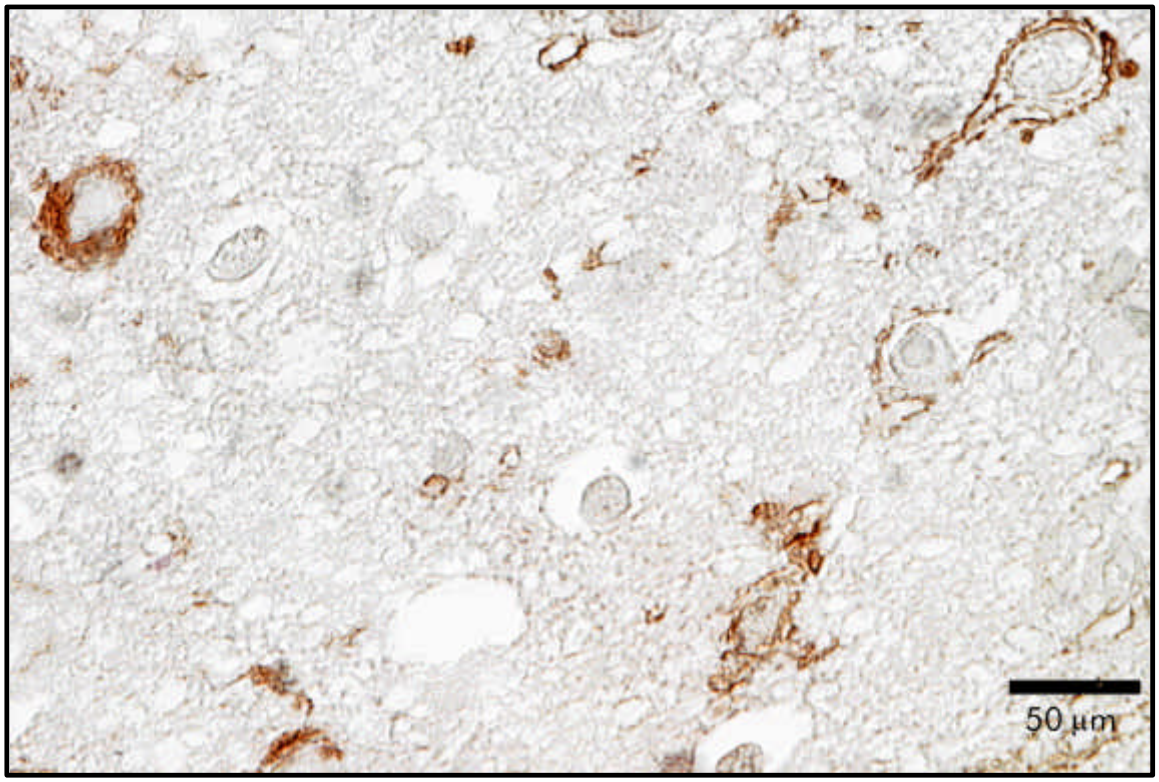

Fig. 29: Staining of EGFR in tumor tissue of patient BE. Only membrane like structures are stained.

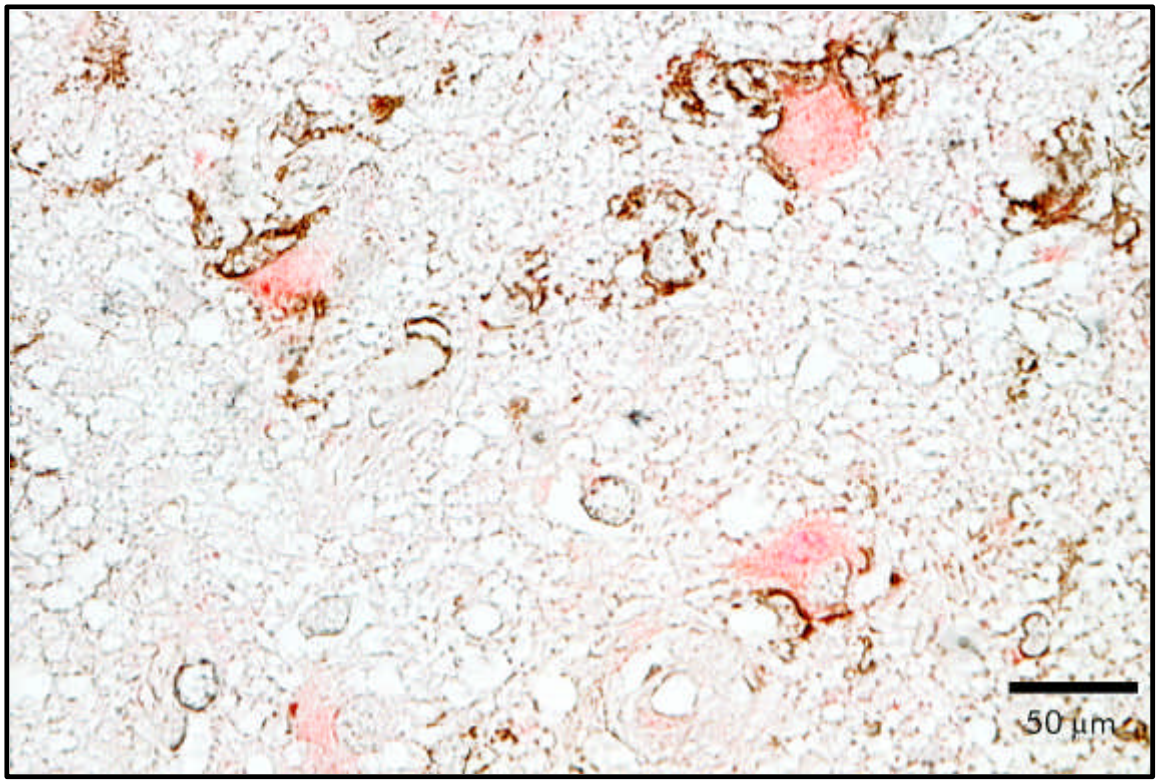

Fig. 30: Double staining of EGFR (brown) and BSH (red) in a tissue section of patient BE. Positive staining of both antigens in the same cell was rare.

On the basis of the staining results for p53 and EGFR the glioblastoma of patient JU seemed to be of secondary development, whereas for BE and WF no reliable statement could be given, the tumors of the four other patients were from primary development. These findings correlate with various studies that showed high incidents of primary glioblastoma in elderly patients whereas younger patients showed symptoms of secondary glioblastoma (von Deimling et al., 1993; Lang et al., 1994).

4.2 CONFOCAL LASER SCANNING MICROSCOPY

Double staining of thick sections (20 – 30 µm) were of limited success. Although labeling of antigens with FITC could be made, positive staining of BSH with Vector Red® could not be observed (Fig. 31 and 32).

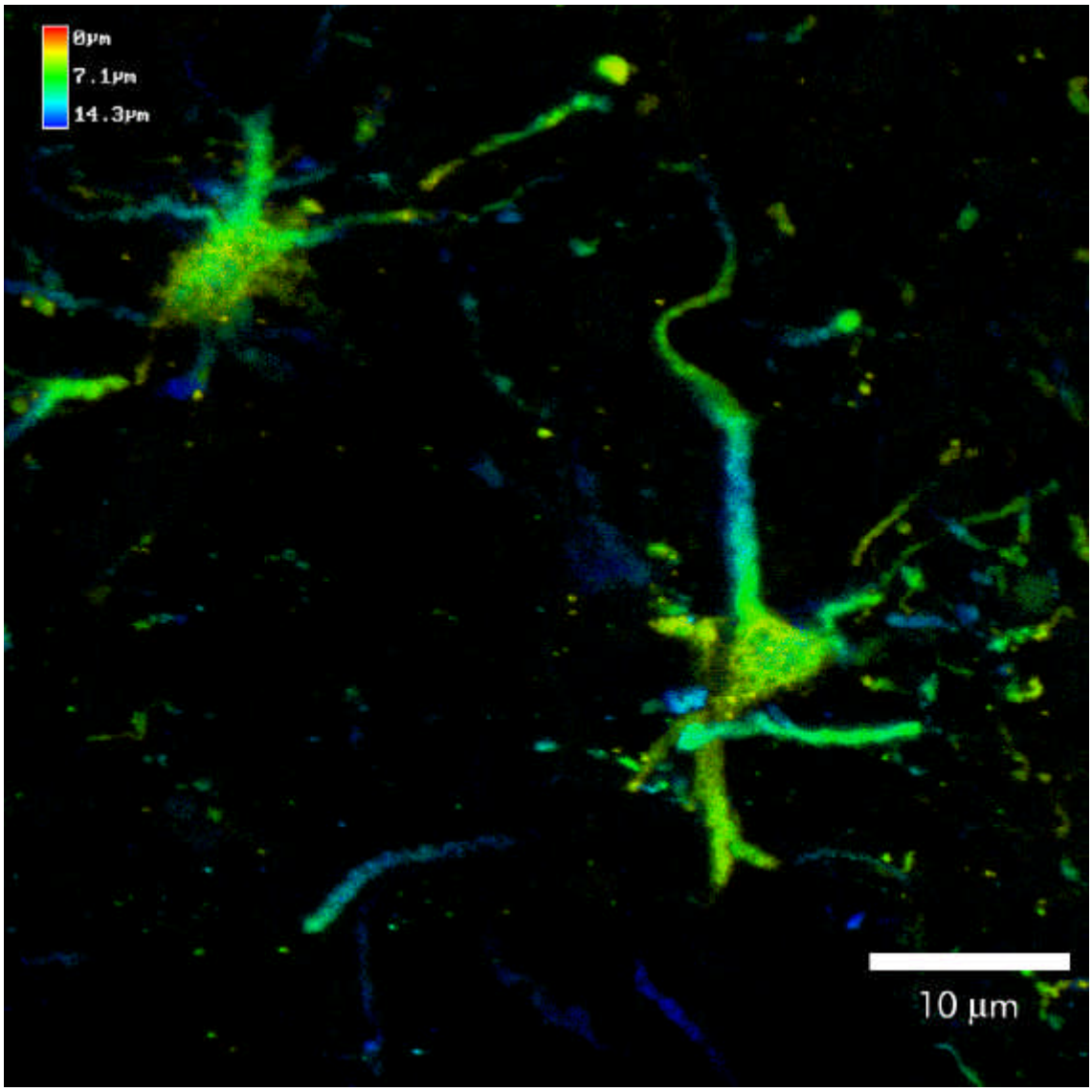

Fig. 31: Depth coded staining of GFAP in a 25-µm-section (patient WF).

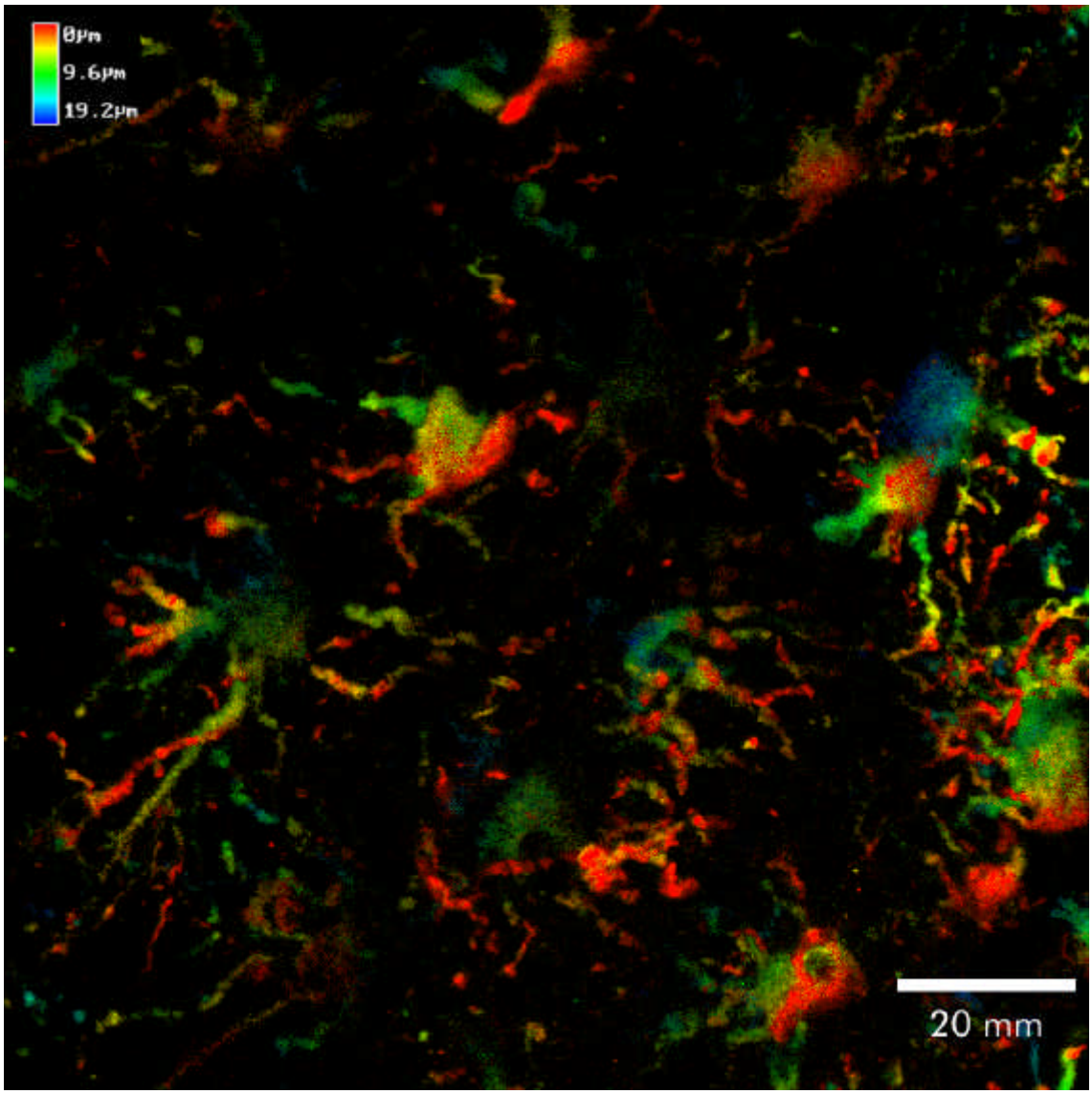

Fig. 32: Depth coded staining of GFAP in a 25-µm-section (patient WF).

The cause for failure of the BSH-staining could be due to the limited time during enzymatic precipitation of Vector Red®. According to the data sheet enzymatic activity stops after 40 min. In thick sections possibly two precipitation steps 30 min each would lead to better results. Because of the limited time in this study further experiments to this problem could not be executed.

4.3 X-RAY PHOTOELECTRON EMISSION SPECTROMICROSCOPY

Human glioblastoma tissue from two patients administered and one not administered with BSH were analyzed. As well as weak signals attributed to BSH, x-ray absorption spectra acquired from tissue samples detected boron in a reduced chemical state with respect to boron in BSH. This chemical state was characterized by a sharp absorption peak at 188.3 eV. Complementary studies on BSH reference samples were not able to reproduce this chemical state of boron, indicating that it is not an artifact produced during sample preparation or x-ray exposure. These data demonstrate that the chemical state of BSH may be altered by *in vivo* metabolism (see also APPENDIX C).

4.4 TRANSMISSION ELECTRON MICROSCOPE

Immunohistochemical labeling of BSH with gold revealed that almost all BSH was either inside the nucleus or associated with the cell membrane (Fig. 33) (see also APPENDIX D). This finding was confirmed by electron energy loss spectroscopy and electron spectroscopic imaging (APPENDIX D).

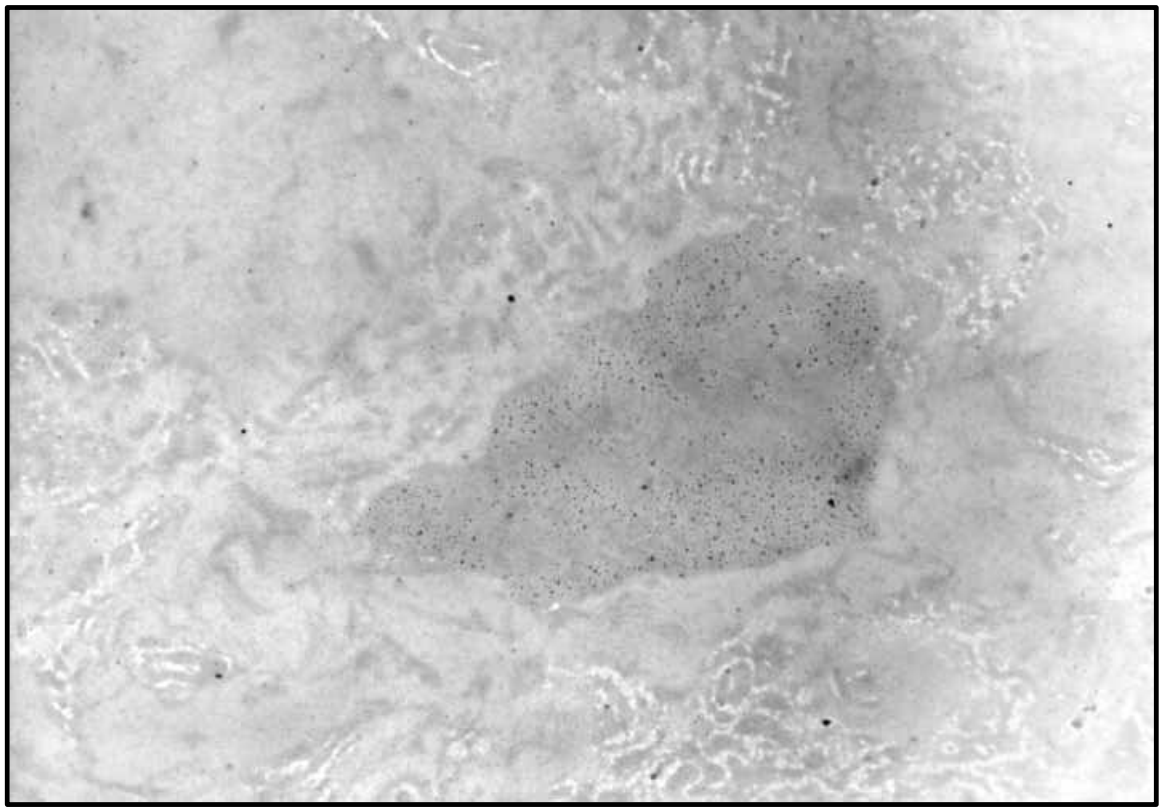

Fig. 33: A nucleus stained positively for BSH (black spots). Almost all BSH could be found inside of nuclei (patient GO).

Due to suboptimal freezing and storage, all tumor samples available for this work were of bad morphological condition. Organelles could rarely be found with exception of nuclei. Because of the unique study from which these samples were obtained no other BSH-containing tumor material was available. Therefore GAMG-spheroids were prepared and incubated with medium containing 1 mM Na_2BSH for 24 h and 48 h. After washing in PBS (pH 7.4) spheroids were fixed and embedded in the same manner like the human tumor samples before (see also 3.6). Unfortunately no BSH could be found neither directly by EELS/ESI nor indirectly by immunogold-labeling in TEM. To clarify this finding, the BSH-

uptake in spheroids was quantitatively evaluated by ICP-MS (Fig. 34; for preparation see 3.8).

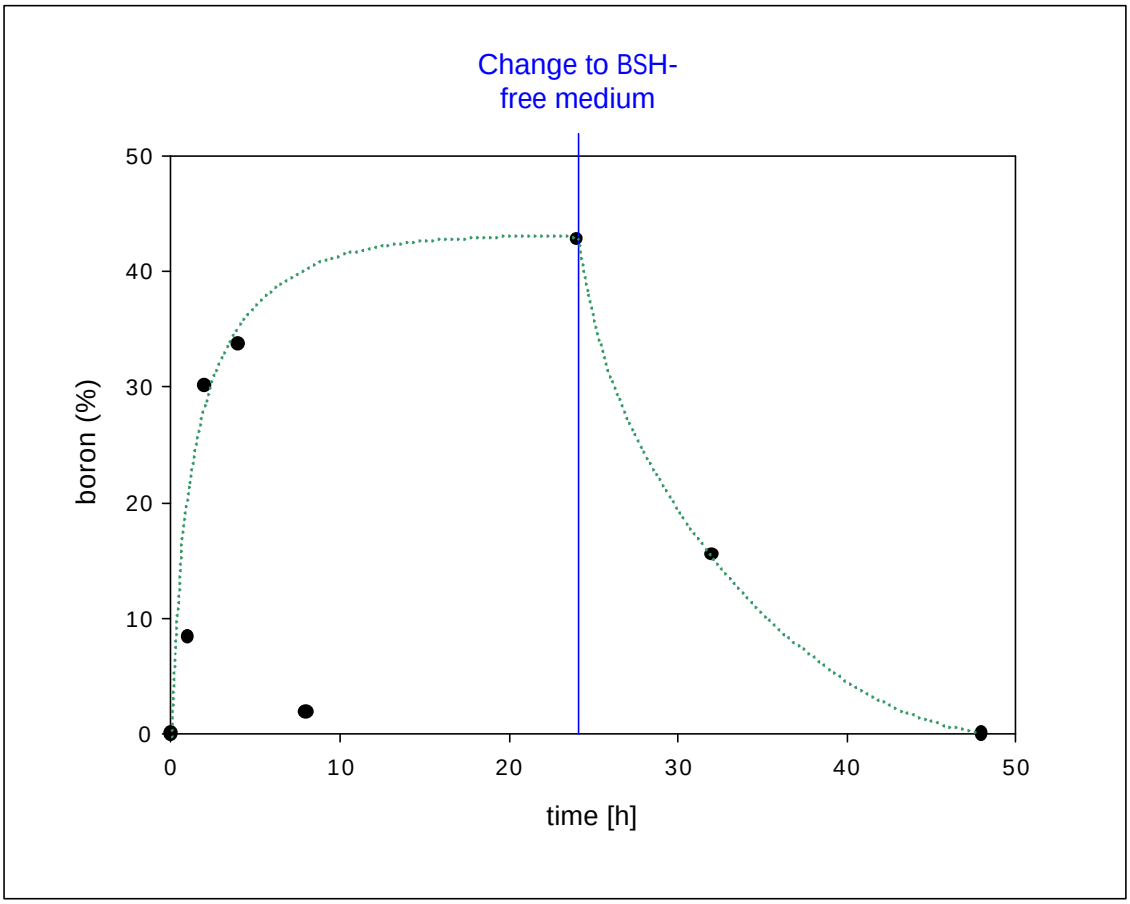

Fig. 34: Boron content in GAMG-spheroids in percent of the dry weight. The value after 8 h did not follow the common trend and is probably an error of measurement. After the initial strong increase BSH-uptake seem to flatten after 24 h. All boron was lost after change to BSH-free medium within 24 h.

These results suggest a fast uptake of BSH in spheroids without firm binding. After change to boron-free medium all BSH was washed out. These findings agree with other studies on BSH localization in tumor cells. Intracellular boron in BSH treated glioblastoma cells measured by ion microscopy was decreased dramatically within 1 h after change to BSH-free medium (Zha et al., 1992).

According to these results, loss during fixation and embedding seem be the cause of the failed detection of BSH in GAMG-spheroids.

5 DISCUSSION

The reason for selective BSH accumulation in tumor cells is yet not clear even today, after almost 25 years of clinical use, are yet not clear. BSH is excluded from healthy brain tissue because of the blood-brain-barrier that is disrupted in tumor regions, thus allowing BSH to enter the tissue. However, a disrupted blood-brain-barrier alone is not sufficient to explain the selectivity of BSH for tumor tissue. In this work accumulation of BSH predominantly in GFAP-positive tumor cells of glial origin could be shown by immunohistochemistry in all investigated tissue samples.

This makes the following uptake mechanism possible: Because of a defective blood-brain barrier BSH can diffuse from blood to astrocytes, which cover the blood vessel like a coat (Fig. 35).

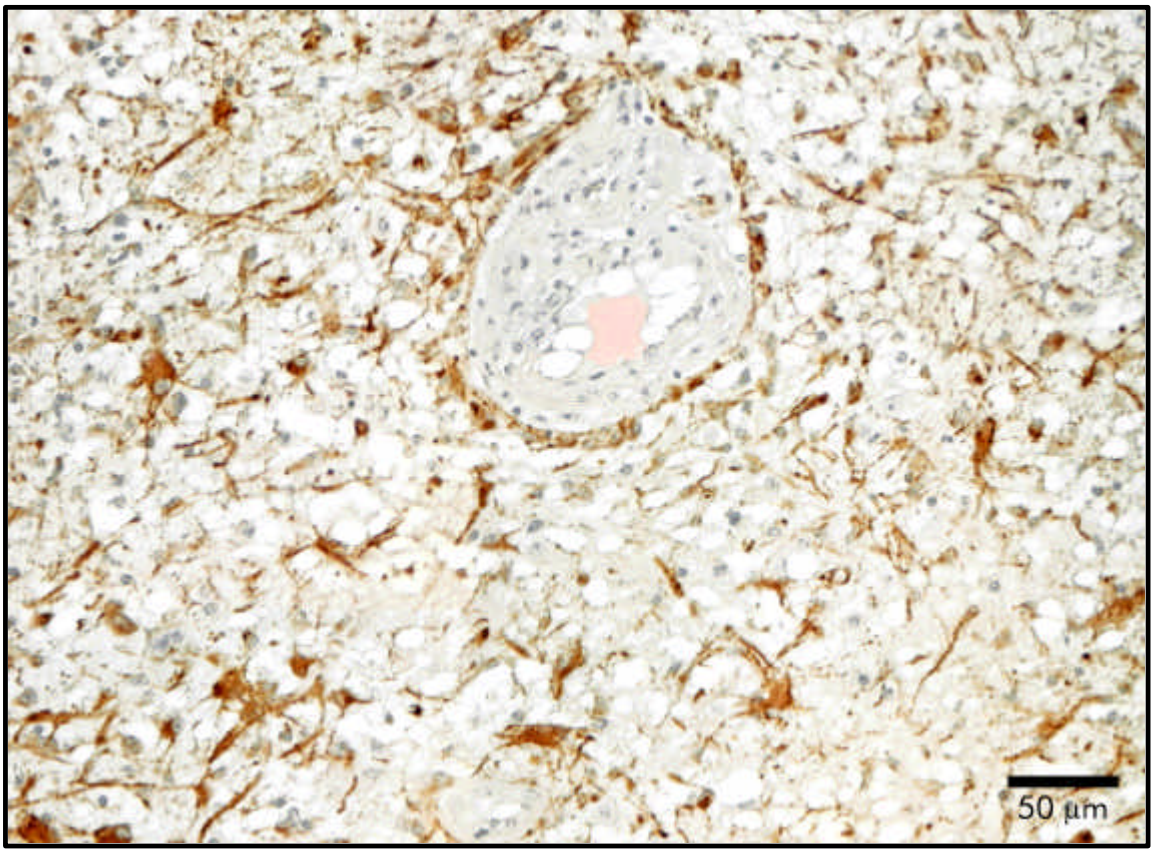

Fig. 35: Astrocytes stained for GFAP in brown covering a blood vessel which contains blood stained for BSH in red (patient WF, hematoxylin counterstain).

This could lead to a selective uptake of BSH in cells of glial origin in the environment of blood vessels, which could be observed occasionally in this work (Fig. 36).

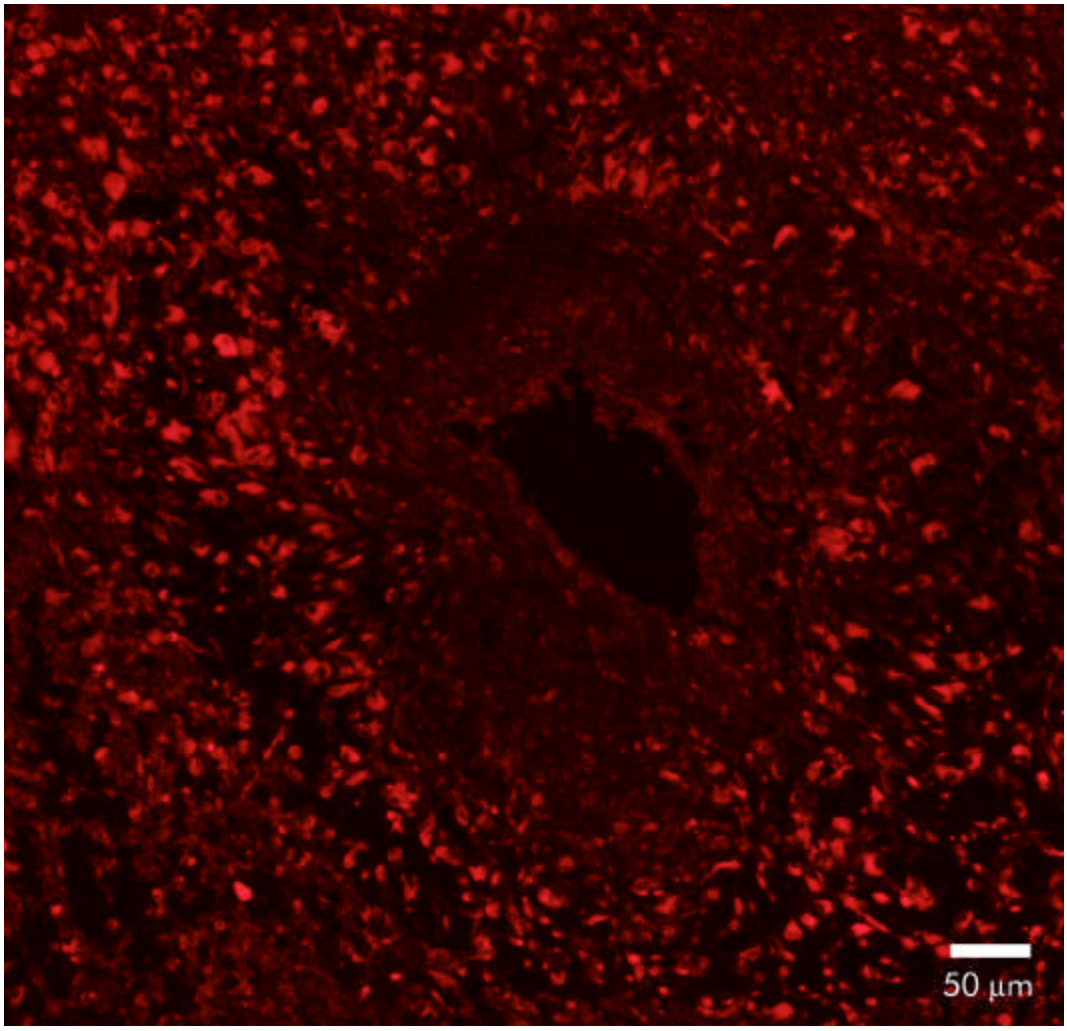

Fig. 36: High number of BSH-positive cells (red) surrounding a blood vessel (center) (patient WB).

Mutations during tumor progression in glial cells could be responsible for the two age-depending groups of glioblastoma tissue, which differ in the rate of correspondence of BSH- and GFAP-positive cells. This would give mutations in glial cells during tumor development a key position in the selective uptake of BSH in glioblastoma multiforme.

Because of different progression pathways for glioblastoma and the resulting differences in genetic alterations, approaches to receptor-mediated targeting, like boron-containing bioconjugates of EGF (Carlsson et al., 1993; Capala et al., 1996), could be of limited usefulness. Strong EGFR-expression could only be found in four of seven patients in this study. This approach would require immunohistochemical detection of EGFR (or the individual receptor used for targeting tumor cells) prior to determination of the boron carrier in BNCT.

Difficult to explain were the two different subcellular distribution patterns for BSH. While electron microscopic studies demonstrated BSH predominantly associated with the cell membrane and the chromatin, BSH visualized by enzymatic precipitation of Vector red could only be found in the cytoplasm. This would be in contradiction with earlier immuno-histochemical studies, which showed BSH also in nuclei of tumor cells (Otersen et al., 1997). In fact, after careful screening of cells stained for BSH, it could also be found in nuclei, in the immediate surrounding of nucleoli (Fig. 37).

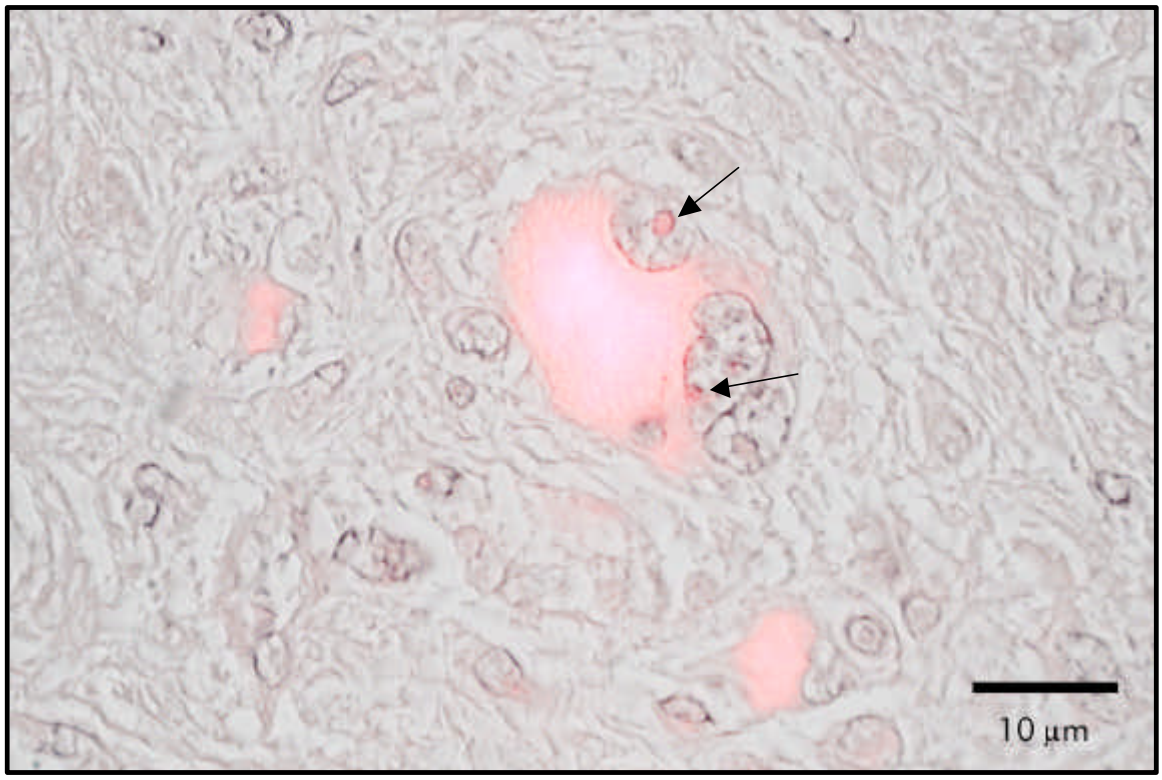

Fig. 37: BSH stained in red could also be found in the nuclei (arrows) (patient WB).

But the number of nuclei stained for BSH for fluorescence microscopy was rare compared to those stained by immunogold-labeling for transmission electron microscopy. Possibly the detection of BSH interacting with the chromatin by enzymatic precipitation of Vector red is reduced due to steric influences.

On the other hand, BSH could be found in the cytoplasm only in light and fluorescence microscopy but neither in immunogold-labeling for TEM nor in EELS/ESI. This discrepancy could be explained by the different thickness of the sections for light and electron microscopic studies. Sections of 5-µm thickness in most cases would show a substantial part of the membrane surface whereas 50-nm sections for electron microscopic studies always show only a membrane ring or very rarely a spot (Fig. 38).

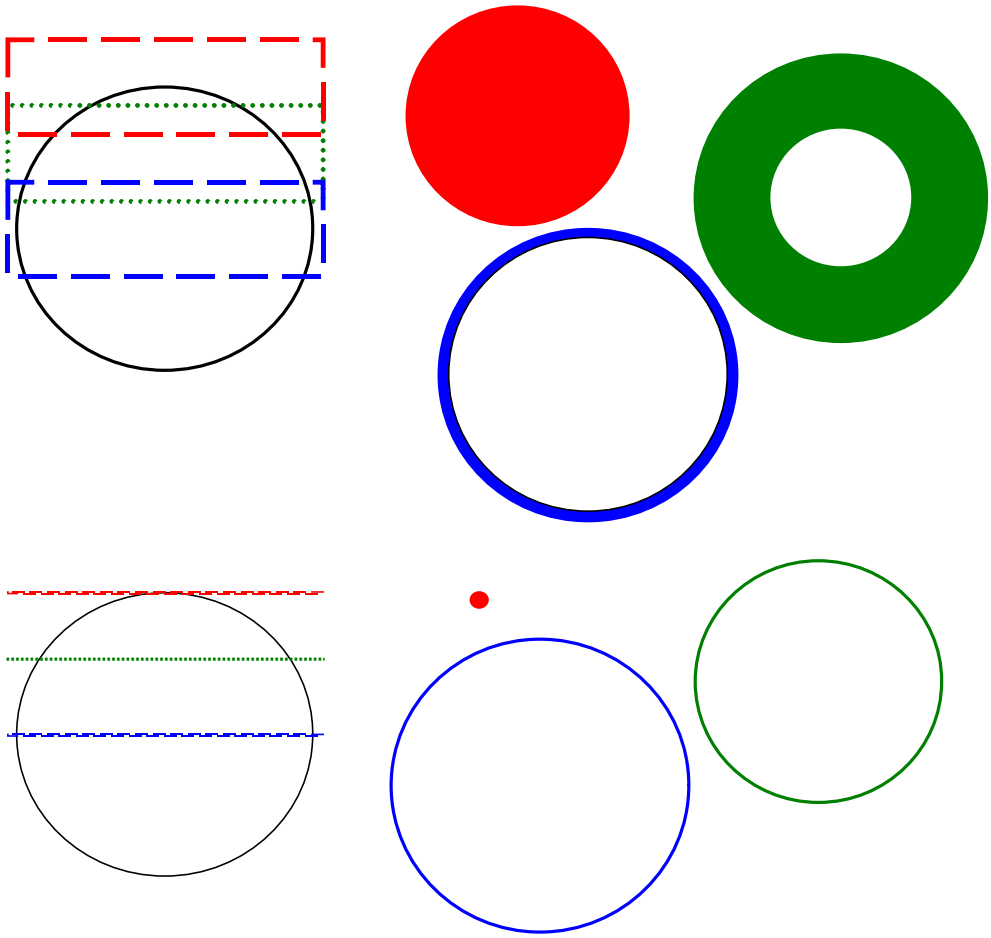

Fig. 38: Three section of 5 µm and 50 nm thickness through a round cell with a diameter of 15 µm and the resulting figures after membrane staining (colored area = membrane).

In this way the apparent staining of the cytoplasm in light and fluorescence microscopy could originate from the stained membrane, and thus reconciling these results with the results obtained by TEM.

The high concentration of BSH near the cell membrane supports the hypothesis that BSH enters the cell by endocytosis (Otersen et al., 1996). Investigations by Lutz et al. (2000) showed an interaction of the double negatively charged BSH with the positive choline head groups of phosphatidylcholine, which is enriched in tumor cells in the extracellular part of the membrane (Fulham et al., 1992; Ott et al., 1993). Normal glial cells, glioma cell lines from rat (Bjerknes et al. 1987) and tumor cells show an increased phagocytic activity. As a result of endocytosis, BSH would occur within cells, encapsulated in vesicles rich in phosphatidylcholine. From there, two pathways are possible:

- Membrane components involved in the endocytic pathway are disassembled and recycled. In this way, it is possible that BSH remains bound to choline residues that are detached from membranes. Such electrically neutral compound could diffuse through the cell and also pass nuclear pores. If BSH interacts with components of the chromatin this could lead to an accumulation of boron in nuclei.

- BSH containing vesicles fuse with the membrane of the endoplasmatic reticulum and move to the inner nuclear membrane by lateral diffusion. Retention in the inner nuclear membrane could occur as a result of interaction with nucleoplasmic proteins like lamins or chromatin proteins.

By x-ray photoelectron emission spectromicroscopy boron was found in a reduced chemical (with respect to boron in BSH) as shown by the x-ray absorption peak at 188.3 eV. This peak was found across 40 % of the tissue regions analyzed and never from the control patient. The reduced boron species was found in tissue in the same general areas, which stained positive for BSH in light microscopy. The x-ray absorption feature at 188.3 eV could not be produced by ashing, nor with x-ray induced photochemistry. Therefore, this work presents for the first time evidence that a proportion of the BSH injected into the patient could have been bound or metabolized *in vivo*.

6 REFERENCES

Abbott NJ: Neurobiology. Glia and the blood-brain barrier. *Nature* 325: 195, 1987.

Agarwal ML, Agarwal A, Taylor WR, Stark GR: p53 controls both the G2/M and the G1 cell cycle checkpoints and mediates reversible growth arrest in human fibroblasts. *Proc Natl Acad Sci USA* 92: 8493-8497, 1995.

Amano K: Boron-10-mercaptoundecahydrodo-decaborate distribution in human brain tumors as studied by neutron-induced alpha-autoradiography. In: Hatanaka H (ed) Boron Neutron Capture Therapy for Tumors. Nishimura, Niigata: 107-115, 1986.

Amelinckx S, van Dyck D, van Landuyt J, vanTendeloo G: Electron microscopy – Principles and fundamentals. Weinheim, VCH, 1997.

Ariza A, Fernandez LA, Inagami T: Renin in glioblastoma multiforme and its role in neovascularization. *Am J Clin Pathol* 90: 437-441, 1988.

Aruffo A, Stamenkovic I, Melnick M, Underhill CB, Seed B: CD44 is the principal cell surface receptor for hyaluronate. *Cell* 61: 1303 - 1313, 1990.

Bailey P, Cushing H. Cited by: Rubenstein LJ. Tumors of the central nervous system. In: Atlas of tumor pathology. Washington, DC: Armed Forces Institute of Pathology 13, 1972.

Barak Y, Juven T, Haffner R, Oren M: mdm2 expression is induced by wild type p53 activity. *EMBO J* 12: 461-468, 1993.

Barth RF, Soloway AH, Goodman JH, Gahbauer RA, Gupta N, Blue TE, Yang W, Tjarks W: Boron neutron capture therapy of brain tumors: An emerging therapeutic modality. *Neurosurg* 44: 433-450, 1999.

Battifora H, Kopinski M (1986) The influence of protease digestion and duration of fixation on the immunostaining of keratins. A comparison of formalin and ethanol fixation. *J Histochem Cytochem* 34: 1095–1100.

Bignami A, Dahl D: Specifity of the glial fibrillary acidic protein for astroglia. *J Histochem Cytochem* 25: 466-469, 1977.

Bigner SH, Burger PC, Wong AJ, Werner MH, Hamilton SR, Muhlbaier LH, Vogelstein B, Bigner DD: Gene amplification in malignant human gliomas: clinical and histopathologic aspects. *J Neuropathol Exp Neurol* 47: 191-205, 1988.

Bondy ML, Wrensch M: Update on brain cancer epidemiology. *Bull Cancer* 45: 365-369, 1993.

Boring CC, Squires TS, Tong T. Cancer statistics. *CA Cancer J Clin* 43: 7-26, 1993.

Bruner JM. Neuropathology of malignant gliomas. *Semin Oncol* 21: 126-138, 1994.

Capala J, Barth RF, Bendayan M, Lauzon M, Adams D, Soloway AH, Carlsson J: Boronated epidermal growth factor as a potential targeting agent for boron neutron capture therapy of brain tumors. *Bioconjug Chem* 7: 7-.15, 1996.

Carlsson J, Gedda L, Grönvik C, Hartman T, Lindström A, Lindström P, Olsson P, Pontén J, Sjöberg S, Westermark B: Strategy for boron neutron capture therapy against brain tumor cells with overexpresion of the epidermal growth factor receptor. *Int J Radiat Oncol Biol Phys* 30: 105-115, 1993.

Ceberg CP, Persson A, Brun A, Huiskamp R, Fyhr A-S, Persson BRR, Salford LG: Performance of sulfhydryl boron hydride in patients with grade III and IV astrocytoma: a basis for boron neutron capture therapy. *J Neurosurg* 83: 79-85, 1995.

Chung-Welch N, Patton WF, Shepro D, Cambria RP: Human omental microvascular endothelial and mesothelial cells: characterization of two distinct mesodermally derived epithelial cells. *Microvasc Res* 54: 108-120, 1997a.

Chung-Welch N, Patton WF, Shepro D, Cambria RP: Two-stage isolation procedure for obtaining homogenous populations of microvascular endothelial and mesothelial cells from human omentum. *Microvasc Res* 54: 121-134, 1997b.

Cioce V, Margulies IM, Sobel ME, Castronovo V: Interaction between the 67 kilodalton metastasis-associated laminin receptor and laminin. *Kidney Int* 43: 30-37, 1993.
Colliex C: Electron energy-loss spectroscopy analysis and imaging of biological specimens. *Ann NY Acad Sci* 483: 311, 1986.

Collins VP: Amplified genes in human gliomas. *Semin Cancer Biol* 4: 27-32, 1993.

Curran RC, Gregory J: The unmasking of antigens in paraffin sections of tissue by trypsin. *Experientia* 33: 1400-1401, 1977.

Davis FG, Freeks S, Grutsch J, Barlas S, Brem S: Survival rates in patients with primary malignant brain tumors stratified by patient age and tumor histological type: An analysis based on surveillance, epidemiology and end results (SEER) data 1973-1991. *J Neurosurg* 88: 1-10, 1998.

Debiec-Richter M, Liberski PP. Molecular changes involved in the carcinogenesis of brain tumors. Folia Neuropathol 32: 199-203, 1994.

Delpech D, Delpech A, Vidard MN, Girard N, TayotJ, Clement JC, Creissard P: Glial fibrillary acidic protein in tumors of the nervous system. *Br J Cancer* 37: 33-40, 1978.

De Stasio G, Capozi M, Lorusso GF, Baudat PA, Droubay TC, Perfetti P, Margaritondo G, Tonner BP: MEPHISTO: a Novel Synchrotron Imaging Photoelectron Microscope. *Rev Sci Instrum* 69: 2062-2067, 1998.

De Stasio G, Perfetti L, Gilbert B, Fauchoux O, Capozi M, Perfetti P, Margaritondo G, Tonner BP: The MEPHISTO Spectromicroscope Reaches 20 nm Lateral Resolution. *Rev Sci Instrum* 70: 1740-1742, 1999.

Duchrow M, Schluter C, Key G, Kubbutat MH, Wohlenberg C, Flad HD, Gerdes J. Cell proliferation-associated nuclear antigen defined by antibody Ki-67: a new kind of cell cycle-maintaining proteins. *Arch Immunol Ther Exp (Warsz)* 43: 117-121, 1995

Ekstrand AJ, James CD, Cavenee WK, Seliger B, Pettersson RF, Collins VP: Genes for epidermal growth factor receptor, transforming growth factor alpha, and epidermal growth factor and their expression in human gliomas in vivo. *Cancer Res* 51: 1427-1433, 1992.

El-Deiry WS, Harper JW, O'Connor PM, Velculescu VE, Canman CE, Jackman J, Pietenpol JA, Burrell M, Hill DE, Wang Y: WAF1/CIP1 is induced in p53-mediated G1 arrest and apoptosis. *Cancer Res* 54: 1169-1174, 1994.

El-Deiry WS, Tokino T, Waldman T, Oliner JD, Velculescu VE, Burrell M, Hill DE, Healy E, Rees JL, Hamilton SR: Topological control of p21WAF1/CIP1 expression in normal and neoplastic tissues. *Cancer Res* 55: 2910-2919, 1995.

Evers P, Uylings HBM (1994) Microwave-stimulated antigen retrieval is pH and temperature dependent. *J Histochem Cytochem* 42: 1555–1563.

Finkel GC, Poletti CE, Fairchild RG, Slatkin DN, Sweet WH: Distribution of ^{10}B after infusion of $Na_2B_{12}H_{11}SH$ into a patient with malignant astrocytomas: implication for boron neutron capture therapy. *Neurosurgery* 24: 6-11, 1989.

Finlay CA, Hinds PW, Levine AJ: The p53 proto-oncogene can act as a suppressor of transformation. *Cell* 57: 1083-93,1989.

Fox CH, Johnson FB, Whiting J, Roller PP: Formaldehyde fixation. *J Histochem Cytochem* 33: 845–853, 1985.

Fox SB, Fawcett J, Jackson DG: Normal human tissues, in addition to some tumors, express multiple different CD44 isoforms. *Cancer Res* 54 : 4539-4546, 1994.

Fraenkel–Conrat H, Brandon BA, Olcott HS: The reaction of formaldehyde with proteins. IV. Participation of indole groups. Gramicidin. *J Biol Chem* 168: 99-118, 1947.

Fraenkel–Conrat H, Olcott HS: Reaction of formaldehyde with proteins. VI. Cross-linking of amino groups with phenol, imidazole, or indole groups. *J Biol Chem* 174: 827-843, 1948a.

Fraenkel–Conrat H, Olcott HS: The reaction of formaldehyde with proteins. V. Cross-linking between amino and primary amide or guanidyl groups. *J Am Chem Soc* 70: 2673-2684, 1948b.

Gabel D, Foster S, Fairchild RG: The Monte Carlo simulations of the biological effect of the $^{10}B(n,\alpha)^7Li$ reaction in cells and tissue and its implication for boron neutron capture therapy . *Radiat Res* 111: 14-25, 1987.

Greenblatt MS, Bennett WP, Hollstein M, Harris CC: Mutations in the p53 tumor suppressor gene: clues to cancer etiology and molecular pathogenesis. *Cancer Res* 54: 4855-78, 1994.

Grossfeld GD, Shi S-R, Ginsberg DA, Rich KA, Skinner DG, Taylor CR, Cote RJ: Immunohistochemical detection of thrombospondin-1 in formalin-fixed, paraffin-embedded tissue. *J Histochem Cytochem* 44: 761-766, 1996.

Gunthert U, Hofmann M, Rudy W, Reber S, Zoller M, Haussmann I, Matzku S, Wenzel A, Ponta H, Herrlich P: A new variant of glycoprotein CD44 confers metastatic potential to rat carcinoma cells. *Cell* 65: 13–24, 1991.

Haapasalo H, Isola J, Sallinen P, et al. Aberrant p53 expression in astrocytic neoplasms of the brain: association with proliferation. *Am J Pathol* 142: 1347-1351, 1993.

Haritz D, Gabel D, Klein H, Piscol K: Clinical investigations in boron neutron capture therapy (BNCT). Pharmacokinetics, biodistribution and toxicity of $Na_2B_{12}H_{11}SH$ (BSH) in patients with malignant glioma. *Adv Neurosurg* 20: 247-252, 1992.

Haritz D, Gabel D, Huiskamp R: Clinical phase-I study of $Na_2B_{12}H_{11}SH$ (BSH) in patients with malignant glioma as precondition for boron neutron capture therapy (BNCT). *Int J Radiation Oncology Biol Phys* 28: 1175, 1994.

Harrach B, Robenek K: Polyclonal antibodies against formaldehyde–modified apolipoprotein A–1. An approach to circumventing fixation–induced loss of antigenicity in immunohistochemistry. *Arteriosclerosis*: 564–576, 1990.

Haselsberger K, Radner H, Gössler W, Schlagenhaufen C, Pendl G: Subcellular boron-10 localization in glioblastoma for boron neutron capture therapy with $Na_2B_{12}H_{11}SH$. *J Neurosurg* 81: 741-744, 1994.

Hatanaka H: Clinical results of boron neutron capture therapy; *in:* Harling OH, Bernard JA, Zamenhof RG (eds): Proceedings of an International Workshop on neutron beam design, development and performance for neutron capture therapy, Massachusetts Institute of Technology, Cambridge: 29-31, 1989.

Hatanaka H, Nakagawa Y: Clinical results of long-surviving brain tumor patients who underwent boron neutron capture therapy. *Int J Radiation Oncology Biol Phys* 28: 1061-1066, 1994.

Heidebrecht HJ, Buck F, Haas K, Wacker HH, Parwaresch R: Monoclonal antibodies Ki-S3 and Ki-S5 yield new data on the 'Ki-67' proteins. *Cell Prolif* 29: 413-425, 1996.

Huang SN: Immunohistochemical demonstration of hepatitis B core and surface antigens in paraffin sections. *Lab Invest* 33: 88–95, 1975.

Huang S, Chakrabarty S: Regulation of fibronectin and laminin receptor expression, fibronectin and laminin secretion in human colon cancer cells by transforming growth factor-beta 1. *Int J Cancer* 57: 742-746, 1994.

Hunter T: The epidermal growth factor receptor gene and its product. *Nature* 311: 414-416, 1984.

Hurtt MR, Moossy J, Donovan-Peluso M, Locker J: Amplification of epidermal growth factor receptor gene in gliomas: histopathology and prognosis. *J Neuropathol Exp Neurol* 51: 84-90, 1992.

James CD, Carlbom E, Dumanski JP, Hansen M, Nordenskjold M, Collins VP, Cavenee WK: Clonal genomic alterations in glioma malignancy stages. *Cancer Res* 48: 5546-51,1988.

Javid M, Brownell GL, Sweet WH: The possible use of neutron capture isotopes such as boron-10 in the treatment of neoplasms: II-Computation of the radiation energy and estimates of effects in normal and neoplastic brain. *J Clin Invest* 31: 603-610, 1952.

Kastan MB, Onyekwere O, Sidransky D, Vogelstein B, Craig RW: Participation of p53 protein in the cellular response to DNA damage. *Cancer Res* 51: 6304-6311, 1991.

Kastan MB, Zhan Q, el-Deiry WS, Carrier F, Jacks T, Walsh WV, Plunkett BS, Vogelstein B, Fornace AJ Jr.: A mammalian cell cycle checkpoint pathway utilizing p53 and GADD45 is defective in ataxia-telangiectasia. *Cell* 71: 587-597, 1992.

Kleihues P, Burger PC, Scheithauer BW. The new WHO classification of brain tumours. *Brain Pathol* 3: 255-268, 1993.

Kleihues P, Ohgaki H: Genetics of glioma progression and the definition of primary and secondary glioblastoma. *Brain Pathol* 7: 1131-1136, 1997.

Kleihues P, Cavenee WK: Pathology and Genetics of Tumours of the Nervous System, International Agency for Research on Cancer, Lyon, 1997.

Kobayashi T, Kanda K: Analytical calculation of boron-10 dosage in cell nucleus for neutron capture therapy. *Radiat Res* 91: 77-94, 1982.

Kortmann RD, Becker G, Kühl J, Bamberg M: Strahlentherapie bei malignen Gliomen. *Der Onkologe* 4: 608-617, 1998.

Kuerbitz SJ, Plunkett BS, Walsh WV, Kastan MB: Wild-type p53 is a cell cycle checkpoint determinant following irradiation. *Proc Natl Acad Sci USA* 89: 7491-7495, 1992.

Lane DP: Cancer. p53, guardian of the genome. *Nature* 358: 15-16, 1992.

Lang FF, Miller DC, Koslow M, Newcomb EW: Pathways leading to glioblastoma multiforme: a molecular analysis of genetic alterations in 65 astrocytic tumors. *J Neurosurg* 81: 427-436, 1994.

Lantos PL, VandenBerg SR, Kleihues P: Tumours of the Nervous System. Graham DI, Lantos PL, (eds), Greenfield's Neuropathology. 9, 6th edition, Arnold, London, 1996.

Leach FS, Tokino T, Meltzer P, Burrell M, Oliner JD, Smith S, Hill DE, Sidransky D, Kinzler KW, Vogelstein B: p53 Mutation and MDM2 amplification in human soft tissue sarcomas. *Cancer Res* 53: 2231-2234, 1993.

Leong AS-Y, Milios J, Duncis CG: Antigen preservation in microwave-irradiated tissues: a comparison with formaldehyde fixation. *J Pathol* 156: 275–282, 1988.

Leong AS-Y, Gilham PN: The effects of progressive formaldehyde fixation on the preservation of tissue antigens. *Pathology* 21: 266–268, 1989.

Lesley J, Howes N, Perschl A, and Hyman R: Hyaluronan binding function of CD44 is transiently activated on T cells during an in vivo immune response. *J Exp Med* 180: 383-387, 1994.

Liem RKH, Yen S, Salomon GD, Shelanski ML: Intermediate filaments in nervous tissues. *J Cell Biol* 79: 637-645, 1978.

Lopez F, Belloc F, Lacombe F, Dumain P, Reiffers J, Bernard P, Boisseau MR: The labelling of proliferating cells by Ki67 and MIB-1 antibodies depends on the binding of a nuclear protein to the DNA. *Exp Cell Res* 210: 145-153, 1994.

Louis DN, Seizinger BR: Genetic basis of neurological tumours. *Baillieres Clin Neurol* 3: 335-352, 1994.

Mackay CR, Terpe HJ, Stauder R, Marston WL, Stark H, Gunthert U: Expression and modulation of CD44 variant isoforms in humans. *J Cell Biol* 124: 71-82, 1994.

Mao Y, Desmeules M, Semenciw RM, Hill G, Gaudette L, Wigle DT: Increasing brain cancer rates in Canada. *Can Med Assoc J* 145: 1583-1591, 1991.

Mineta T, Rabkin SD, Yazaki T: Attenuated multi-mutated HSV-1 for the treatment of malignant gliomas. *Nature Med* 1995; 1:938-943.

Mishima Y, Honda C, Ichihashi M, Obara H, Hiratsuka J, Fukuda H, Karashima T, Kobayashi K, Kanda K, Yoshino K: Treatment of malignant melanoma by single neutron capture treatgment with melanoma-seeking ^{10}B compound. *Lancet* 11: 388-389, 1989.

Mishima Y: Selective thermal neutron capture therapy of cancer cells using their specific metabolic activities-melanoma as prototype. In Mishima Y (ed): Cancer Neutron Capture Therapy. New York, Plenum Press: 1-26, 1996.

Miyake K, Underhill CB, Lesley J, Kincade PW: Hyaluronate can function as a cell adhesion molecule and CD44 participates in hyaluronate recognition. *J Exp Med* 172: 69-75, 1990.

Nomizu M, Otaka A, Utani A, Roller PP, Yamada Y: Assembly of synthetic laminin peptides into a triple-stranded coiled-coil structure. *J Biol Chem* 269: 30386-30392, 1994.

Northcliffe LC, Schilling RF: Range and stopping-power tables for heavy ions. *Nucl Data Tables A* 7: 233-463, 1970.

Oliner JD, Kinzler KW, Meltzer PS, George DL, Vogelstein B: Amplification of a gene encoding a p53-associated protein in human sarcomas. *Nature* 358: 80-83, 1992.

Otersen B, Haritz D, Grochulla F, Bergmann M, Sierralta W, Gabel D: Binding and immunohistochemical localization of $Na_2B_{12}H_{11}SH$ to tumor tissue of glioma patients in boron neutron capture therapy. In: Mishima Y (ed) Cancer Neutron Capture Therapy, Plenum Press, New York: 627-632, 1996.

Otersen B, Haritz D, Grochulla F, Bergmann M, Sierralta W, Gabel D: Binding and distribution of $Na_2B_{12}H_{11}SH$ on cellular and subcellular level in tumor tissue of glioma patients in boron neutron capture therapy. *J Neuro-Oncol* 33: 131-139, 1997.

Perutelli, P. and Mori P.G. Interaction of the von Willebrand factor with platelets and thrombosis. Recenti. Prog. Med. 88: 526-529, 1997.

Plate KH, Breier G, Weich HA: Vascular endothelial growth factor and glioma angiogenesis. *Int J Cancer* 59: 520-529, 1994.

Posner JB. Section VI: neoplastic disorders. In: Scientific American Medicine, section 11, neurology. New York, Scientific American, 1995.

Puchtler H, Meloan SN: On the chemistry of formaldehyde fixation and its effects on immunohistochemical reactions. *Histochemistry* 82: 201-204, 1985.

Radhakrishnan K, Bohnen NI, Kurland LT. Epidemiology of brain tumors. In: Morantz RA, Walsh JW (eds) Brain tumors. New York, Dekker, 1-19, 1994.

Ransom DT, Ritland SR, Moertel CA, Dahl RJ, O'Fallon JR, Scheithauer BW, Kimmel DW, Kelly PJ, Olopade OI, Diaz MO: Correlation of cytogenetic analysis and loss of heterozygosity studies in human diffuse astrocytomas and mixed oligo-astrocytomas. *Genes Chromosomes Cancer* 5: 357-74,1992.

Rasheed BK, Fuller GN, Friedman AH, et al. Loss of heterozygosity for 10q loci in human gliomas. *Genes Chromosom Cancer* 5: 75-82, 1992.

Rasmussen S, Bock E, Warecka K, Althage G: Quantification of glial fibrillary acidic protein in human brain tumors. *Br J Cancer* 41: 113-116, 1980.

Reynolds FH Jr., Todaro GJ, Fryling C, Stephenson JR: Human transforming growth factors induce tyrosine phosphorylation of EGF receptors. *Nature* 292: 259-262, 1981.

Rosenberg SA, Lotze MT, Muul LM, Chang AE, Avis FP, Leitman S, Linehan WM, Robertson CN, Lee RE, Rubin J: A progress report on the treatment of 157 patients with advanced cancer with interleukin-2. *N Engl J Med* 316:889-897, 1987.

Salcman M: Survival in glioblastoma: historical perspective. *Neurosurgery* 1980; 7: 435-439.

Saxena A, Clark WC, Robertson JT, Ikejiri B, Oldfield EH, Ali IU: Evidence for the involvement of a potential second tumor suppressor gene on chromosome 17 distinct from p53 in malignant astrocytomas. *Cancer Res* 52: 6716-6721, 1992.

Schluter C, Duchrow M, Wohlenberg C, Becker MH, Key G, Flad HD, Gerdes J: The cell proliferation-associated antigen of antibody Ki-67: a very large, ubiquitous nuclear protein with numerous repeated elements, representing a new kind of cell cycle-maintaining proteins. *J Cell Biol* 123: 513-522, 1993.

Shi SR, Key ME, Kalra KL: Antigen retrieval in formalin-fixed, paraffin-embedded tissues: an enhancement method for immunohistochemical staining based on microwave oven heating of tissue sections. *J Histochem Cytochem* 39: 741-748, 1991.

Shi SR, Imam A, Young L, Cote RJ, Taylor CR: Antigen retrieval immunohistochemistry under the influence of pH using monoclonal antibodies. *J Histochem Cytochem* 43: 193–201, 1995.

Shimizu Y, van Seventer GA, Siraganian R, Wahl L, Shaw S:. Dual role of the CD44 molecule in T cell adhesion and activation. *J Immunol* 143: 2457-2463, 1989.

Starborg M, Gell K, Brundell E, Hoog C: The murine Ki-67 cell proliferation antigen accumulates in the nucleolar and heterochromatic regions of interphase cells and at the periphery of the mitotic chromosomes in a process essential for cell cycle progression. *J Cell Sci* 109: 143-153, 1996.

Steck PA, Bruner JM, Pershouse MA, et al.: Molecular, genetic, and biologic aspects of primary brain tumors. *Cancer Bull* 45: 296-303, 1993.

Stevens JK, Mills LR, Trogadis JE: Three-Dimensional Confocal Microscopy: Volume Investigation of Biological Systems. Academic Press, London, 1994.

Sy MS, Guo YJ, Stamenkovic I: Distinct effects of two CD44 isoforms on tumor growth in vivo. *J Exp Med* 174: 859-866, 1991.

Taylor CR, Burns J: The demonstration of plasma cells and other immunoglobulin containing cells in formalin-fixed, paraffin-embedded tissues using peroxidase labelled antibody. *J Clin Pathol* 27: 14-20, 1974.

Taylor CR: Immunohistologic studies of lymphomas: new methodology yields new information and poses new problems. *J Histochem Cytochem* 27: 1189-1191, 1979.

Taylor CR: Immunohistologic studies of lymphoma: past, present and future. *J Histochem Cytochem* 28: 777-787, 1980.

Taylor CR: The current role of immunohistochemistry in diagnostic pathology. *Adv Pathol Lab Med* 7: 59-105, 1994.

Taylor HJ, Goldhaber M: Detection of nuclear disintegration in a photographic emulsion. *Nature* 135, 341, 1935.

Ushiro H and Cohen S: Identification of phosphotyrosine as a product of epidermal growth factor-activated protein kinase in A-431 cell membranes. *J Biol Chem* 255: 8363-8365, 1980.

Valk PE, Budinger TF, Levin VA, Silver P, Gutin PH, Doyle WK: PET of malignant cerebral tumors after brachytherapy. *J Neurosurg* 69: 830-838, 1988.

Van Meir EG, Roemer K, Diserens AC, Kikuchi T, Rempel SA, Haas M, Huang HJ, Friedmann T, de Tribolet N, Cavenee WK: Single cell monitoring of growth arrest and morphological changes induced by transfer of wild-type p53 alleles to glioblastoma cells. *Proc Natl Acad Sci* 92: 1008-1012, 1995.

Vertosick FT, Selker RG: Brain stem and spinal metastases of supratentorial glioblastoma multiforme: a clinical series. *Neurosurgery* 27: 516-522, 1990.

von Deimling A, Eibl RH, Ohgaki H, Louis DN, von Ammon K, Petersen I, Kleihues P, Chung RY, Wiestler OD, Seizinger BR: p53 mutations are associated with 17p allelic loss in grade II and grade III astrocytoma. *Cancer Res* 52: 2987-2990, 1992a.

von Deimling A, von Ammon K, Schoenfeld D, Wiestler OD, Seizinger BR, Louis DN: Subsets of glioblastoma multiforme defined by molecular genetic analysis. *Brain Pathol* 3: 19-26, 1993.

Watanabe K, Tachibana O, Sata K, Yonekawa Y, Kleihues P, Ohgaki H: Overexpression of the EGF receptor and p53 mutations are mutually exclusive in the evolution of primary and secondary glioblastomas. *Brain Pathol* 6: 217-224, 1996.

Westermark B, Nister M: Molecular genetics of human glioma. *Curr Opin Oncol* 7: 220-225,1995.

Wewer UM, Liotta LA, Jaye M, Ricca GA, Drohan WN: Altered levels of laminin receptor mRNA in various human carcinoma cells that have different abilities to bind laminin. *Proc Natl Acad Sci USA* 83: 7137-7141, 1986.

Wewer UM, Wayner EA, Hoffstrom BG, Lan F, Meyer-Nielsen B, Engvall E, Albrechtsen R: Selective assembly of laminin variants by human carcinoma cells. *Lab Invest* 71: 719-730, 1994.

Wu JK, Ye Z, Darras BT: Frequency of p53 tumor suppressor gene mutations in human primary brain tumors. *Neurosurgery* 33: 824-830, 1993.

Yu Q, Toole BP, Stamenkovic I: Introduction of apoptosis of metastatic mammary carcinoma cells *in vivo* by disruption of tumor cell surface CD44 function. *J Exp Med* 186:1985-1996, 1997.

Zulch KJ: Brain Tumors. Their biology and pathology. 3rd edition, Springer Verlag: Berlin Heidelberg, 1986.

7 APPENDICES

A: A simple method for reduction of auto-fluorescence in fluorescence microscopy

Submitted for publication to the
Journal of Histochemistry and Cytochemistry

A simple method for reduction of autofluorescence in fluorescence microscopy

Michael Neumann and Detlef Gabel

Department of Chemistry, University of Bremen,
Leobener Straße, P. O. Box 330 440, D-28334 Bremen, Germany
Tel.: +49 (0)421 2182200
Fax: +49 (0)421 2182871
gabel@chemie.uni-bremen.de

ABSTRACT:

Autofluorescence of aldehyde-fixed neural tissue often complicate the use of fluorescence microscopy. Background fluorescence can be notably reduced or eliminated by irradiation with light before treatment with fluorescence probes resulting in a higher contrast without adversely affecting the staining probabilities.

KEYWORDS: Autofluorescence, photo bleaching, immunofluorescence

INTRODUCTION:

There are many causes for the autofluorescence of tissue. Some exist only in mammalian tissue like the fluorescent pigment lipofuscin, which accumulates with age in the cytoplasm of cells of the central nervous system. Others are special for plants or are independent of the species and find their origin in the embedding material.

All these causes of autofluorescence have one thing in common: They complicate the use of fluorescence microscopy. In the literature many techniques are described for reducing auto-fluorescence: $CuSO_4$ in ammonium acetate buffer or Sudan Black B in 70 % ethanol (Schnell et al. 1999), $NaBH_4$ (Clancy and Cauller 1998), Pontamine Sky Blue (Cowen et al.

1985) or mathematical models which try to subtract the background fluorescence because of the broader autofluorescent excitation spectra compared to the spectra of the fluorescent label (Van de Lest et al. 1995; Steinkamp and Stewart 1986).

But all these techniques have their disadvantages: The treatment with chemicals reduces also the intensity of immunofluorescent labeling which demands a compromise of autofluorescence reduction and antigen visualization. The mathematical models such as the differential fluorescence correction are difficult and carry the risk of false results.

We have developed a simple method, which eliminates most kinds of autofluorescence in mammalian tissue without adversely affecting the probability of labeling the tissue with fluorescent markers. We found that the irradiation with light eliminates all autofluorescence by photobleaching in tissue sections independent of the kind of tissue.

MATERIALS AND METHODS:

Human brain tumor tissue of different patients and murine liver tissue were fixed in paraformaldehyde and embedded in paraffin. From these, thin sections (5 µm) were cut, mounted on glass slides and centered in a box with up to four fluorescent tubes: One conventional neon tube (18 W), one UV-tube (20 W) and two tubes from Dennerle, Germany (Trocal 5085 and Trocal-Kombi 8085, 18 W each) which have higher emission peaks at 488 nm and 633 nm respectively. By choice of the length of the tubes the maximum amount of slides, which could be irradiated simultaneously, can be varied (in this case 18). For maximum yield of light the box was lined with aluminum foil. The sections were irradiated for 12 to 48 h with each tube depending on the thickness and intensity of the autofluorescence. Some heat sensible antigens may require cooling while being irradiated especially when more than two tubes were used simultaneously. After irradiation the paraffin of the thin sections were removed in xylene for two times 10 min and mounted in Entellan (Merck, Germany). For comparison neighboring sections of each treated tissue section were deparaffinized and mounted without irradiation. For testing the influence of the treatment on the ability of fluorescence markers to label cell structures, samples with and without irradiation were labeled either with ethidium bromide and acridine orange or indirect immunofluorescence. For the latter primary antibodies against glial fibrillary acidic protein (anti-GFAP, Z0334, DAKO, Denmark; prediluted) (20 h incubation at room temperature) were used. The secondary antibody was FITC-conjugated anti-mouse from rabbit (Jackson Immunoresearch, USA; 1:150 for 20 h). For cooling several small plastic containers filled with frozen water were placed inside the irradiation box. In regular time intervals the containers were replaced by recently frozen ones.

For image acquisition a confocal scanning laser microscope (LSM 410 invert, Zeiss) were used. The setting for contrast, brightness, scanning time and pinhole were identical for each picture in each individual set. Fluorescence emission was recorded through a Plan-Neofluar x 40, NA 1,3 oil objective.

All measurements were made with the following filter sets: chromatic beamsplitter FT510, bandpassfilter BP 515-565 for argon laser irradiation at 488 nm and FT 560 long pass filter LP 570 for helium neon laser irradiation at 543 nm.

RESULTS:

During irradiation the autofluorescence reduces dramatically with time. Most of the structures lose their ability for fluorescence after 24 h of treatment. Some structures are less affected by the photo bleaching and were still visible after 48 h of irradiation (Fig. 1).

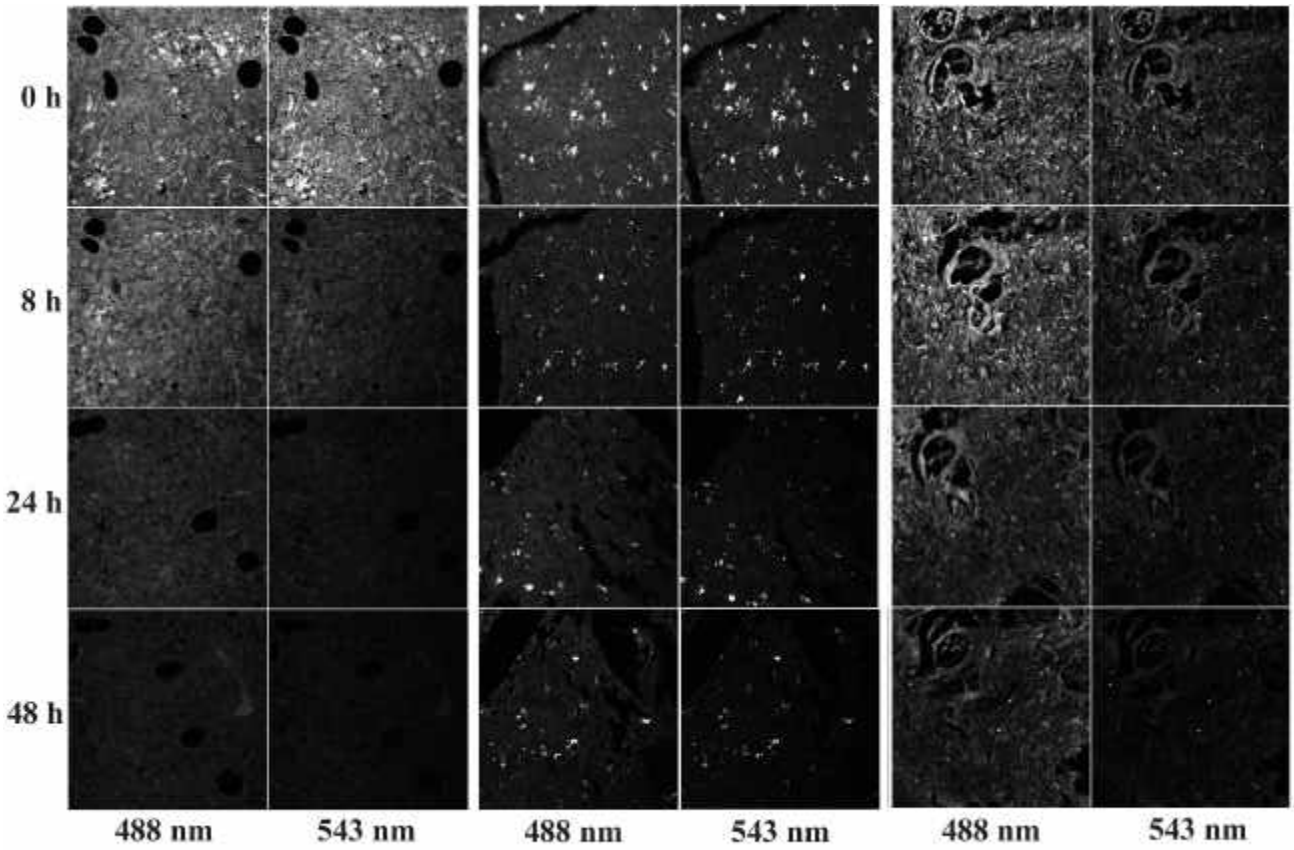

Fig. 1: Photographs of irradiated and non-irradiated tissue sections. Left: mouse liver; middle and right: human brain tumor tissue. Excitation was either at 488 nm or at 543 nm as indicated.

After a longer period of irradiation without cooling the quality of staining for DNA by ethidium bromide and acridine orange was very poor. With cooling during the photo treatment no difference of the staining quality between treated and untreated sections could be detected (Fig. 2).

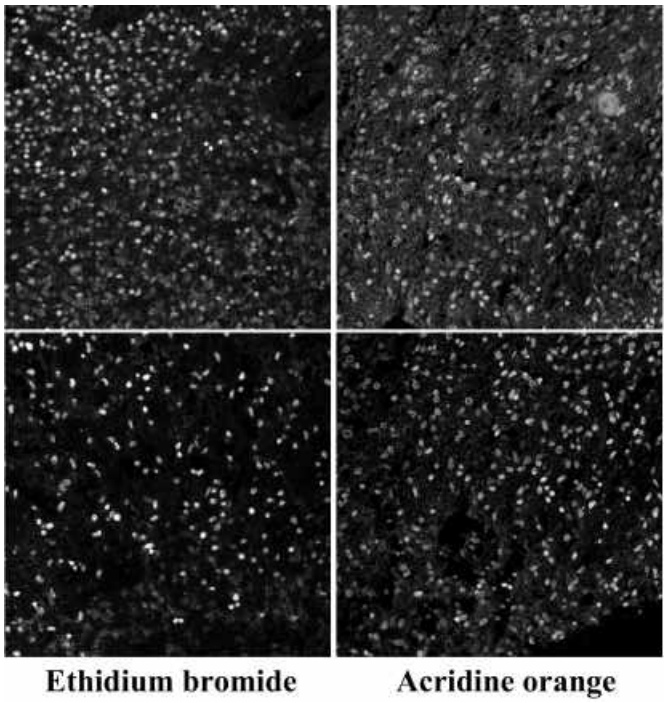

Fig. 2: Staining of the cell nuclei by ethidium bromide and acridine orange in human brain tumor tissue. Top: without irradiation, bottom: 48 h irradiation.

The same results were obtained for immunohistochemistry. With cooling no decrease in the staining quality could be detected (Fig. 3).

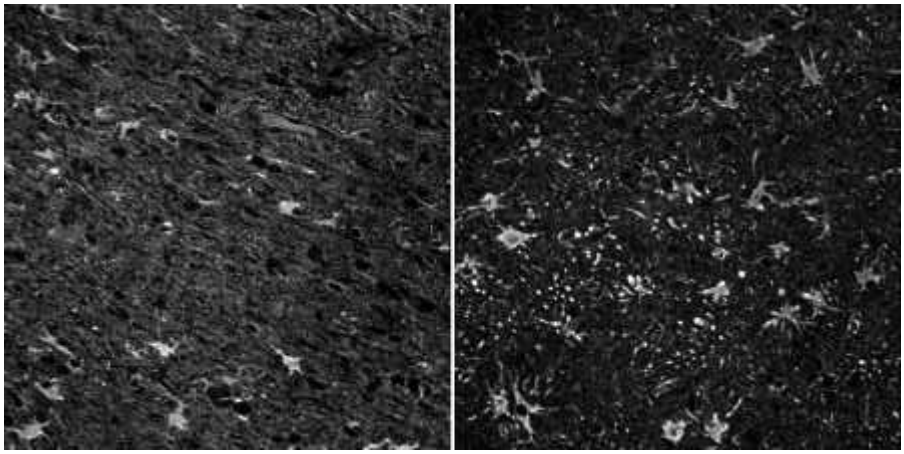

Fig. 3: Staining of GFAP with FITC in human brain tumor tissue. Left: Without irradiation, right: 24 h of irradiation. The contrast improved without decreasing the labeling quality.

DISCUSSION:

By illumination with visible or long-wavelength UV light elimination of nearly all autofluorescence is possible without adversely affecting the probability of labeling the tissue with fluorescent markers, thus improving the quality of staining. Especially in thick sections (> 10 µm) the contrast can be increased dramatically. By using fluorescent tubes with a limited window for the emitted wavelength a chosen range of wavelength could be freed of autofluorescence while another stays in the original state. This could be of interest when the fluorescent structures give additional information. By use of more than one tube for a special wavelength the irradiation time can be decreased.

LITERATURE CITED:

Clancy B, Cauller LJ (1998) Reduction of background autofluorescence in brain sections following immersion in sodium borohydride. *J Neurosci Methods* 83: 97-102

Cowen T, Haven AJ, Burnstock G (1985) Pontamine Sky Blue: a counterstain for background autofluorescence in fluorescence and immunofluorescence histochemistry. *Histochemistry* 82: 205-208

Schnell SA, Staines WA, Wessendorf MW (1999) Reduction of lipofuscin-like autofluorescence in fluorescently labeled tissue. *J Histochem Cytochem* 47: 719-30

Steinkamp JA, Stewart CC (1986) Dual-laser, differential fluorescence correction method for reducing cellular background autofluorescence. *Cytometry* 7: 566-74

Van de Lest CH, Versteeg EM, Veerkamp JH, Van Kuppevelt TH (1995) Elimination of autofluorescence in immunofluorescence microscopy with digital image processing. *J Histochem Cytochem* 43: 727-30

B: Cell type selective accumulation of Mercaptoundeca-hydro-*closo*-dodecaborate (BSH) in glioblastoma multiforme

Submitted for publication to the Journal of Neuro-Oncology

Cell type selective accumulation of Mercaptoundecahydro-*closo*-dodecaborate (BSH) in glioblastoma multiforme

Michael Neumann[1], Markus Bergmann[2] and Detlef Gabel[1]

[1]Department of Chemistry, University of Bremen, Germany
Leobener Straße, P. O. Box 330 440, D-28334 Bremen
Tel.: +49 (0)421 2182200
Fax: +49 (0)421 2182871
gabel@chemie.uni-bremen.de

[2]Institut für Klinische Neuropathologie, Zentralkrankenhaus Bremen Ost, Germany

ABSTRACT:

The cell type specific distribution of mercaptoundecahydro-*closo*-dodecaborate (BSH) in glioblastoma multiforme tissue sections of seven patients having received BSH prior to surgery was investigated by light and fluorescence microscopy. With use of specific antibodies against different tumor specific epitopes and BSH, BSH could be found predominantly (approx. 90 %) in the cytoplasm of GFAP-positive cells of all but two patients. The latter were significantly younger (33 and 38 years versus to 46-71 (mean 60) years). There was no correlation between BSH uptake and expression of EGFR, p53, CD44 and Ki-67.

KEYWORDS:

Immunohistochemistry, Fluorescence microscopy, primary/secondary glioblastoma, BSH

INTRODUCTION:

Boron neutron capture therapy (BNCT) is a radiation therapy to destroy tumor cells while minimizing damage to healthy tissue. It is based on the nuclear reaction that occurs when boron-10 is irradiated with low-energy neutrons. The ^{10}B-nucleus undergoes a neutron capture reaction and disintegrates into two fission particles ($^{10}B(n,\alpha)^{7}Li$) (Taylor et al., 1935) with a range of approximately one cell diameter (Northcliffe and Schilling, 1970). When these particles hit cell nuclei they can cause severe damage which lead to cell death.

For successful treatment, accumulation of boron in tumor to a larger extent than in the surrounding tissue is necessary. Two boron compounds, BSH ($Na_2B_{12}H_{11}SH$) and L-4-dihydroxyborylphenylalanine (BPA), are currently being used clinically as capture agents for glioblastoma multiforme and melanomas (Hawthorne 1998). The localization of boron-10 on a subcellular level has a great influence on the biological effectiveness of BNCT (Kobayashi and Kanda, 1982; Gabel et al., 1987).

BSH has been established as a suitable boron carrier and has been used by Hatanaka et al. since 1968 with encouraging results (Hatanaka and Nakagawa, 1994). Despite of the long use of BSH in BNCT little is known about its distribution within the tumor tissue. Investigation of heterogeneous uptake in relation to structural or functional differences of the tissue plays an important role for understanding the uptake mechanism. With this information structural optimization of the boron carrier could be achieved for higher tumor selective uptake.

It is known that BSH is inhomogeneously distributed in the tumor tissue (Otersen et al., 1996; Otersen et al., 1997; Haritz et al., 1992). Haritz et al. (1992) found, that heterogeneous staining of tumor tissue depends to the density of tumor cells in tissue whereas necrotic areas show a very low uptake of BSH. On the other hand, Otersen et al. (1997) found that the BSH content was independent of cell density. Despite these differences no preferred cell type for BSH accumulation is known. By immunohistochemistry we investigated the question whether BSH accumulates arbitrarily in cells of any kind or whether BSH is preferentially taken up by specific cell types.

MATERIALS AND METHODS:

Origin of tumor material:

Tumor material was collected in a pharmacokinetic study aimed at identifying optimal time point and dosage of BSH. Tissue samples were taken from glioma patients (grade IV, glioblastoma multiforme) who had received BSH prior to surgery in the Zentralkrankenhaus St. Jürgenstraße (Bremen, Germany). Intravenous infusions (40 - 102 mg BSH/kg body weight) were carried out for one hour, 14 to 22 hours before operation (Haritz et al., 1994). After surgery, the material was frozen rapidly and stored at -18 °C.

Patient identification	Age	Administered amount of ^{10}B/ kg body weight	Time between infusion and tumor sampling	Average boron concentration in tumor at surgery
HO	71	31.3 mg	14 h	84.2 ppm
WB	66	54.0 mg	24 h	16.7 ppm
GO	59	21.1 mg	72 h	0.5 ppm
FJ	56	55.9 mg	17 h	39.0 ppm
WF	46	31.3 mg	24 h	16.4 ppm
BE	38	27.9 mg	47 h	8.7 ppm
JU	33	28.1 mg	22 h	12.2 ppm

Table 1: Data of the patients from whom the tumor material was taken.

Tissue preparation:

Fixation was carried out in 10 % buffered formalin for 16 h at room temperature (rt). Previously it had been shown that this treatment does not remove boron from this tissue (Otersen et al., 1996). The tissue was dehydrated in increasing concentrations of ethanol. Afterward, the material was incubated in toluene and embedded in paraffin. Thin section (5 µm) were cut and mounted on glass slides.

Antibody preparation:

At the Institut für Tierzucht und Tierverhalten, Mariensee, Germany a goat was immunized with BSH, which was linked through sulfhydryl groups to bovine serum albumin (BSA). The resulting serum was freed from antibodies directed against BSA by affinity chromatography over a column of BSA bound to sepharose.

Immunohistochemistry

For fluorescence and light microscopy immunohistochemical analysis of formalin-fixed paraffin-embedded human glioma tissue with the polyclonal antibody against BSH was performed on 5-µm-thick sections that were deparaffinized in xylene and rehydrated in sequential baths of ethanol (100 %, 96 %, 90 % and 70 %) and bidistilled water. After blocking with normal rabbit serum the slides were incubated with antibodies against BSH with a dilution of 1:120 for 20 h at rt. followed by exposure of biotinylated rabbit anti-goat secondary antibody (DAKO, Denmark; dilution 1:200) for 30 min at rt. Then the slides were incubated with alkaline phosphatase-avidin-biotin-complex (Camon, Germany; performed as recommended on the data sheet) for 40 min at rt. Between all steps washing with PBS-Tris-buffer pH 7.4 occurred (3 times 10 min each). Finally the sections were developed with Vector Red (Vector laboratories, USA) for 30 - 40 min at rt. As counterstainings similar staining procedures for different antigens, which are exclusively or stronger expressed in tumors, such as MIB 1 (Dianova, Germany; prediluted), CD44 (Dako, Denmark; dilution 1:100), epidermal growth factor receptor (EGFR) (Sigma, USA; dilution 1:120), p53 (BioGenex, USA; dilution 1:200) or glial fibrillary acidic protein (GFAP) (Immunotech, France; dilution 1:30) were used. Incubation with biotinylated (DAKO, Denmark; dilution 1:200) or fluorescein isothiocyanate (FITC)-conjugated (Jackson Immunoresearch, USA; dilution 1:150) rabbit anti-mouse antibody followed. The biotinylated secondary antibody was coupled with a peroxidase-avidin-biotin-complex (Camon, Germany; performed as recommended on the data sheet) for 40 min at rt. Color development was executed with diaminobenzidine complex (Camon, Germany; performed as recommended on the data sheet) for 9 min at rt. For image acquisition a fluorescence microscope (Axiovert 100, Zeiss, Germany) with a digital camera (DMC 1, Polaroid, USA) was used and the fluorescence emission was recorded with following filter sets: Vector Red Excitation: BP510-560 / Emission: LP590, FITC Excitation: BP485/20 / Emission: BP515-565. Evaluation of the obtained images were made by an overlay of the distribution maps of the different stainings in the same section area and counting BSH-positive cells, cells which were stained by the above mentioned antibodies and cells which were stained both for BSH and the used “tumor-selective” markers.

RESULTS AND DISCUSSION:

In tumor sections, a very heterogeneous staining for BSH was observed. In regions of necrosis no BSH could be found. In some cases BSH-containing blood remained in the vessels or in the basement membrane of the blood vessel (Fig. 1). By visual inspection of the slides, no correspondence between the localization of CD44 and Ki-67 on the one hand and BSH on the other hand could be observed. With GFAP, however a high correspondence was found. In all but two tissue blocks almost all BSH-positive cells were also positive for GFAP (Fig. 2).

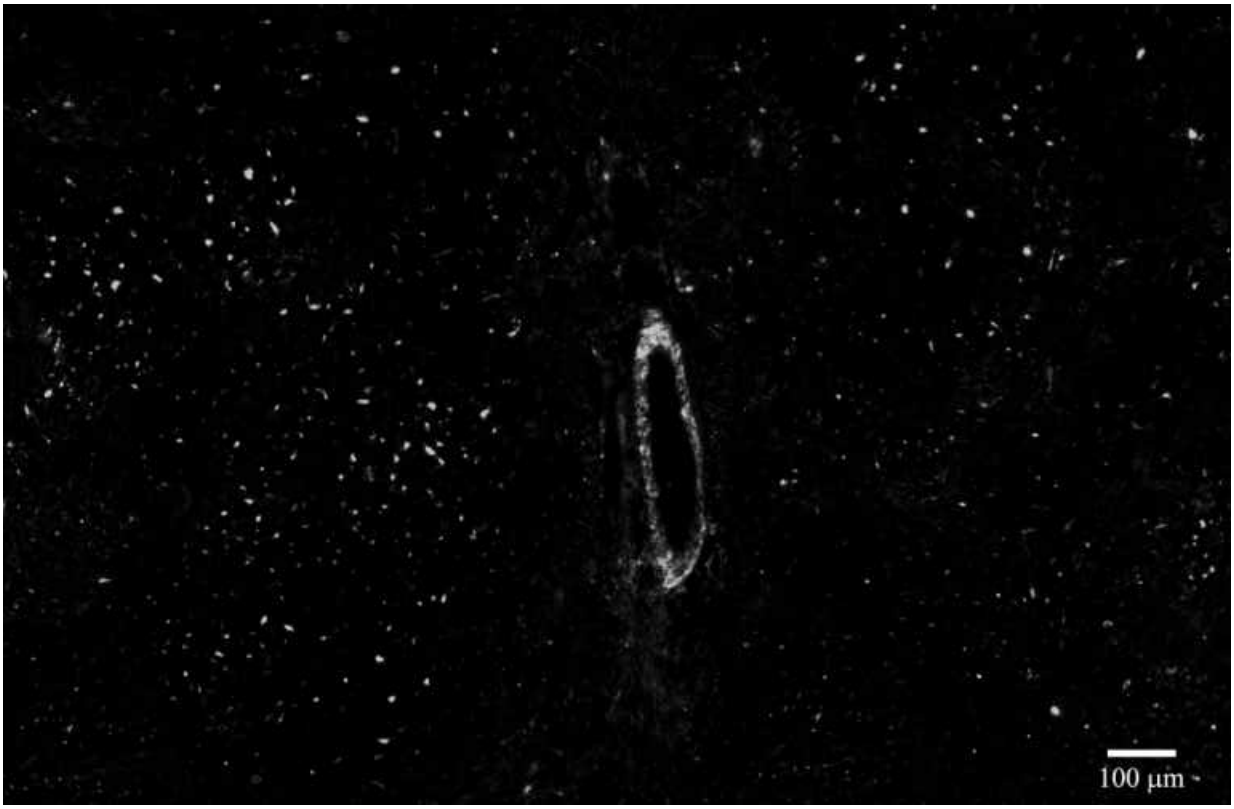

Fig. 1: Patient HO: Immunohistochemical staining for BSH. The basement membrane of a blood vessel in the center is also stained.

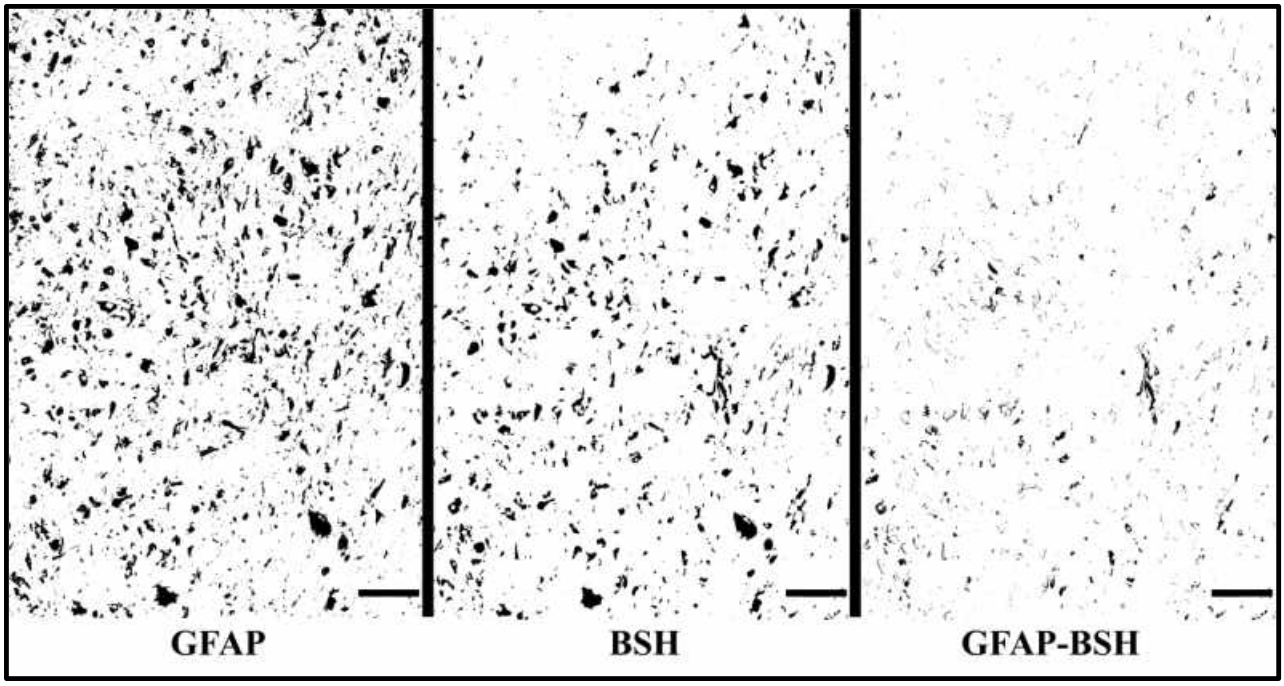

Fig. 2: Photographs of an identical tissue area double stained for GFAP and BSH (patient HO; bar = 100 µm). a) stained for GFAP with DAB, b) stained for BSH with Vector Red (fluorescence, inverted), c) subtraction of b) from a) (inverted). Nearly all BSH-positive cells are also GFAP-positive and appear transparent in the subtracted picture.

Although not all GFAP-positive cells contain BSH (between 14 and 59 % of the GFAP-positive cells contain BSH) (Fig. 3 and Table 2), these appear to be the predominant target for BSH. Several tissue sections of different planes (at least through 50 µm of tumor tissue) of the tumor were prepared and stained for GFAP and BSH. The obtained digital images were overlaid and the BSH-positive, the GFAP-positive and the double positive cells were counted. In five of the seven tumors studied, over 90 % of the BSH-positive cells were also GFAP-positive (Fig. 4) independent of the time between BSH-administration and surgery. HO and GO for example show both a correspondence of BSH- and GFAP-positive cells of about 90 % while the time between BSH-administration and surgery was 14 h and 72 h respectively (Table 2). GFAP stains both tumor cells of glial origin and normal, reactive astrocytes. However, no reactive astrocytes could be found in the tumor tissue sections, with the exception of patients FJ, WF and JU. Only in the tissue sample of JU reactive astrocytes could be detected that were also positive for BSH.

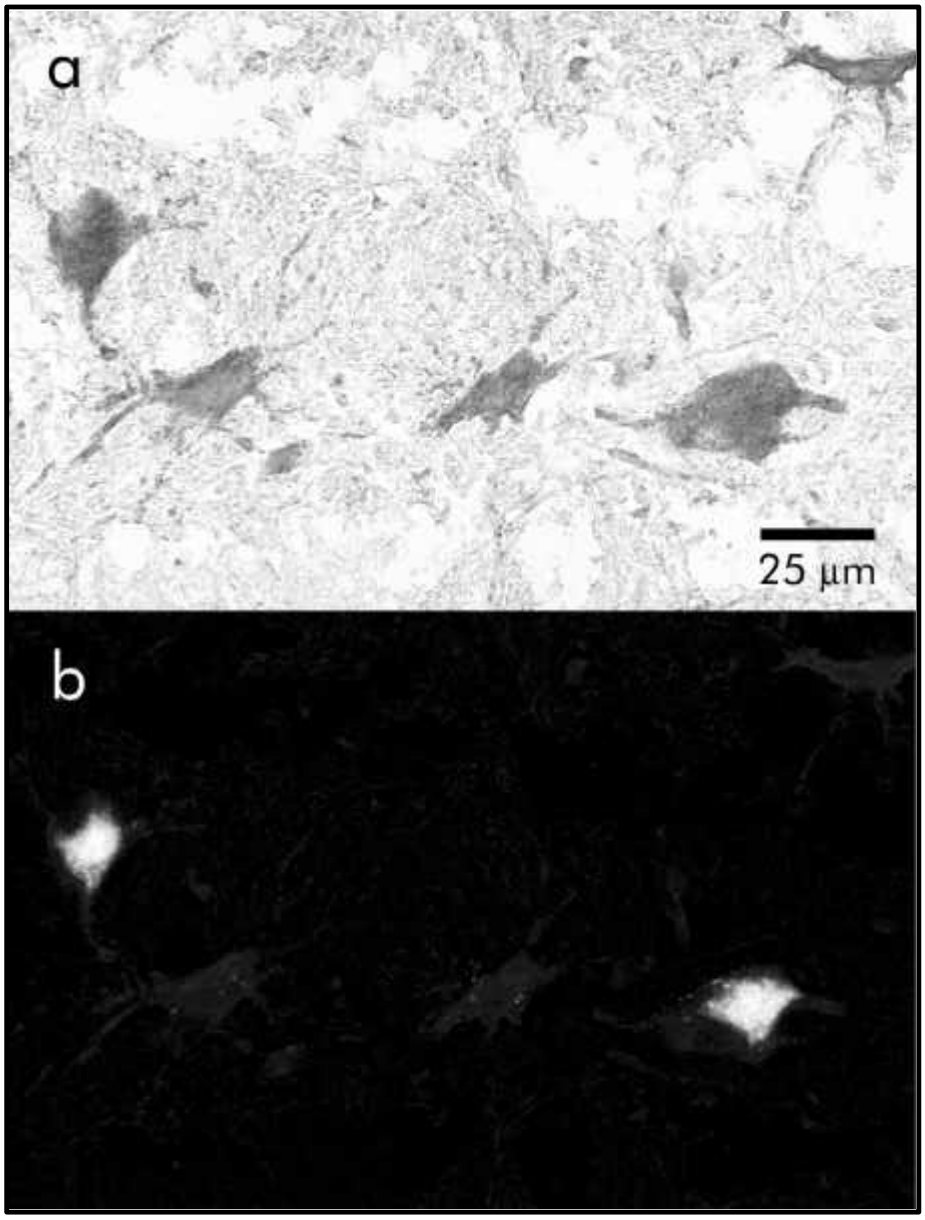

Fig. 3: Patient WF: Double staining of BSH and GFAP: a) cells positively stained for GFAP recorded in light microscopy, b) BSH-staining recorded in fluorescence microscopy. For better comparability GFAP-staining (dark gray) is also shown in b. Not all GFAP-positive cells contain BSH but in all but two patients nearly all BSH was in these cells.

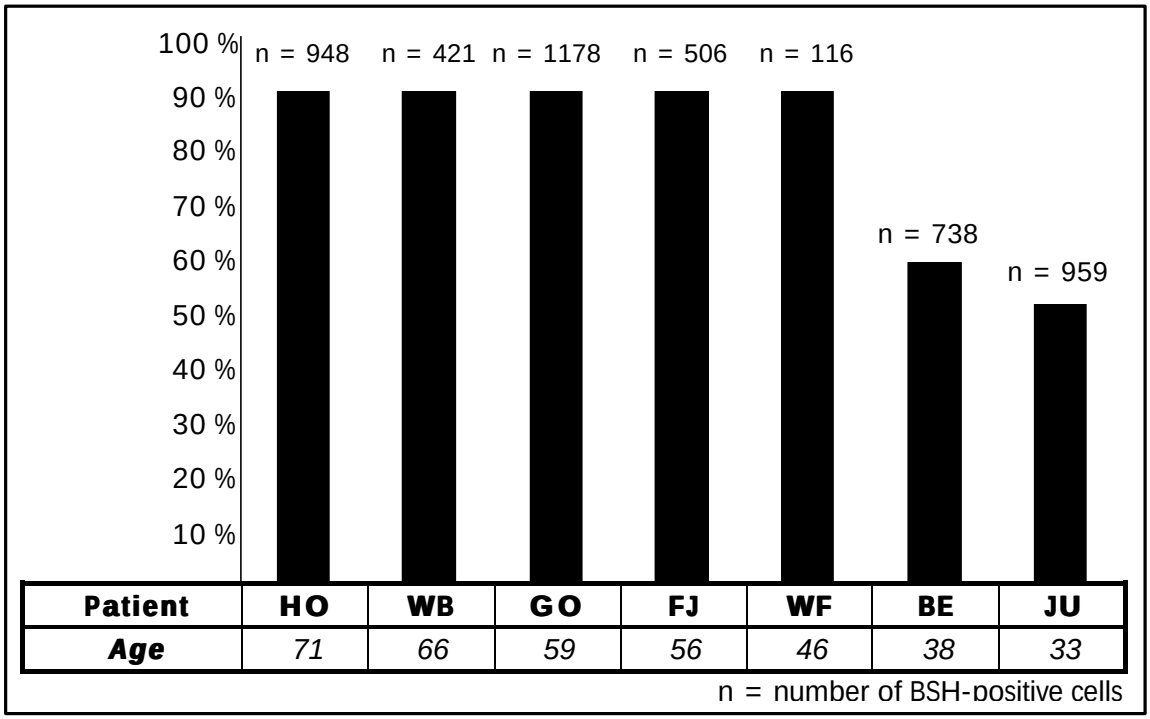

Fig. 4: Correspondence of BSH- and GFAP-positive cells of seven patients in order of decreasing age. The five older patients show a correspondence of over 90 % in contrast to 50-60 % of the two younger patients. No correlation between the distribution of BSH and the time between BSH-infusion and surgery could be found.

The only perceptible difference between the patients JU, BE and the others was that the former was significantly younger (33 and 38 years respectively in contrast of 46 - 71 (mean 60) years). This could be an indication that the tumors in patients JU and BE were secondary glioblastomas, which often develop from low-grade diffuse or anaplastic astrocytomas and typically affect young adults. There is evidence that different genetic pathways lead to glioblastoma as a common phenotypic endpoint (Kleihues and Cavenee, 1997). Two groups of glioblastoma with distinct genetic alterations have been postulated on the basis of the different combinations of p53 tumor suppressor protein mutations and EGFR amplification. According to von Deimling et al. (1993) EGFR amplification occurs significantly more often in elderly patients with primary (*de novo*) glioblastoma. Lang et al. (1994) characterized primary glioblastoma as tumors without p53 mutation but with amplification of EGFR whereas for secondary glioblastoma p53 amplification and lack of EGFR overexpression are characteristic.

Mutations, which occurred during oncogenesis, can possibly influence the uptake of BSH in some cell types. This would lead to a cell type selective accumulation of BSH in the tumor tissue. For further information we used antibodies against EGFR and p53 for determination

of the development of the tumor (Table 2). As reported in the literature, EGFR-overexpression occur in elderly patients whereas p53 overexpression in the younger adults. On the basis of these results the glioblastoma of patient JU seems be of secondary development, whereas for BE and WF no reliable statement could be given. Based on the expression of EGFR and p53, the tumors of the four other patients were from primary development (Table 2). Although the tissue regions of EGFR and p53 overexpression do not seem to correspond with the regions of high BSH incidence, mutations during tumor development could be the reason for the distinct accumulation of BSH. If this is the case, the relevant mutation is still unknown and its finding subject of further investigations.

Patient identification	Age	EGFR	p53	BSH-positive cells which are also positive for GFAP	GFAP-positive cells which are also positive for BSH
HO	71	+ + +	+	90.4 %	39.9 %
WB	66	+ + +	-	90.0 %	21.8 %
GO	59	+ +	-	91.7 %	58.5 %
FJ	56	+	-	90.3 %	37.2 %
WF	46	+	+	92.2 %	14.3 %
BE	38	+	+	60.4 %	39.6 %
JU	33	-	+ + +	52.1 %	40.8 %

Table 2: Comparison of expression of EGFR and p53 with the correspondence of BSH- and GFAP-positive cells. Rating in 4 steps from – to + + + by relation of positive structures/(tissue area).

REFERENCES:

Gabel D, Foster S, Fairchild RG: The Monte Carlo simulations of the biological effect of the $^{10}B(n,\alpha)^{7}Li$ reaction in cells and tissue and its implication for boron neutron capture therapy. Radiat Res 111: 14-25, 1987

Haritz D, Gabel D, Klein H, Huiskamp R, Pettersson O-A: BSH in patients with malignant glioma: Distribution in tissues, comparison between BSH concentration and histology. In: Gabel D, Moss RL (eds.), *Boron Neutron Capture Therapy: Toward clinical trials of Glioma Treatment*. Plenum Press, New York: 163-174, 1992.

Haritz D, Gabel D, Huiskamp R: Clinical phase-I study of $Na_2B_{12}H_{11}SH$ (BSH) in patients with malignant glioma as precondition for boron neutron capture therapy (BNCT). *Int J Radiation Oncology Biol Phys* 28: 1175, 1994.

Hatanaka H, Nakagawa Y: Clinical results of long-surviving brain tumor patients who underwent boron neutron capture therapy. *Int J Radiation Oncology Biol Phys* 28 (5): 1061-1066, 1994.

Hawthorne MF: New horizons for therapy based on the boron neutron capture reaction. *Molecular Medicine Today* 4: 174-181, 1998.

Kleihues P, Cavenee WK: Pathology and Genetics of tumours of the Nervous System. International Agency for Research on Cancer, Lyon: 19, 1997.

Kobayashi T, Kanda K: Analytical calculation of boron-10 dosage in cell nucleus for neutron capture therapy. *Radiat Res* 91: 77-94, 1982.

Lang FF, Miller DC, Pisharodys, Koslow M, Newcomb EW: High frequency of p53 accumulation without p53 gene mutation in human juvenile pilocytic, low grade and anaplastic astrocytomas. *Oncogene* 9: 949-954, 1994.

Northcliffe LC, Schilling RF: Range and stopping-power tables for heavy ions. *Nucl. Data Tables A* 7: 233-463, 1970.

Otersen B, Haritz D, Grochulla F, Bergmann M, Sierralta W, Gabel D: Binding and immunohistochemical localization of $Na_2B_{12}H_{11}SH$ to tumor tissue of glioma patients in boron neutron capture therapy. *Cancer Neutron Capture Therapy*, edited by Mishima, Plenum Press, New York: 627-632, 1996.

Otersen B, Haritz D, Grochulla F, Bergmann M, Sierralta W, Gabel D: Binding and distribution of $Na_2B_{12}H_{11}SH$ on cellular and subcellular level in tumor tissue of glioma patients in boron neutron capture therapy. *J Neuro-Oncol* 33: 131-139, 1997.

Taylor HJ, Goldhaber M: Detection of nuclear disintegration in a photographic emulsion. *Nature* 135, 341, 1935.

von Deimling A, von Ammon K, Schoenfeld D, Wiestler OD, Seizinger BR, Louis DN: Subsets of glioblastoma multiforme defined by molecular genetic analysis. *Brain Pathol* 3: 19-26, 1993.

C: Spectromicroscopy of boron in human glioblastomas following administration of $Na_2B_{12}H_{11}SH$

***Physical Review E* 62: 1110-1118, 2000**

Spectromicroscopy of boron in human glioblastomas following administration of $Na_2B_{12}H_{11}SH$

B. Gilbert,[1,*] L. Perfetti,[1] O. Fauchoux,[1] J. Redondo,[1] P.-A. Baudat,[1] R. Andres,[2] M. Neumann,[3] S. Steen,[3] D. Gabel,[3] Delio Mercanti,[4] M. Teresa Ciotti,[4] P. Perfetti,[5] G. Margaritondo,[1] and Gelsomina De Stasio[5,6]

[1]*Institut de Physique Appliquée, Ecole Polytechnique Fédérale, PH-Ecublens, CH-1015 Lausanne, Switzerland*

[2]*Paul Scherrer Institut, CH-5232 Villigen, PSI, Switzerland*

[3]*Department of Chemistry, University of Bremen, P.O. Box 330 440, D-28334 Bremen, Germany*

[4]*Istituto di Neurobiologia del CNR, Viale Marx 15, 00100 Roma, Italy*

[5]*Istituto di Struttura della Materia del CNR, Via Fosso del Cavaliere, 00137 Roma, Italy*

[6]*Department of Physics, University of Wisconsin-Madison and Synchrotron Radiation Center, 3731 Schneider Drive, Stoughton, Wisconsin 53589*

(Received 8 March 1999; revised manuscript received 23 December 1999)

Boron neutron capture therapy (BNCT) is an experimental, binary treatment for brain cancer which requires as the first step that tumor tissue is targeted with a boron-10 containing compound. Subsequent exposure to a thermal neutron flux results in destructive, short range nuclear reaction within 10 μm of the boron compound. The success of the therapy requires than the BNCT agents be well localized in tumor, rather than healthy tissue. The MEPHISTO spectromicroscope, which performs microchemical analysis by x-ray absorption near edge structure (XANES) spectroscopy from microscopic areas, has been used to study the distribution of trace quantities of boron in human brain cancer tissues surgically removed from patients first administered with the compound $Na_2B_{12}H_{11}SH$ (BSH). The interpretation of XANES spectra is complicated by interference from physiologically present sulfur and phosphorus, which contribute structure in the same energy range as boron. We addressed this problem with the present extensive set of spectra from S, B, and P in relevant compounds. We demonstrate that a linear combination of sulfate, phosphate and BSH XANES can be used to reproduce the spectra acquired on boron-treated human brain tumor tissues. We analyzed human glioblastoma tissue from two patients administered and one not administered with BSH. As well as weak signals attributed to BSH, x-ray absorption spectra acquired from tissue samples detected boron in a reduced chemical state with respect to boron in BSH. This chemical state was characterized by a sharp absorption peak at 188.3 eV. Complementary studies on BSH reference samples were not able to reproduce this chemical state of boron, indicating that it is not an artifact produced during sample preparation or x-ray exposure. These data demonstrate that the chemical state of BSH may be altered by *in vivo* metabolism.

PACS number(s): 87.59.−e

I. INTRODUCTION

Glioblastoma multiforme is the most malignant form of glioma (cancer of the glial cells, which provide the support environment for neurons) and conventional treatments remain incapable of significantly prolonging life expectancy beyond an average of 6–12 months after diagnosis. Radiotherapy after surgery is the only treatment shown to be capable of slowing but not curing the cancer. The significant limitation of radiotherapy or chemotherapy is the lack of specificity towards individual cancer cells, especially when metastasis has occurred. New modalities are sought which target tumor and spare healthy tissue. Glioblastomas appear very heterogeneous, and multiple genetic pathways may lead to the malignant tumor [1] but tumor cells may present different antigens than healthy tissue or amplify certain gene expression. Radioactive isotopes, foreign genes in liposomes or stimulants to the immune system may be conjugated to antiglioma antibodies. Genetic therapies aim to stimulate the expression of foreign toxic genes, or to inhibit the expression of a tumor-specific gene with an antisense gene. In both cases, the exogenous genetic material must penetrate the tumor membrane by, for example, virus mediated delivery.

Boron neutron capture therapy (BNCT), first proposed in 1936 [2], is another experimental therapy that could potentially destroy tumor regions, but spare healthy tissue. The key feature of successful BNCT is the selective accumulation of a ^{10}B-enriched compound in regions of tumor tissue [3]. Neutron capture by ^{10}B leads to fission by the reaction $^{10}B(n,\alpha)^7Li$. ^{10}B has a capture cross section for thermal neutrons (3,838 b) many times greater than other elements present in tissue (^{16}O has 0.00019, ^{12}C has 0.0035, ^{1}H has 0.333, ^{14}N has 1.83 barn). Therefore, if ^{10}B is present in tissue irradiated by a neutron flux, almost all of the radiation dose results from the boron neutron capture reaction. The energetic alpha and ^{7}Li particles that are produced are highly biologically destructive over a short distance around the boron atom. The ^{7}Li particle has a range of about 3 μm, while the α particle has a range of about 10 μm; both distances are smaller than typical brain cell dimensions. Thus if compounds containing ^{10}B can be delivered only to regions of tumor tissue, irradiation of a macroscopic tissue area with a neutron flux will result in the selective destruction of tumor, while neighboring tissue receives a much lower radiation dose.

Following the administration of a boron compound, it is of great importance to assess its subsequent distribution, in the blood stream, areas of healthy tissue and the tumor itself. Using the technique of inductively coupled plasma atomic

*Author to whom correspondence should be addressed.

emission spectroscopy (ICP-AES) to measure volume-averaged boron concentrations, several compounds have demonstrated tumor affinity in animals and humans [4]. One such compound is BSH ($Na_2B_{12}H_{11}SH$), first proposed for BNCT in 1967 [5]. BSH has had some success in the treatment of malignant human gliomas with BNCT in Japan [6] and has been chosen as the compound to be used in European clinical trials [7,8] which were started in 1997. The development of so-called ''third generation'' boron compounds is ongoing, and applies a more systematic methodology common to all antitumor drug design [9] and faces the same challenges, such as the low permeability of the blood-brain barrier.

Because of the short range of the fission products of the boron neutron capture reaction, it is also vital to study the boron distribution in tissue at a microscopic level. A BNCT compound must target all tumor cells to ensure tumor destruction without the possibility of recurrence. Additionally, the location of boron in cells (e.g., cytoplasm or nucleus) has large implications for the efficacy of BNCT treatment. The microdistribution of BSH has been investigated by several techniques [10–12] but no complete description exists of the fate and distribution of BSH *in vivo*. The present study was stimulated by the need to address this important subject for BNCT.

The MEPHISTO (microscope à emission de photoélectrons par illumination synchrotronique de type onduleur) spectromicroscope employs the technique of synchrotron x-ray photoelectron emission spectromicroscopy (X-PEEM), hereafter referred to as spectromicroscopy. MEPHISTO produces magnified images of the area under investigation and performs elemental and chemical state analysis of microareas of the images, while scanning the photon energy. Using tunable soft x rays from a synchrotron source, MEPHISTO acquires x-ray absorption spectra, collecting the electrons emitted at each photon energy from selected areas [13,14]. MEPHISTO micrographs represent the two-dimensional (2D) distribution of the photoelectron emission intensity from the sample surface at a specific photon energy, and provide an image of the area under investigation, on which up to eight spectra can be acquired simultaneously. The field of view of a micrograph can be easily varied between 10 and 500 μm, while the spectra acquisition regions can be chosen to be 0.5–500 μm. The MEPHISTO spectromicroscope has been used for studies in neurobiology, including the detection of trace concentrations of metals in neuron networks, and the analysis of the boron distribution in rat brain tumor tissues [15,16].

We are currently trying to adapt the methods of immunohistochemistry for optical microscopy to spectromicroscopy. The goal is to label tissue structures with a nonphysiological element for imaging in the MEPHISTO spectromicroscope. Specifically, we intend to use the ABC (avidin-biotin-complex) technique [17] with the incorporation of nickel as a staining agent, which is spectroscopically detectable. The results of this effort have not yet been perfected and will be the subject of a further publication. The data presented below were obtained from human glioblastoma samples from patients administered with BSH and stained with nickel in the framework of this effort. Nickel staining does not affect the spectromicroscopy of boron or other physiological elements.

II. MATERIALS AND METHODS

A. XANES spectroscopy of reference boron compounds

X-ray absorption near edge structure (XANES) spectra of all compounds were acquired at the University of Wisconsin-Madison Synchrotron Radiation Center. Certain spectra were acquired from the User's Chamber on the Mark V Grasshopper or 10 m TGM beamlines, by measuring the total photocurrent from a powdered sample mounted on carbon tape. Other spectra were acquired from a sample in MEPHISTO mounted on the 6 m TGM beamline, by measuring the intensity at the phosphor screen (proportional to the total photoelectron yield) of MEPHISTO. A comparison of the energy position of the characteristic sharp peak of tetrahedral boron oxide from spectra taken on these beamlines showed discrepancies of up to 0.6 eV between the beamlines. This was compensated for by rigidly shifting spectra from the Mark V and 10 m TGM beamlines to match those from the 6 m TGM.

All spectra were saved as text files and plotted in KALEIDAGRAPH 3.0.4 for Macintosh. Normalization of the spectra was performed by dividing the experimental data by the beamline transmission curve acquired reading the photocurrent on either a gold diode (in the case of 6 m TGM) or from a piece of bare carbon tape (Mark V, 10 m TGM), which does not contain boron. The beamline transmission curve vs photon energy often contains undesirable structures which affect the spectrum lineshape, and which must be removed.

The boron compounds cesium borocaptate (BSH), cesium dodecahydrododecaborate, decaborane, *ortho*-carborane, sodium tetrahydridoborate, and boronophenylalanine were purchased from Boron Biologicals, Inc., and studied as pure powder without further purification. All other inorganic boron, sulfur and phosphorus compounds were purchased from Alfa Aesar.

Additional reference samples of BSH were prepared by depositing 2 μg BSH in solution onto a silicon substrate and air drying. To investigate the possibility of photochemical reactions induced by x-ray illumination, or other artifacts created during ashing, we also prepared BSH droplet samples in the presence of albumin. This large molecular weight protein has all the physiological elements present in the tissue, and may therefore constitute a source of chemicals necessary for such reactions. These samples were prepared with 2 μg BSH in a matrix of up to 5 μg bovine serum albumin. One BSH sample and the BSH/albumin samples were ashed in a cold oxygen plasma or UV/ozone (as described below for tissue sections) for different periods, up to 48 h.

B. Human tissue samples

The tissue samples from three patients were obtained from the Hospital St. Jürgen Str., Bremen, Germany. They are identified using the patients' initials and the number of the section taken from the tissue block. Two of the patients (FR and JU) requiring brain surgery for the removal of malignant glioblastoma were intravenously injected with BSH 24 h before the operation (patient FR) or 70 and 22 h before (patient JU was administered twice with BSH). The control sample (patient DS) was obtained from a patient who was

not administered any boron compound. The excised tumor tissue was fixed overnight in a 10% solution of formaldehyde. It was dehydrated by immersion in baths containing increasing concentrations of ethanol (70, 96, and 99%, three exposures for 30 min at each concentration) ensuring limited exposure of tissue to ambient air while transferring between baths. The tissue was hardened in toluene for 1 h and finally embedded in paraffin at 60 °C.

Sectioning of the bulk tissue samples in paraffin was performed with microtomy (7 μm thick sections). A few sections were taken from patient JU by ultramicrotomy after embedding the tissue in resin. These sections were between 100 nm and 2 μm thick, and were not stained.

Tumor tissue containing boron was taken from two different patients. From ICP-AES analysis, the boron concentration in the tumor from patient FR was 75 ppm. ICP-AES data for patient JU were not available.

For MEPHISTO analysis, microtomed sections were mounted on silicon wafers. Neighboring tissue sections were mounted on glass microscope slides. Both the glass and silicon surfaces had been treated with ARPES [3-(triethoxysilyl)propylamine] to improve tissue adhesion. When the samples for MEPHISTO analysis were stained, this procedure was carried out simultaneously with the staining of the neighboring sections on glass to provide reference samples for visible light microscopy (VLM) analysis. If the MEPHISTO sample remained unstained then only the neighboring sections on glass were stained to provide reference samples.

The ABC (avidin-biotin-complex) staining method used here is described in detail elsewhere [17,18]. The monoclonal antibodies used for immunohistochemical staining were either anti-Ki-67 (a protein found in the nuclei of proliferating cells, antibody from Dianova, Germany), anti−van Willebrandt factor (located in blood vessel endothelia, antibody from DAKO, Denmark) or anti-BSH (prepared at the University of Bremen).

Following the removal of paraffin with xylene, the tissue sections were rehydrated with increasing concentrations of water in ethanol. In all stained samples, endogenous peroxidase was blocked with 1% H_2O_2 in double distilled water, then the specimens were incubated with normal serum (DAKO, Denmark) in a humid chamber for 1 h at room temperature. All subsequent incubations also took place in a humid chamber at room temperature. After each application of reagents, the sections were washed with 0.005 Tris-HCl buffer Ph=7.4. The samples were then incubated overnight with the monoclonal antibody.

Following the exposure to the primary antibody and washing, all samples were exposed for 30 min to a biotin-conjugated secondary antibody. Several secondary antibodies may bind to the immunoglobulin of each primary antibody. An enzyme (either horseradish peroxidase or alkaline phosphatase) was linked to the secondary antibodies via the formation of avidin-biotin-enzyme complexes in a 30 min incubation. Amplification of the stain occurs during this process, as many enzyme units bind to the secondary antibodies. The stain development process is different for the two enzymes. Oxidative polymerization of diaminobenzidine by horseradish peroxidase and H_2O_2 in the presence of $NiCl_2$ produces a black precipitate. In this way, nickel is incorporated into the stain for subsequent MEPHISTO or VLM analysis. In double stained samples for the VLM, a blue precipitate is obtained from the alkaline phosphatase mediated BCIP/NBT redox reaction.

Tissue samples from patient FR destined for MEPHISTO analysis were ashed with a cold plasma (150 °C, Plasma-Processor 300E, Techn. Plasma GmbH, München) in the presence of oxygen for 24 h. After ashing the tissue thickness is reduced because carbon and nitrogen are removed by oxygen plasma oxidation. More specifically, the atomic oxygen radicals in the plasma react with the carbon present in the tissue to form CO or CO_2, which are then removed by the pumping system. Carbon is a majoritary component of tissue, therefore removing carbon by ashing results in an enhancement of the relative concentration of the other elements (boron in the present case). We previously demonstrated the effectiveness of ashing in this respect, and we showed that no material displacement was detected [19]. The detection limits of MEPHISTO for phosphorus ($2p$) and chromium ($2p$) are on the order of 100 ppm and it is reasonable to assume a similar limit for boron ($1s$) [20]. The measured bulk concentration of boron in the human tissue samples studied is at this level or less, so that boron from BNCT is in principle undetectable by MEPHISTO in unashed tissues, at least if the boron is homogeneously distributed. The tissue samples on silicon from patient FR were ashed with UV light from a low pressure mercury lamp, which generates and dissociates ozone and consequently removes organic carbon by oxidation [21]. The ozone ions are lower in energy than the oxygen plasma, and this further ensures that no redistribution of material occurs during ashing.

The MEPHISTO spectromicroscope [13] uses an electron optics system (SpectroMicroTech, Milwaukee, WI, USA) to form a magnified image of the secondary electrons, originating from inelastic collisions of primary and Auger electrons, emitted by a specimen under soft x-ray illumination. The x-ray beam incident at 60° to the specimen normal, which lies on the electron optical axis. The electron image intensity is amplified by a series of two microchannel plates, and converted into a visible image by a phosphor screen (Galileo, Ca, USA). This image is captured by a video camera (Dage, USA) linked to a Pentium computer for display and data acquisition. The image magnification is continuously variable up to 8000 times, and the optimum lateral resolution has been measured to be 20 nm [22]. The photoelectrons are not energy filtered, so the total photoelectron yield, per unit area per unit time, is recorded as a function of photon energy. Such spectra reflect the x-ray absorption coefficient of the specimen surface and are hence referred to as x-ray absorption spectra. The depth at the specimen portion that is probed by this technique is limited by the secondary electron escape depth, which is less than 100 Å in the B $1s$ photon energy range [23]. The energy position and lineshape of spectral features provide element identification and chemical state information. Spectra can be acquired simultaneously from several regions selected anywhere on the image of the sample surface. For this work, MEPHISTO was mounted on the 10 or 6 m TGM beamlines of the University of Wisconsin-Madison Synchrotron Radiation Center.

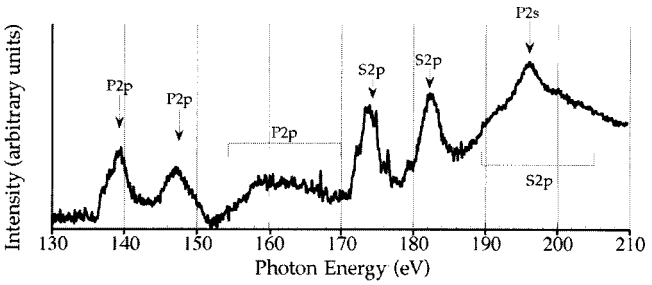

FIG. 1. X-ray absorption spectrum of UV/ozone ashed control tissue (no boron) across the sulfur and phosphorus *L* edges. The contributions from *S* and *P* indicated are typical for ashed tissue. Spectrum acquired in the MEPHISTO chamber on 6 m TGM beamline.

Optical micrographs were obtained using a Zeiss Axiotech 100 HD microscope connected to a Sony 950 DXC color video camera whose output was captured using AVID VIDEOSHOP® software for Macintosh. MEPHISTO and VLM micrographs were manipulated in ADOBE PHOTOSHOP 3.0 for Macintosh. The contrast was slightly enhanced and the scale bar added.

III. RESULTS AND DISCUSSION

A. Principles of boron detection in tissues with x-ray absorption spectroscopy

Figure 1 shows a typical total yield spectrum acquired in the photon energy range 160–210 eV from ashed brain tissue not treated with boron, containing signals from sulfur and phosphorus. The tissue was ashed for 72 h in an ozone/UV-light environment. The spectroscopy of all principal physiological elements following ashing is reported in a separate article [21]. The B 1*s* absorption edge lies in the photon energy range 175–210 eV. There are three important contributions to the absorption spectrum in this region: (1) the strong S 2*p* shape resonance at 182 eV, (2) broader resonances between 187–200 eV also associated with the S 2*p* core level, and (3) the peak of the P 2*s* absorption edge.

1. Sulfur and phosphorus L-edge XANES

The strongly oxidizing environment during the ashing process was expected to convert all the organic sulfur and phosphorus compounds into oxides, and this was confirmed experimentally by comparing the x-ray absorption near-edge structure (XANES) spectra of reference sulfate and phosphate compounds with the spectra from ashed tissues. The results at the sulfur *L* edge are reported in Figs. 2(a) and 2(b). The near-edge region of the sulfur *L* edge has been described as a ''fingerprint'' region because the spectral structure is unique for each chemical environment [24]. Furthermore, as shown elsewhere [19], the ashing of tissues removes all detectable carbon from the probed surface layer. Figure 2 shows the XANES of a range of sulfur-oxygen-metal reference salts. The metals chosen (potassium and sodium [monovalent, Fig. 2(a)] and calcium [divalent, Fig. 2(b)]) are physiologically present in tissue. Figure 2(a) demonstrates that the main factor influencing the line shape is the chemical structure (compare sodium sulfate, sulfite, and thiosulfate) although there are also differences between the spectra from sodium and potassium sulfate. The top spectrum of calcium sulfate in Fig. 2(b) shows extra structure due to higher orders

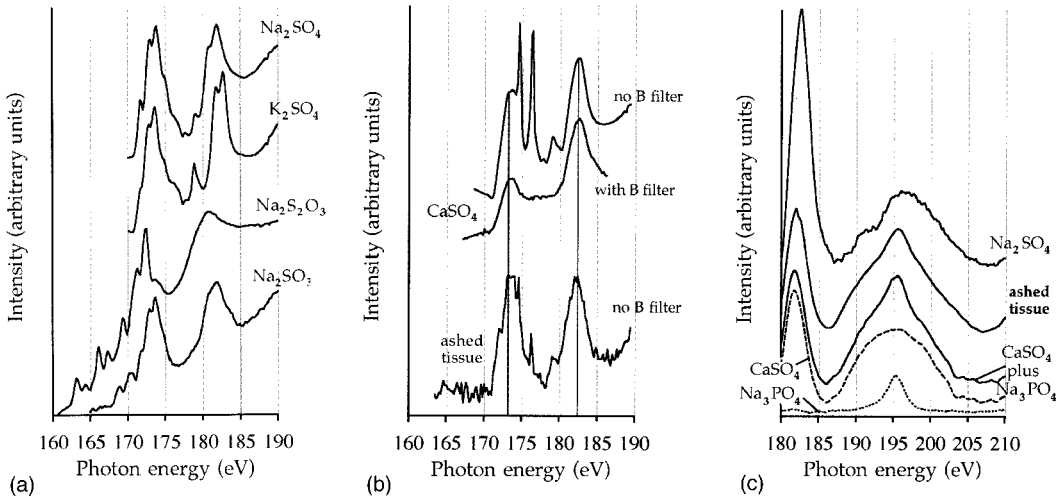

FIG. 2. Sulfur *L*-edge XANES spectra from metal-sulfur-oxygen compounds which may be formed during the ashing of tissues. The near-edge fine structure is unique for each compound and can be compared with the XANES from ashed tissue (b) to determine the products of the oxidation of organic sulfur. (a) The XANES of monovalent metal sulfates (sodium sulfate Na_2SO_4 and potassium sulfate K_2SO_4) and the lesser oxides sodium thoisulfate $Na_2S_2O_3$ and sodium sulfite Na_2SO_3. (b) Sulfur *L* edge XANES of the divalent metal sulfate calcium sulfate $CaSO_4$, acquired with and without a boron filter to remove higher order (higher energy) photons from the monochromator output. The filter removes three spurious spectral components (the sharp doublet around 175 eV is the second order calcium 2*p* signal, the peak at 179 eV is third order O 1*s*). The bottom spectrum is from UV/ozone ashed control tissue (acquired with no filter), and is closest to the top calcium sulfate line shape. Extra structure may be explained by the presence of other sulfates (a) but not the lower sulfur oxides. (c) Sulfur XANES contribute structure in the boron 1*s* energy region (175–210 eV) which is smoother for calcium sulfate than for sodium sulfate (top solid line). The lowest solid curve shows a combination of the calcium sulfate (dashed line) and a sodium phosphate peak (P 2*s*, dotted line) which very well reproduces the spectrum from ashed tissue not containing boron (central solid line). Reference spectra acquired in SRC User's Chamber on 10 m TGM beamline.

of synchrotron light, specifically second order Ca $2p$ peaks (normally at 350 eV) and another signal at 179 eV attributed to third order O $1s$ (normally at 537 eV). By using a thin boron film as a low pass filter (188 eV cutoff) in the x-ray beam, these effects were removed in the lower spectrum. Both of these spectra are presented since the boron filter could not be used when studying real tissue samples. Hence the final spectrum, taken from ashed human brain tissue, also contains these higher order signals.

Comparing the spectra in Figs. 2(a) and (b) we conclude that ashed tissue contains mostly calcium sulfate (the second order $2p$ peaks show that calcium is certainly present). The extra structure on each of the two main peaks indicates that other (potassium or sodium) sulfates are present at lower concentrations. The relative concentrations of these metals do vary throughout normal tissue, and some variation in exact line shape is observed in real samples. Although there is some noise in the tissue spectrum before the first peak, we never observed any structure below 170 eV that matched the lineshapes of the lower sulfur oxides.

The structure of the sulfur *L*-edge continuum resonances within the B $1s$ energy region varies with the local atomic environment of the sulfur atom (i.e., the oxygen coordination of the sulfur atom and the salt stoichiometry). Figure 2(c) compares the ashed tissue line shape with two reference sulfur spectra and one spectrum from a phosphate species. Physiological phosphorus is also oxidized during ashing and the resulting phosphates contribute structure through P $2s$ absorption at 196 eV. Figure 2(c) shows that a linear sum of the calcium sulfate and sodium phosphate spectra (shown individually as the dashed lines) agrees very closely with the spectrum from ashed tissue. By contrast, the spectrum from sodium sulfate (sodium is monovalent) clearly has extra structure around 190 eV as compared to that from calcium sulfate (calcium is divalent). Very little variation was observed in the position and shape of the P $2s$ peak in other phosphates. However, the intensity ratio of sulfur and phosphorus signals can fluctuate significantly across the surface of a tissue section [compare Fig. 2(c) with the same energy region of Fig. 1]. *In vivo*, regions of protein synthesis are richer in sulfur than, for example, the nucleus, which contains nucleic acids, in turn rich in phosphates. In general, however, a linear combination of a sulfate $2p$ signal and a phosphate $2s$ signal is a good model for the absorption spectrum of ashed control tissue in the B $1s$ region (175–210 eV).

These spectra indicate that the interference between sulfur and boron are minimized if the tissue is fully ashed (i.e., physiological sulfur is fully oxidized to sulfate) and if the predominant species is calcium sulfate or the sulfate salt of another divalent metal. The sulfur *L*-edge spectra are then smooth in the B $1s$ energy region.

2. Boron K-edge XANES

We acquired reference spectra from relevant boron compounds to understand the boron absorption spectra acquired from tissues.

Mercaptoundecahydrododecaborate (the sulfhydryl boron hydride, $B_{12}H_{11}$ SH or BSH). BSH has a *closo* icosahedral (12 atom) boron framework covered by *exo* hydrogen atoms, with the exception of the -S-H group substituted for hydrogen. The icosohedral moiety has an overall charge of 2^-, and hence is soluble in water and forms ionic salts (e.g., Cs_2BSH or Na_2BSH). The spectrum of BSH is displayed in Fig. 3.

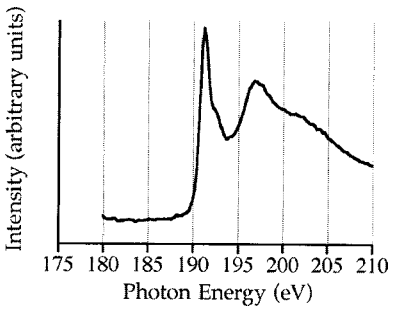

FIG. 3. Boron *K* edge XANES of $B_{12}H_{11}SH$. Spectra acquired in the MEPHISTO chamber on 6 m TGM beamline.

Boron oxides. As the ashing of organic sulfur and phosphorus compounds is expected to form sulfates and phosphates, so the boron in BSH may also be oxidized. Boron naturally forms oxides with a range of stoichiometric formulas, but the most common structural unit contains boron coordinated by oxygen atoms in a planar trigonal environment. This is the case for both the crystalline oxide B_2O_3, and boric acid $B(OH)_3$. The identical *K*-edge XANES spectra of these compounds are displayed together in Fig. 4.

Ashing BSH. To follow the chemical changes produced in BSH present in tissue during ashing, BSH in solution (2 μg) was deposited onto silicon substrates and air dried, either pure or in the presence of 1 μg bovine serum albumin (BSA), and these were ashed for up to 48 h. A cold oxygen plasma oven was used to ash these specimens. The energetic oxygen ions in plasma are expected to oxidize samples more rapidly then the UV/ozone environment (in which the oxygen radicals have thermal kinetic energies) but the chemical endpoint will be the same. When BSH was ashed alone an oxide species was rapidly formed, as shown by the characteristic sharp peak at 194 eV, having a maximum intensity after about 1 h [Fig. 5(a)]. The intensity of the BSH 191.4 eV exciton was also reduced. However, the oxide peak subsequently diminished, as seen in the 48 h spectrum.

When BSH was ashed in a protein matrix, the strength of the boron signal increased with ashing time, as organic carbon was removed [Fig. 5(b)]. In this case the oxide peak

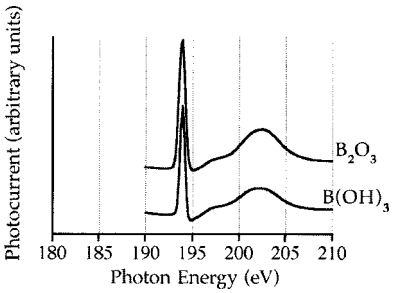

FIG. 4. Boron *K* edge XANES of boron oxide B_2O_3 and boric acid $B(OH)_3$. The structures of these compounds are similar (boron is trigonally coordinate with oxygen in both cases) giving indistinguishable spectra. Spectra acquired in SRC User's Chamber on Mk V Grasshopper beamline.

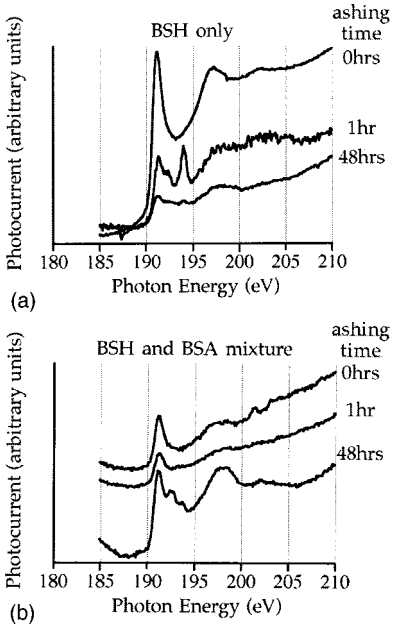

FIG. 5. Boron *K* edge XANES of reference 2 μg BSH samples ashed for up to 48 h in a cold oxygen plasma. (a) Ashing pure BSH crystals. (b) Ashing BSH in a protein matrix [1 μg bovine serum albumin (BSA)]. Spectra acquired in the MEPHISTO chamber on 6 m TGM beamline.

never develops strongly, and the additional peak at 192.5 eV appears after 12 h, remaining until 48 h.

These data suggest that the BSH cage is attacked during ashing to form boron oxide. However, boron oxide was observed to be volatile in vacuum (and in air above 100 °C). The reduction in the strength of the oxide peak, and the overall boron signal then indicates that boron (as the oxide) might be removed from the sample, either during ashing, or later under vacuum. A protein matrix appears to stabilize the BSH molecule, however, as the line shape and relative intensities of the boron XANES spectra in Fig. 5(b) show much less oxidation. Note that a parallel series of carbon spectra was acquired (not shown) and after 48 h ashing no carbon was detected.

B. Spectroscopy of boron in human glioblastoma tissue

1. BSH in tissue

The data presented in Sec. I demonstrate the potential difficulties in the detection of trace quantities of boron (as BSH) in tissue by x-ray absorption spectroscopy in MEPHISTO. (1) Ashing of the tissue is required to raise the relative expected boron concentrations for its detection, but this may cause the loss of boron from the sample as the oxide. (2) Sulfur and phosphorus are both interferences in the x-ray energy region of interest. The main concern is with S 2*p* continuum resonances above 187 eV. We have shown that the products of the ashing process are sulfates, and that calcium sulfate gives a smooth signal above 187 eV, which could not be misinterpreted as a B 1*s* signal. Other sulfates may be present in tissues, however, which do have spectral structure in the B 1*s* energy region.

Given these constraints, we studied real tissue samples from brain tumor patients administered with BSH. With reference to the spectra of Figs. 5(a) and 5(b), BSH in ashed tissue should be detected via either the BSH or oxide exciton peaks (at 191.1 and 194 eV), or as a step centered at 190.5 eV [see the 48 h ashing curve in Fig. 5(a)]. Both peaks are narrower than any sulfur component in this region, and are clearly separated from the phosphorus 2*s* signal. If ashing removes both of these peaks the spectra of boron in tissue, however, the remaining absorption step lies very close to the step observed in the sodium sulfate spectrum.

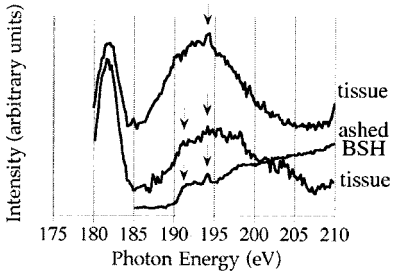

FIG. 6. XANES spectra from ashed tissue containing BSH showed two structures (shown by arrows) that match those in the ashed BSH reference spectra and which are not due to phosphorus or sulfur. The two tissue spectra reported indicate that BSH in tissue may not be oxidized to the same extent between ashed samples as while the top curve exhibits a strong boron oxide peak, the lower curve additionally shows structure at 191 eV. Ashed tissue spectra acquired in the MEPHISTO chamber on 6 m TGM beamline.

MEPHISTO analysis of tissue containing BSH gave spectra containing the signature of ashed BSH as identified by the two features indicated by arrows in Fig. 6. The top tissue spectrum clearly possesses the boron oxide resonance at 194 eV, while the lower tissue spectrum has a shoulder at 191 eV and a weak 194 eV resonance in close agreement with the ashed BSH spectrum included for reference. Neither of these structures was ever seen in control tissue not containing BSH [Fig. 2(c)]. We observe the expected boron features, but also conclude that the extent of oxidation of the BSH molecule due to ashing may vary between samples.

2. An alternative boron chemical state

In approximately 40% of the 130 microscopic areas analyzed across the three tissue samples we found evidence of a boron signal at 188.3 eV. This was reproducible in two different patients and absent from the control case. Figure 7 shows two examples of these results, taken from glioblas-

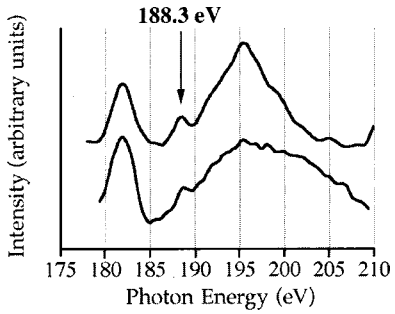

FIG. 7. XANES spectrum of UV/ozone ashed tissue from two human patients which clearly show a peak at 188.3 eV in addition to the contributions from sulfate and phosphate. Spectrum acquired in the MEPHISTO chamber on 6 m TGM beamline.

TABLE I. Frequency table reporting the detection of the 188.3 eV peak from sections from three patients. Each count represents one unique tissue area from which an x-ray absorption spectrum in the boron 1*s* energy range was acquired. The notation *vWf* in the second column indicates that the tissue had been stained against van Willebrandt factor.

Patient and Sample(s)	Sectioning	Staining	No. of regions with 188.3 eV peak	No. of regions with no 188.3 eV peak
DS 1 (control)	microtomed	unstained	0	7
JU U1–U4	ultramicrotomed	unstained	3	10
JU 265	microtomed	*vWf*	8	10
JU 268	microtomed	*vWf*	14	17
FR 41	microtomed	unstained	12	49

toma tissue from patient JU, section 265 (top curve) and from patient FR, section 41 (bottom curve). In this spectrum, in addition to the sulfur and phosphorus contributions seen previously (the P 2*s* peak is very weak in the lower curve), there is a sharp peak at 188.3 eV. This peak is too sharp to be a sulfur 2*p* high-energy resonance, and has never been seen in the absorption spectra of sulfur compounds studied by our or other groups [25]. It is also too low in energy to be associated with the phosphorus 2*s* peak, and could not be attributed to higher diffraction order structures from the beamline or other artifacts associated with the x-ray beam. Only boron could give a peak at this energy, although it is in a reduced oxidation state compared to boron in BSH. It is commonly observed in both x-ray absorption and photoemission spectroscopy that core level energies can increase as oxidation number increases. The oxidation-induced withdrawal of valence electrons that penetrate into the atom reduces nuclear charge screening and therefore increases the binding energies of core levels. In the present case, boron appears to be reduced, as the 188.3 eV B 1*s* binding energy is lower than in boron oxide or BSH.

The x-ray absorption spectra of many boron compounds were acquired to investigate the origin of this signal, but so far we did not observe any boron absorption features below 189 eV. Nevertheless, a boron 1*s* peak is the only reasonable description of this signal. A review of the literature pertaining to boron x-ray absorption spectroscopy revealed one possible interpretation. McLean *et al.* formed a subsurface layer of boron in an annealed silicon wafer heavily doped with boron [26]. Boron in this sample had a peak at 188.6 eV in the absorption spectrum.

It is unlikely that we have reproduced the physical situation reported by McLean *et al.*, which would have required boron atoms to diffuse past the top silicon layer. In addition, we do not expect *a priori* that the underlying silicon substrate on which the tissue samples are placed should be spectroscopically visible in MEPHISTO, as the probing depth is less than 100 Å. However, McLean's result demonstrates that boron in a reduced chemical state can have x-ray absorption peaks at lower energies than BSH and the other compounds studied. Boron may be bonded to one or more other elements physiologically present in the tissue that generate a boron chemical state with the observed peak at 188.3 eV. We have not yet identified this compound, but the results of McLean *et al.* prove that it is plausible.

Another possible interpretation for the appearance of the peak at 188.3 eV is that boron in BSH is reduced under x-ray illumination during the MEPHISTO experiments. To exclude this possibility, we carefully analyzed BSH in the presence or absence of albumin, before and after ashing. The results are presented in Figs. 5(a) and 5(b) and discussed in **A**. In none of these cases did such a structure appear under illumination.

These experiments also demonstrate that the formation of the 188.3 eV peak cannot have occurred during the ashing procedure, as a result of ionization and subsequent reaction of boron with other physiological elements, provided in this test by albumin. The presence of the 188.3 eV peak cannot be a consequence of the presence of nickel in the tissue, as it has been observed in samples from two patients, both containing and not containing nickel. Ni 2*p* peaks are at 853 and 870 eV, and Ni 3*p* peaks are at 66 and 68 eV, very far from 188.3 eV and therefore without interference in this energy region. Table I summarizes the frequency with which this signal was observed. The boron signal at 188.3 eV was not seen everywhere in the FR and JU cases. This suggests that the boron distribution in tumor, following administration of BSH, is inhomogeneous.

The existence of a boron absorption peak at 188.3 eV, and the absence of BSH spectral features suggests that a change in the chemical state of boron has occurred *in vivo*. Such a peak could be interpreted as an artifact introduced by the ashing procedure, but we have shown that oxidation of BSH leads to higher energy features. This is true also when BSH is ashed in the presence of albumin. Another possible cause could be photoreduction in the synchrotron beam, although photochemistry was never observed in reference BSH depositions on silicon, even in the presence of albumin. The only hypothesis that is not contradicted by the experimental results is the chemical modification of the BSH anion *in vivo*.

3. Microlocalization of boron signals in tissue

The tissue section JU 265 was accompanied by a neighboring tissue section on a glass slide that was double stained against van Willebrandt factor (to locate blood vessel endothelia) and against molecular BSH. The results of the anti-BSH staining showed both a diffuse positive staining throughout some tissue areas (a small fraction of the total tissue area, with typical dimensions of $100\times400\,\mu$m) and small localized denser spots having a diameter of 5–10 microns, in the same areas. Positive staining against BSH oc-

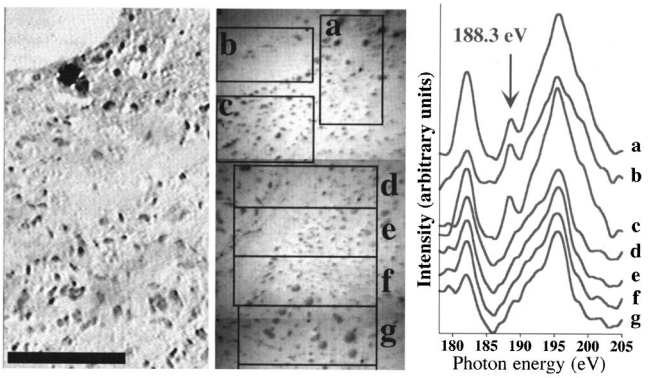

FIG. 8. Left. (Patient JU, section 269) optical micrograph of human glioblastoma section mounted on a glass slide and double stained against van Willebrandt factor and BSH. A diffuse positive stain for BSH was developed at the lower edge of the gap in the tissue. The scale bar (black, at bottom) = 100 μm. Center. (Patient JU, section 265) composite MEPHISTO photoelectron micrograph of the equivalent tissue area to that shown on the left. The area studied corresponds to the most darkly stained region of tissue seen in the left image, at the edge of the gap, and moving down the tissue away from the edge. The photon energy was 139 eV. Right. X-ray absorption spectra were acquired in each one of the boxes indicated in the center micrograph. Note that the regions (a)–(c) which show most strongly the B 1*s* peak at 188.3 eV correspond to the regions that showed positive staining against BSH.

curred only in well vascularized areas (as proven by the staining against van Willebrandt factor) although not all stained blood vessels could be associated with BSH penetration into the tumor.

The 188.3 eV boron species was observed only in the tissue areas that were well vascularized and which gave positive anti-BSH staining. Absorption spectra from these areas showed too much phosphorus interference to clearly characterize the BSH distribution with MEPHISTO. The 188.3 eV peak is clearly separated from the P 2*p* peak, however, and could be traced through the tissue as demonstrated by Fig. 8.

The image on the left of Fig. 8 is an optical micrograph (patient JU, section 269) showing the positive stain (blue in the original image, a darker gray in this version) against BSH at the border of a gap in the tissue. This gap was seen in several consecutive tissue sections, and so is not an artifact of the sectioning process. The equivalent tissue region was studied in MEPHISTO on section 265 (that is, a section that was taken by microtomy from the same tissue block four sections (28 μm) before the section for VLM imaging). A composite image constructed from photoelectron micrographs (acquired with a photon energy of 139 eV, the maximum of the P 2*p* absorption) is shown at the center of Fig. 8. The boxes in this image represent the acquisition areas from which the correspondingly labeled absorption spectra reported on the right were acquired. There is a gradual modulation in the 188.3 eV peak intensity over the $100\times400\ \mu m^2$ region of this image.

In previous studies, positive staining against BSH was observed in localized spots similar to those found in our cases, JU and FR [17]. Double stained samples against BSH and Ki-67, a protein found in the nuclei of proliferating cells, showed examples in which both stains overlapped at some regions, indicating that BSH is actually accumulated in some nuclei. This result has also been published independently by secondary ion mass spectrometry (SIMS) [12]. A motivation of the analysis of these tissue samples with spectromicroscopy is to investigate whether the immunohistochemical stainings for the optical microscope do show that BSH is accumulated inside nuclei. At present, the very weak boron signal in MEPHISTO (at 188.3, 191, or 194 eV) does not allow a direct comparison with the results of immunohistochemical staining.

V. CONCLUSIONS

The work presented here represents the first systematic application of chemical analysis with XANES spectroscopy to human tissue samples. The specific aim of this work is to discover the microdistribution and chemical state of boron in human tissue samples treated with BSH for BNCT. We have shown that the products of tissue ashing can be identified by comparing near edge structure in the x-ray absorption spectra from ashed tissue with those from reference compounds. Physiological elements which are not removed by ashing (sulfur and phosphorus) can act as interferences for boron, but the spectra we have acquired on control and reference samples allow us to identify a small signal in a real tissue sample which can be unambiguously interpreted as ashed BSH.

Samples of human glioblastoma tissue from two patients administered with BSH and one patient not administered with BSH were analyzed in the MEPHISTO spectromicroscope. A spectroscopic analysis of microscopic tissue regions discovered a weak BSH signal. Boron was found in a reduced chemical state (with respect to boron in BSH) as shown by the x-ray absorption peak at 188.3 eV. This peak was found across 40% of the tissue regions analyzed and never from the control patient. The tissue samples analyzed in MEPHISTO were prepared in parallel with a nearby section mounted on a glass slide and stained anti-BSH for VLM analysis. The reduced boron species was found in tissue in the same general areas which stained positive for BSH in VLM. The x-ray absorption feature at 188.3 eV could not be produced by ashing, nor with x-ray induced photochemistry. A proportion of the BSH injected into the patient must, therefore, have been bound or metabolized *in vivo*. The remaining proportion was not metabolized, and was immunohistochemically stained, but was only weakly detectable in MEPHISTO after ashing, and suffered interference from the phosphorus signal.

In conclusion, the present work presents evidence of *in vivo* metabolism of BSH to a different chemical state. The boron compound formed has not been yet identified, but it is plausible that BSH cage is opened *in vivo* or binds another element or molecule physiologically present in the tissue.

ACKNOWLEDGMENTS

This work was supported by the Fonds National Suisse de la Recherche Scientifique, the Consiglio Nazionale delle Ricerche, the Ecole Polytechnique Fédérale of Lausanne, Deutsche Forschungsgemeinschaft, Fonds der Chemischen Industrie and the Biomed Program of the European Commission. We thank Professor B. P. Tonner for his in-

valuable collaboration in the design and construction of the MEPHISTO electron optics and data acquisition system, and for their continuous improvement. We benefited greatly from the professional assistance of Roger Hansen, Dan Wallace, Mary Seversen, Mark Bissen, and all the staff of the SRC (a national facility supported by the NSF under Grant No. DMR-95-31009). We also thank Roger Hansen for use of the UV/ozone cleaning oven for the ashing of tissue samples, and Takashi Suda for use of the oxygen plasma oven.

[1] F. B. Furnari, H.-J. Su Huang, and W. K. Cavanee, Cancer Surv. **25**, 233 (1995).
[2] G. L. Locher, Am. J. Roentgenol. **36**, 1 (1936).
[3] R. F. Barth, A. H. Soloway, R. G. Fairchild, and R. M. Brugger, Cancer **70**, 995 (1992).
[4] A. H. Soloway, in *Advances in Neutron Capture Therapy*, edited by A. H. Soloway, R. F. Barth, and D. E. Carpenter (Plenum, New York, 1993).
[5] A. H. Soloway, H. Hatanaka, and M. A. Davis, J. Med. Chem. **10**, 714 (1967).
[6] H. Hatanaka and Y. Nakagawa, Int. J. Radiat. Oncol. Biol. Phys. **28**, 1061 (1994).
[7] D. Gabel, in *Progress in Neutron Capture Therapy for Cancer*, edited by B. J. Allen (Plenum, New York, 1992).
[8] D. Haritz, D. Gabel and R. Huiskamp, Int. J. Radiat. Oncol. Biol. Phys. **28**, 1175 (1994).
[9] A. H. Soloway, W. Tjerks, B. A. Barnum, F.-G. Rong, R. F. Barth, I. M. Codogni, and J. G. Wilson, Chem. Rev. **98**, 1515 (1998).
[10] C. P. Ceberg, A. Persson, A. Brun, R. Huiskamp, A.-S. Fyhr, B. R. R. Persson, and L. G. Salford, J. Neurosurg. **83**, 86 (1995).
[11] D. Haritz *et al.*, in *Boron-Neutron Capture Therapy: Towards Clinical Trials of Glioma Treatment*, edited by D. Gabel and R. Moss (Plenum, New York, 1992).
[12] K. Haselsberger, H. Radner, W. Gössler, C. Schlagenhaufen, and G. Pendl, J. Neurosurg. **81**, 714 (1994).
[13] G. De Stasio, M. Capozi, G. F. Lorusso, P.-A. Baudat, T. C. Droubay, P. Perfetti, G. Margaritondo, and B. P. Tonner, Rev. Sci. Instrum. **69**, 2062 (1998).
[14] W. Gudat, and C. Kunz, Phys. Rev. Lett. **29**, 169 (1972).
[15] G. De Stasio and G. Margaritondo, in *Spectromicroscopy with VUV Photons and X-Rays*, special issue of J. Electr. Spectr. Relat. Phenom., edited by H. Ade (Elsevier, Amsterdam, 1997).
[16] B. Gilbert, J. Redondo, P.-A. Baudat, G. F. Lorusso, R. Andres, E. G. Van Meir, J.-F. Brunet, M.-F. Hamoud, T. Suda, Delio Mercanti, M. T. Ciotti, T. C. Droubay, B. P. Tonner, P. Perfetti, G. Margaritondo, and Gelsomina De Stasio, J. Phys. D **31**, 2642 (1998).
[17] B. Otersen, D. Haritz, F. Grochulla, M. Bergmann, W. Sierralta, and D. Gabel, J. Neuro-Oncol. **33**, 131 (1997).
[18] *Immunocytochemistry: A Practical Approach*, edited by J. E. Beesley (IRL, Oxford 1993).
[19] G. De Stasio, M. Capozi, T. C. Droubay, D. Mercanti, M. T. Ciotti, G. F. Lorusso, R. Andres, T. Suda, P. Perfetti, B. P. Tonner, and G. Margaritondo, Anal. Biochem. **252**, 106 (1997).
[20] F. J. Esposto, P. Aebi, T. Tyliszczak, A. P. Hitchcock, M. Kasrai, J. D. Bozek, T. E. Jackman, and S. R. Rolfe, J. Vac. Sci. Technol. A **9**, 1663 (1991).
[21] G. De Stasio, B. Gilbert, L. Perfetti, R. Hansen, D. Mercanti, M. T. Ciotti, R. Andres, P. Perfetti, and G. Margaritondo, Anal. Biochem. **266**, 174 (1999).
[22] G. De Stasio, L. Perfetti, B. Gilbert, O. Fauchoux, M. Capozi, P. Perfetti, G. Margaritondo, and B. P. Tonner, Rev. Sci. Instrum. **70**, 1740 (1999).
[23] M. Kasrai, W. N. Lennard, R. W. Brunner, G. M. Bancroft, J. A. Bardwell, and K. H. Tan, Appl. Surf. Sci. **99**, 303 (1996).
[24] M. Kasrai, J. R. Brown, G. M. Bancroft, Z. Yin, K. H. Tan, and X. Feng, Int. J. Coal Geol. **32**, 107 (1996).
[25] M. Kasrai, Z. Yin, and G. M. Bancroft, J. Vac. Sci. Technol. A **11**, 2694 (1993).
[26] A. B. McLean, L. J. Terminello, and F. J. Himpsel, Phys. Rev. B **41**, 7694 (1990).

D: Determination of the subcellular distribution of Mercaptoundecahydro-*closo*-dodecaborate (BSH) in human glioblastoma multiforme by electron microscopy

Submitted for publication to the European Journal of Cancer

Determination of the subcellular distribution of Mercaptoundecahydro-*closo*-dodecaborate (BSH) in human glioblastoma multiforme by electron microscopy

Michael Neumann[1], Ulrike Kunz[2], Heiner Lehmann[2] and Detlef Gabel[1]

[1]Department of Chemistry, University of Bremen
Leobener Straße, P. O. Box 330 440, D-28334 Bremen, Germany
Tel.: +49 (0)421 2182200
Fax: +49 (0)421 2182871
gabel@chemie.uni-bremen.de

[2]Institut für Tierökologie und Zellbiologie, Tierärztliche Hochschule Hannover, Germany

ABSTRACT:

The subcellular distribution of mercaptoundecahydro-*closo*-dodecaborate (BSH) in glioblastoma multiforme tissue sections of several patients having received BSH prior to surgery was investigated by transmission electron microscopy (TEM) using antibodies against BSH and electron energy loss spectroscopy (EELS) and electron spectroscopic imaging (ESI). These microscopic techniques show that BSH is associated with extracellular structures, the cell membrane as well as with the chromatin in the nucleus.

KEY WORDS:

BSH, transmission electron microscopy, ESI/EELS technique, glioblastoma multiforme, immunohistochemistry.

INTRODUCTION:

Boron neutron capture therapy (BNCT) is a radiation therapy to destroy tumor cells while minimizing damage to healthy tissue. It is based on the nuclear reaction that occurs when boron-10 is irradiated with low-energy neutrons. The ^{10}B-nucleus undergoes a neutron capture reaction and disintegrates into two fission particles ($^{10}B(n,\alpha)^{7}Li$) (Taylor et al., 1935) with a range of approximately one cell diameter (Northcliffe and Schilling, 1970). When these particles hit cell nuclei they can cause severe damage which lead to cell death. For a successful treatment, accumulation of boron in tumor to a larger extent than in the surrounding tissue is necessary. Two boron compounds, BSH ($Na_2B_{12}H_{11}SH$) and L-4-dihydroxy-borylphenylalanine (BPA), are currently being used clinically as capture agents for glioblastoma multiforme and melanomas (Hawthorne 1998). The localization of boron-10 on a subcellular level has a great influence on the biological effectiveness of BNCT (Kobayashi and Kanda, 1982; Gabel et al., 1987).

BSH has been established as a suitable boron carrier and has been used by Hatanaka et al. since 1968 with encouraging success (Hatanaka and Nakagawa, 1994). Despite of the long use of BSH in BNCT little is known about its distribution within the tumor cell. Furthermore, different studies with various methods have shown different results for the localization of BSH. Amano (1986) was the first to describe the localization of BSH on a subcellular level; he investigated the boron distribution in brain tumors from BSH-infused patients by neutron-induced α-auto-radiography. He found that the boron content near the nuclear membrane was more than four times higher than for the rest of the tissue. The distribution of BSH was also investigated through laser microprobe mass analysis of glioblastoma material by Haselsberger et al. (1994). When boron could be detected, it was localized within the nuclei. Boron outside of nuclei could not be detected (detection limit approx. 10 ppm). Ceberg et al. (1995) measured boron in subcellular fractions of BSH-infused astrocytoma tissue. By atomic emission spectroscopy (AES) they found 21% of boron in the nuclei, while an additional 18% sedimented with the fraction consisting of cell organelles. Sixty-one percent of boron was found in the soluble fractions. Using immunhistochemistry Otersen et al. (1997) detected BSH in the cytoplasm and in nuclei, with a correlation between the amount of BSH in the nuclei and time between infusion and tumor sampling. The methods used in these studies either did not have the high resolution or the sensitivity necessary for a clear evaluation of the subcellular BSH distribution after cell uptake.

In this study we used two high-resolution microscopic methods for direct and indirect detection of boron. Identifying the subcellular distribution of BSH in tumor tissue is of crucial importance for dosimetric calculations as well as for improving the effectiveness of BNCT, because a nuclear localization of ^{10}B-atoms would greatly increase the selective therapeutic effect caused by the $^{10}B(n,\alpha)^{7}Li$ reaction.

MATERIALS AND METHODS:

Origin of tumor material:

Tumor material was collected in a pharmacokinetic study aimed at identifying optimal time point and dosage of BSH. Tissue samples were taken from glioma patients (grade IV, glioblastoma multiforme), which had received BSH prior to surgery in the Zentralkranken-haus St. Jürgenstraße (Bremen, Germany). Intravenous infusions (40 - 102 mg BSH/kg body weight) were carried out for one hour, 14 to 22 hours before operation (Haritz et al., 1994). After surgery, the material was frozen rapidly and stored at –18 °C.

Pat. code	Age/sex	Infused mg ^{10}B/kg body weight	Average ^{10}B tumor concentration [ppm]
FJ	56/m	55.9	74.8
GO	59/f	21.1	0.5
HO	71/m	31.3	84.2
JU	33/m	28.1	12.2

Table 1: Data of the patient from whom tumor tissue was investigated in this study.

Tissue preparation:

Fixation was carried out in 10 % buffered formalin for 16 h at room temperature (rt). Previously it had been shown that this treatment does not remove boron from this tissue (Otersen et al., 1996). The tissue was dehydrated in increasing concentrations of ethanol. Afterward, the material was incubated in ethanol with increasing content of LR White (London Resin Company, England) up to 100 %. Polymerization was performed by addition of small amounts of fastener (catalyst) at rt. Ultra-thin sections (50-70 nm) were cut and mounted on nickel-grids (300 - 600 mesh).

Antibody preparation:

At the Institut für Tierzucht und Tierverhalten, Mariensee, Germany a goat was immunized with BSH, which was linked through sulfhydryl groups to bovine serum albumin (BSA). The resulting serum was freed from antibodies directed against BSA by affinity chromatography over a column of BSA bound to Sepharose.

Immunogold labeling for transmission electron microscopy:

The tissue sections were rehydrated in ethanol (90 % and 70 %) and bidistilled water. After blocking with normal rabbit serum the slides were incubated with the antibody against BSH for 20 h at rt. After washing in PBS-Tris-buffer (pH 7.4) the grids were exposed to a gold-labeled anti-goat secondary antibody (Nanoprobes Inc., USA) (1:200) for 20 h at rt followed by silver enhancement (HQ silver, Nanoprobes Inc., USA) for 15 min. For image acquisition a transmission electron microscope (EM 10, Zeiss, Germany) and an acceleration voltage of 60 kV was used.

EELS/ESI:

Element analysis of untreated sections using electron energy loss spectroscopy (EELS) and electron spectroscopic imaging (ESI) were performed with an energy filtering transmission electron microscope CEM 902 operated at 80 kV (Zeiss, Germany). In the first method (EELS) the element composition from selected areas can be measured using a photomultiplier detector system. The measurements were performed at a magnification of 30000x and a filter entrance aperture of 100 µm in diameter, that means the diameter of the analyzed area was about 370 nm. The characteristic energy losses used were the 186 eV-edge for detecting boron and the 164 eV-edge for detecting sulfur. Elemental maps were calculated with an image processing system (Kontron, Germany) based on the Two-Window-Method (Probst and Bauer 1987; Lehmann et al. 1990), following the instructions of the “Handbook of Standard Data for Identification and Interpretation of Electron Energy Loss Spectra and for Generation of Electron Spectroscopic Images” (Reimer et al 1992).

RESULTS:

TEM:

The tumor material available for this study was originally prepared for light microscopy. Due to suboptimal freezing and storage for electron microscopy the tissue material was morphologically in bad condition. Organelles could rarely be found with exception of nuclei. Because of the unique study from which these samples were obtained no other BSH-containing tumor material was available and the investigations were performed on these samples.

The subcellular distribution of BSH was similar in the investigated tissue samples of all patients. Fig. 1 shows a photograph of a tissue section visualized by immunogold-labeling. BSH could be detected in large amounts. This confirms earlier reports that the compound must be strongly bound inside the cell (Ceberg et al., 1995; Otersen et al., 1996). BSH is located predominantly near the cell membrane, the nuclear membrane and also within the nuclei. In case of the plasma membrane, BSH seems to adhere to the extracellular part in intercellular structures, which are visualized also by contrasting with uranium acetate and lead citrate (Fig. 2). BSH found near the nuclei on the other hand seems to be located on the intranuclear side of the nuclear membrane associated with an electron dense structure, possibly heterochromatin (Fig. 3). The nonuniform distribution suggests an interaction of BSH with molecules inside the nucleus. Due to the double negative charge an ionic interaction can be assumed. Potential partners for electrostatic interactions are proteins with a high amount of lysine or arginine such as histones (Cooper et al., 2000) or lamine (Lin and Worman, 1995; Pollard et al., 1990; McKeon et al., 1986; Fisher et al., 1986).

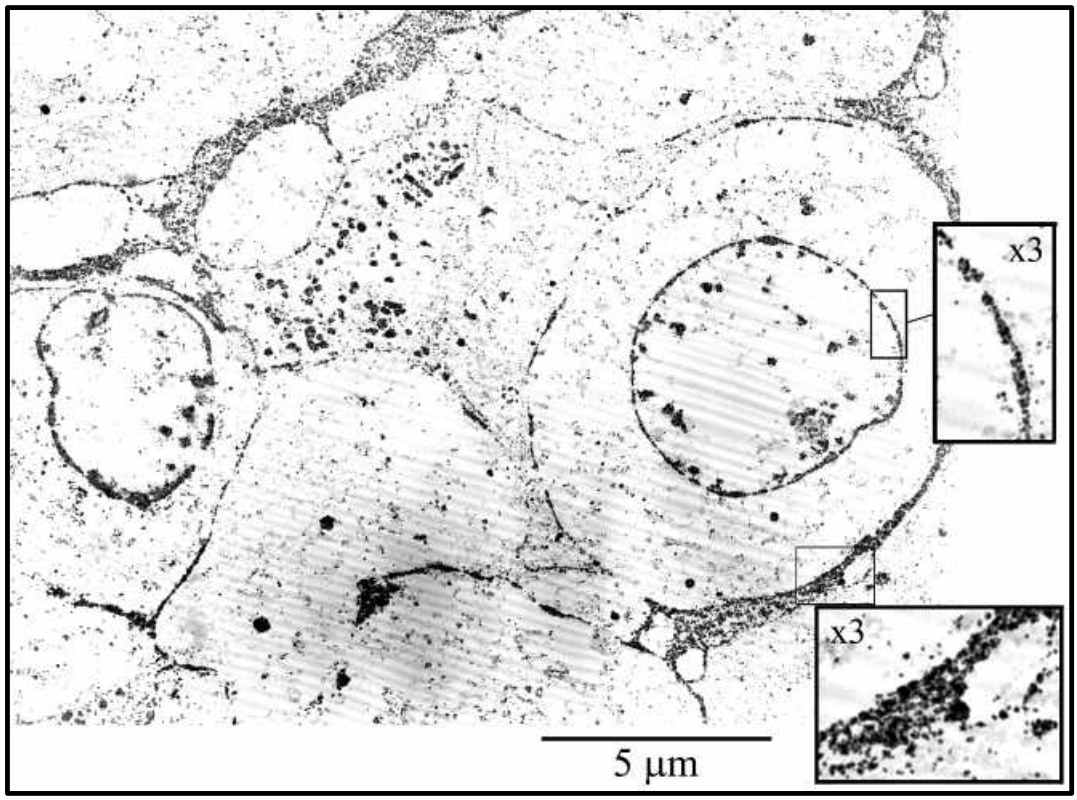

Fig. 1: Electron microscopic photograph of a tissue section of patient HO. Black structures are stained for BSH whereas the tissue is visible as light gray. Insets are shown with a three times higher magnification. Staining of cell and nuclear membrane is prominent. Most BSH is located intercellular space near the cell membranes.

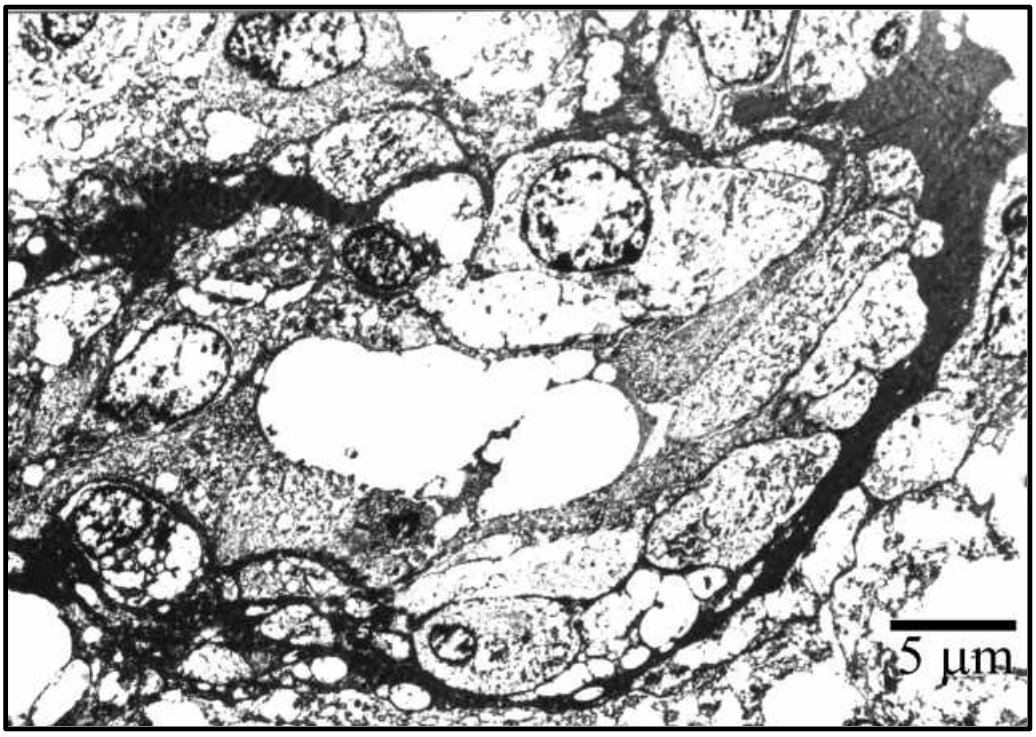

Fig. 2: Tissue section from patient HO contrasted by uranium acetate and lead citrate. Noticeable is the wide, strongly contrasted intercellular space with bubble like inclusions.

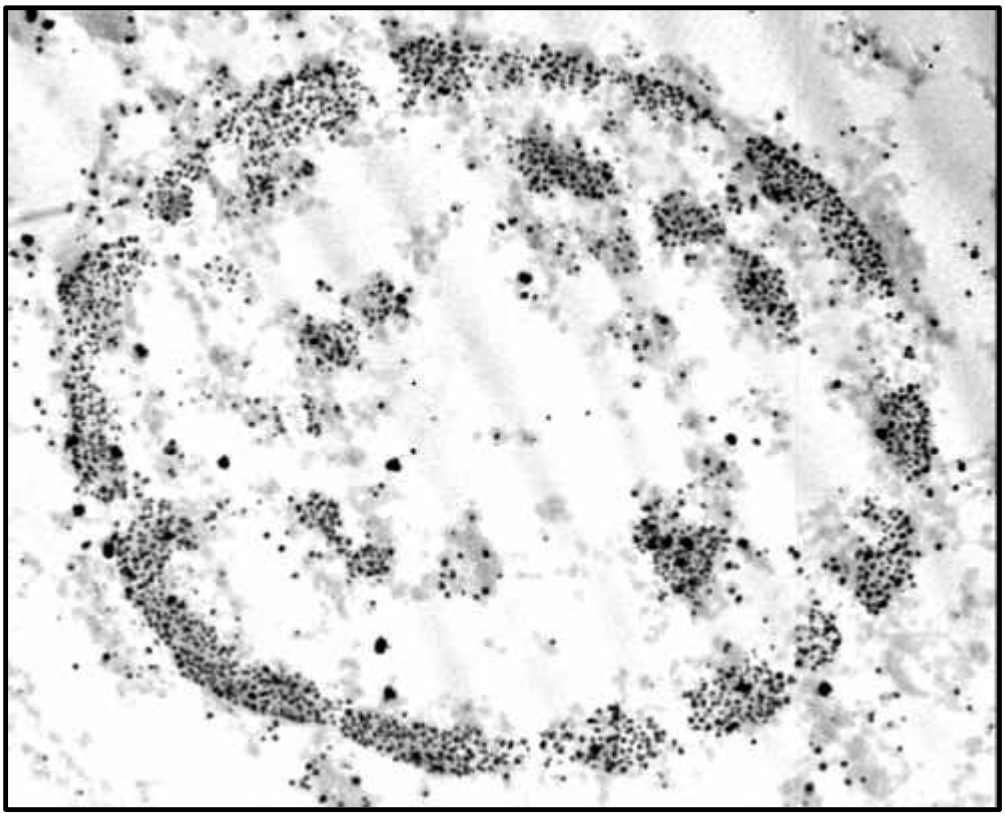

Fig. 3: Patient FJ: Photograph of a nuclear region. BSH visualized with gold particle labeled antibodies and enhanced with silver. BSH is located in clusters and only in regions with electron dense structures.

EELS/ESI:

EELS records the energy loss of beam electrons which occurs through inelastic scattering. The amount of energy loss is characteristic for each element. The data can also be used to obtain electron spectroscopic images (ESI).

Fig. 4 is a transmission electron microscopic photograph of a nucleus in an untreated tissue section. The electron spectroscopic images of boron of this nucleus are shown in Fig. 5. Also in Fig. 5 are the corresponding background stripped electron energy loss spectra (EELS) of the marked regions in panel d. The first peak in the spectra is due to sulfur (S-L2 edge) whereas the second peak marks boron (B-K edge). In dark regions of the element-specific image no boron is located whereas in the bright regions it is. In correspondence with the TEM results BSH could only found inside the nucleus near the nuclear membrane and in electron dense clusters in the nucleoplasmic space.

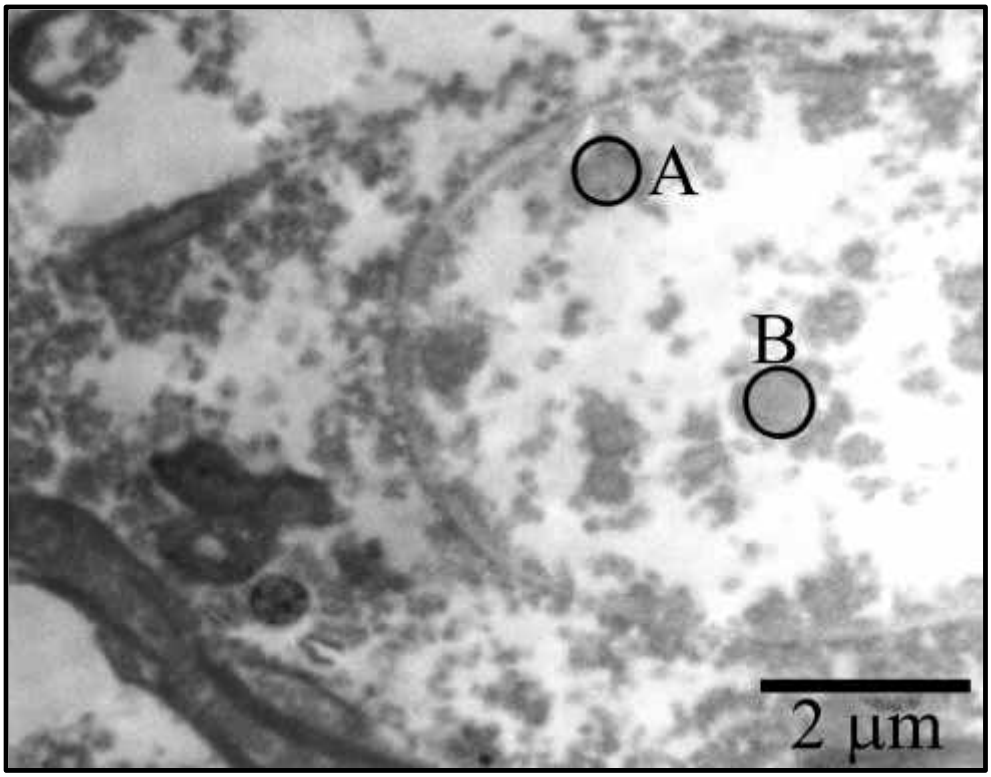

Fig. 4: Patient HO: Unstained nucleus. Two areas of the heterochromatin are marked for further experiments with EELS/ESI.

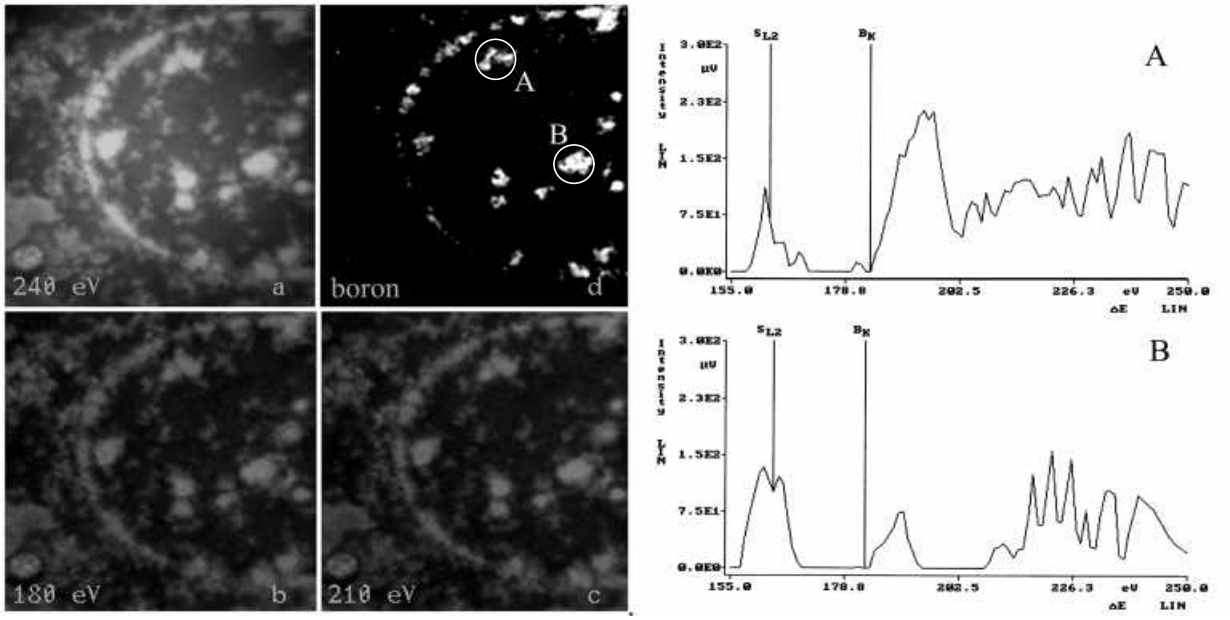

Fig. 5: Left: Electron spectroscopic image of boron obtained by EELS. Same nucleus as in Fig. 4. Panel a: control image; b: element-specific baseline or background image; panel c: element-specific peak image and d: "net" element-specific image which was obtained by subtraction of image b from c. Right: Corresponding spectra for the regions marked in panel d.

There exists a possibility that due to the relative proximity of the S-L2 edge for sulfur (164 eV) and the B-K edge for boron (186 eV) the structures visible in boron ESI derive not from boron, but rather from sulfur. To exclude this two ESI images of these elements were compared (Fig. 6). The used window settings were 180 eV to 210 eV ("boron") and 160 eV to 200 eV ("sulfur"). Due to the absorption edges for boron at 186 eV and sulfur at 164 eV, boron is visible in the "sulfur"-ESI but sulfur should not be visible in the "boron"-ESI. Therefore the "sulfur"-ESI in Fig. 6 shows the distribution of sulfur and boron, whereas the "boron"-ESI in Fig. 6 is originated only by boron. Important is the fact that there are regions positive in the "sulfur"-ESI which are negative in the "boron"-ESI. This proves that sulfur is not visible within the window widths of the electron specific images for boron used in this study. Phosphorus as the most common element in nuclei after carbon has an adsorption edge (P-L2 edge) of 129 eV and cannot interfere with the boron signal (Friel, 1995).

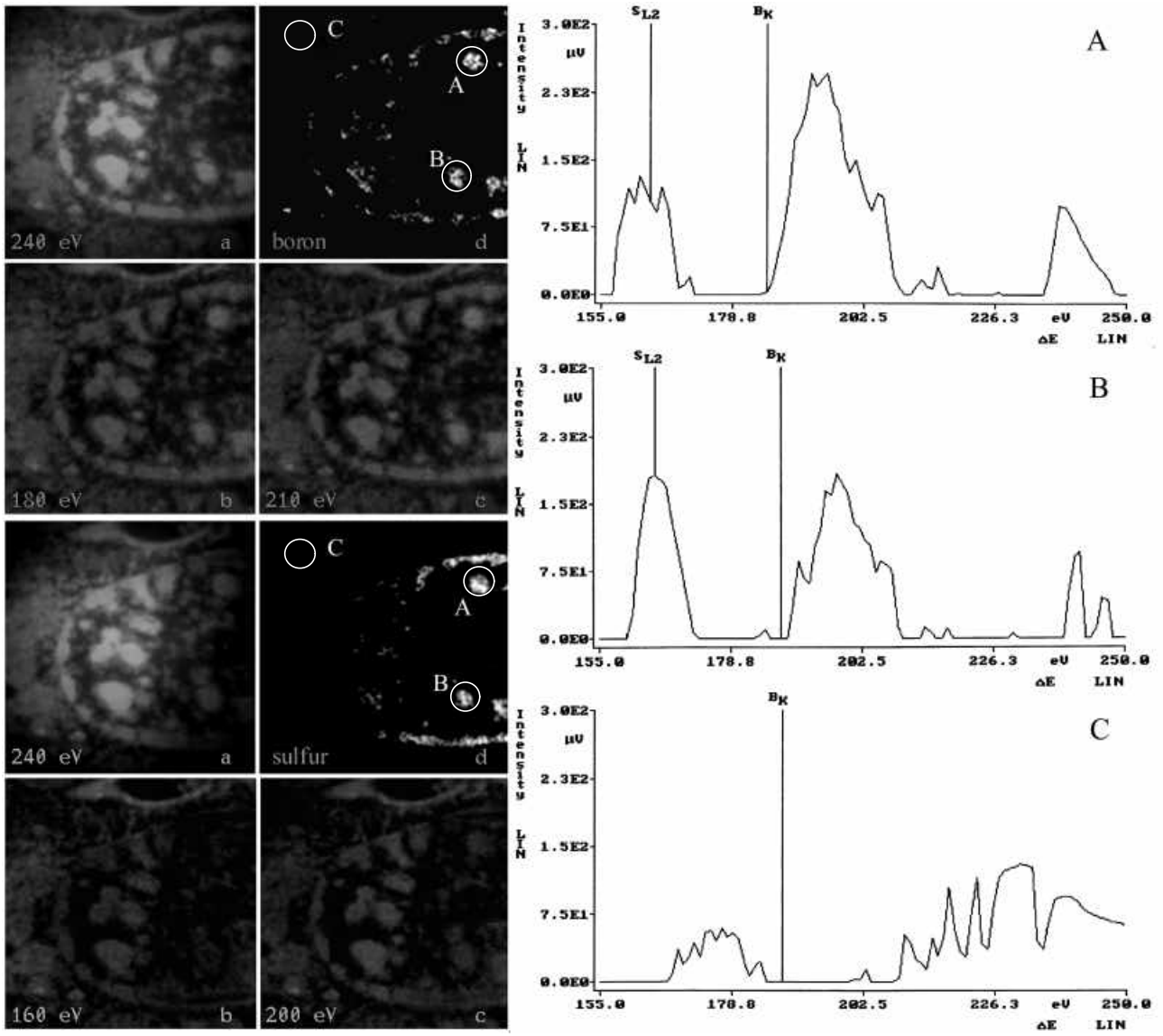

Fig. 6: Patient HO: Electron spectroscopic image and EELS of boron and sulfur of a perinuclear region. The distribution of sulfur is similar but not equal to boron. Especially the nuclear membrane contains different regions with deposits of sulfur and boron.

Because of the bad morphological conditions of the tissue organelles could rarely be found with exception of nuclei. To answer the question whether the BSH accumulation near the cell membrane and the nuclear membrane is selective for these structures or whether BSH accumulates in all remaining structures with high electron density two ESI-images were made from two high-density regions on the same grid (Fig. 7 and 8). It is clearly visible that there is much more boron in the nuclear region. This shows that the presence of BSH does not correlate to the electron density.

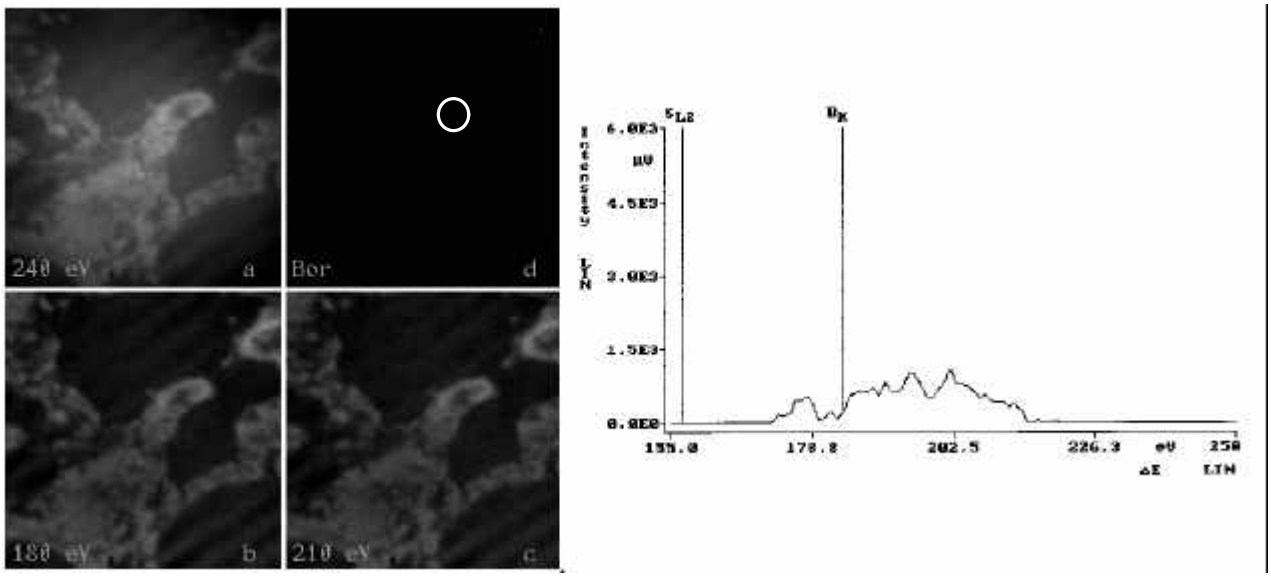

Fig. 7: Electron spectroscopic image and EELS of boron from a nuclear region (patient FJ).

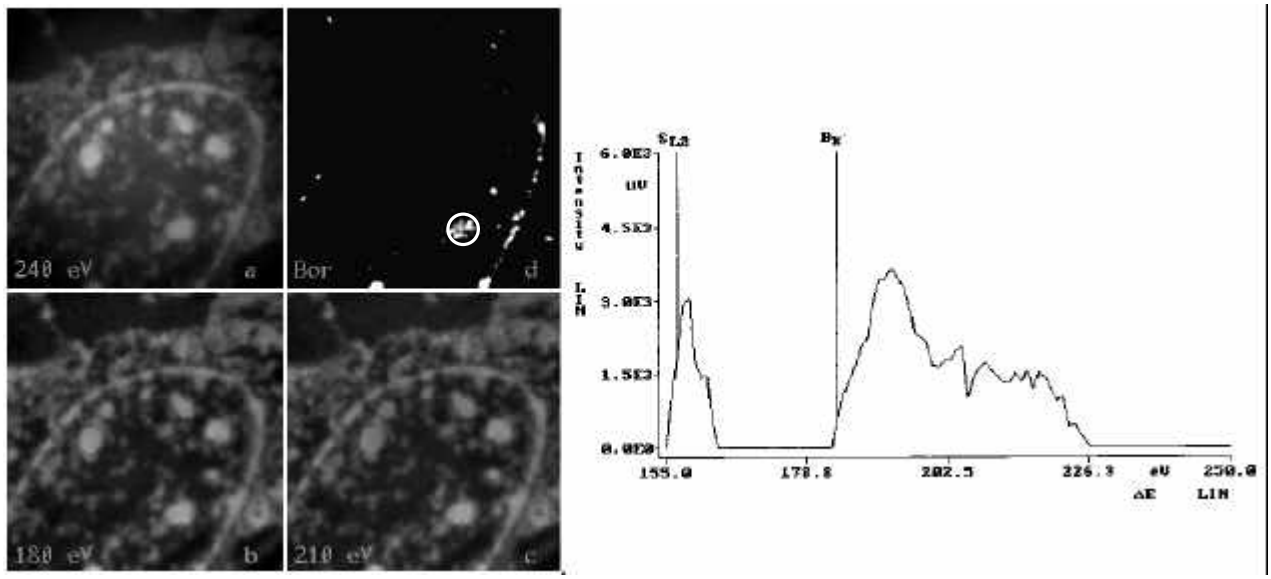

Fig. 8: Electron spectroscopic image and EELS of boron from an electron dense non-nuclear region from the same grid as in Fig. 7.

DISCUSSION:

In this study we could detect BSH by immunogoldlabeling. This confirms that BSH is strongly bound to the tissue (Otersen et al., 1996) and had not been removed neither during fixation nor during the staining procedure. If such a strong interaction between BSH and tissue structures exists a displacement of the compound after surgery can be excluded. Due to the fact that the antibodies could recognize BSH no major change of its structure could have occurred in vivo.
The distribution maps obtained by TEM show that BSH is located in electron dense regions within the nucleus, which have a similar appearance as chromatin, and on the extracellular part of the cell membrane. The theoretical detection limit of this method is one BSH-molecule, which is linked by antibodies to one gold particle. This is much lower than the approx. 100 ppm for EELS/ESI. But the later has fewer possibilities for artifacts due to the direct detection method. We used both TEM and EELS in this study to ensure that the obtained results unequivocally represent the real distribution of BSH. Additionally the antibody used to detect BSH has already shown its selectivity in light microscopic studies (Otersen et al., 1997), and therefore unspecific staining is not probable.

It could be demonstrated that the chosen energy window at 210 eV result in electron spectroscopic images that represent only boron. Sulfur has a similar energy of the ionization edge but results in different distribution images. No other element has an adsorption peak near at 200 eV, so that the ESI shown above result unequivocally from boron.

Based on the comparison of two ESI-images, one of a nuclear region and one of a non-nuclear region, a non-selective accumulation of BSH in electron dense structures can be excluded.

The high concentration of BSH near the cell membrane supports the hypothesis that BSH enters the cell by endocytosis (Otersen et al., 1996). Investigations by Lutz et al. (2000) showed an interaction of the double negatively charged BSH with the positive choline head groups of phosphatidylcholine which is enriched in tumor cells in the extracellular part of the membrane (Fulham et al., 1992; Ott et al., 1993). Normal glial cells, glioma cell lines from rat (Bjerknes et al. 1987) and tumor cells show an increased phagocytic activity. As a result of endocytosis, BSH would occur within cells, encapsulated in vesicles rich in phosphatidylcholine. From there, two pathways are possible:

Membrane components involved in the endocytic pathway are disassembled and recycled. In this way, it is possible that BSH remains bound to choline residues that are detached from membranes. Such electrically neutral compound could diffuse through the cell and also

pass nuclear pores. If BSH interacts with components of the chromatin this could lead to an accumulation of boron in nuclei.

BSH containing vesicles fuse with the membrane of the endoplasmatic reticulum and move to the inner nuclear membrane by lateral diffusion. Retention in the inner nuclear membrane could occur as a result of interaction with nucleoplasmic proteins like lamins or chromatin proteins.

In conclusion, the accumulation of BSH within tumor cells of high-grade glioma could be demonstrated by two high-resolution microscopic methods. Within these cells, BSH is located in nuclei and near the cell membrane. In the nuclei BSH seems to be in regions of chromatin like structures.

Recently also photoelectronspectromicroscopic studies showed BSH in the immediate environment of the nucleus (Gilbert et al., 2000).

The local arrangement of boron in tissue plays an important role in the radiobiological effect of the $^{10}B(n,\alpha)^{7}Li$ reaction in BNCT. The Relative Local Efficiency (RLE) which indicates the effectiveness of a given intracellular boron concentration to produce cell death in relation to a uniform distribution throughout the cell was found to be six times higher for boron localization in nucleus (Gabel et al., 1987).

When glioma patients are treated with BNCT using BSH, a high probability of DNA-damage caused by the $^{10}B(n,\alpha)^{7}Li$ reaction can be assumed in those cells accumulating BSH, due to the spatial vicinity of boron to the chromatin.

ACKNOWLEDGEMENTS:

We wish to express our sincere gratitude to Prof. Dr. Reimer Stick for the fruitful discussion.

REFERENCES:

Amano K. Boron-10-mercaptoundecahydrodo-decaborate distribution in human brain tumors as studied by neutron-induced alpha-autoradiography. In Hatanaka H, Eds. Boron Neutron Capture Therapy for Tumors. Nishimura, Niigata, 1986, 107-115.

Bjerknes R, Bjerkvig R, Laerum OD. Phagocytic capacity of normal and malignant rat glial cells in culture. J Natl Cancer Inst 1987, **78**, 279-288.

Ceberg CP, Persson A, Brun A, Huiskamp R, Fyhr A-S, Persson BRR, Salford LG. Performance of sulfhydryl boron hydride in patients with grade III and IV astrocytoma: a basis for boron neutron capture therapy. J Neurosurg 1995, **83**, 79-85.

Cooper AJ, Wang J, Pasternack R, Fuchsbauer HL, Sheu RK, Blass JP. Lysine-rich histone (H1) is a lysyl substrate of tissue transglutaminase: possible involvement of transglutaminase in the formation of nuclear aggregates in (CAG)(n)/Q(n) expansion diseases. Dev Neurosci 2000, **22**, 404-417.

Fisher DZ, Chaudhary N, Blobel B. cDNA sequencing of nuclear lamins A and C reveals primary and secondary structural homology to intermediate filament proteins. Proc Natl Acad Sci USA 1986, **83**, 6450-6454.

Friel JJ. X-ray and image analysis in electron microscopy. Princeton Gamma-Tech, 1995.

Fulham MJ, Bizzi A, Dietz MJ, Shih HH, Raman R, Sobering GS, Frank JA, Dwyer AJ, Alger JR, Di Chiro G. Mapping of brain tumor metabolites with proton MR spectroscopic imaging: clinical relevance. Radiology 1992, **185**, 675-686.

Gabel D, Holstein H, Larsson B, Gille L, Ericson G, Sacker D, Som P, Fairchild RG. Quantitative neutron capture radiography for studying the biodistribution of tumor-seeking boron-containing compounds. Cancer Res 1987, **47**, 5451.

Gilbert B, Perfetti L, Fauchoux O, Redondo J, Baudat P-A, Andres R, Neumann M, Steen S, Gabel D, Mercanti D, Ciotti M, Perfetti P, Margaritondo G, De Stasio G. Spectromicroscopy of boron in human glioblastomas following administration of $Na_2B_{12}H_{11}SH$. Physical Review E 2000, **62**, 1110-1118.

Haritz D, Gabel D, Huiskamp R. Clinical phase-I study of $Na_2B_{12}H_{11}SH$ (BSH) in patients with malignant glioma as precondition for boron neutron capture therapy (BNCT). Int J Radiation Oncology Biol Phys 1994, **28**, 1175-1181.

Haselsberger K, Radner H, Gössler W, Schlagenhaufen C, Pendl G. Subcellular boron-10 localization in glioblastoma for boron neutron capture therapy with $Na_2B_{12}H_{11}SH$. J Neurosurg 1994, **81**, 741-744.

Hatanaka H, Nakagawa Y. Clinical results of long-surviving brain tumor patients who underwent boron neutron capture therapy. Int J Radiation Oncology Biol Phys 1994, **28**, 1061- 1066.

Hawthorne MF. New horizons for therapy based on the boron neutron capture reaction. Molecular Medicine Today 1998, **4**, 174-181.

Kobayashi T, Kanda K. Analytical Calculation of Boron-10 Dosage in Cell Nucleus for Neutron Capture Therapy. Radiation Research 1982, **91**, 77-94.

Lehmann H, Kramer A, Schulz D, Probst W. Preparation of plant material for elemental analysis using ESI and EELS techniques. Ultramicroscopy 1990, **32**, 26-34.

Lin F, Worman HJ. Structural organization of the human gene (LMNB1) encoding nuclear lamin B1. Genomics 1995, **27**, 230-236.

Lutz S, Neumann M, Gabel D. The interaction of $Na_2B_{12}H_{11}SH$ (BSH) with liposomes; Relevance to the cellular BSH uptake. In Proceedings of the 9th International Symposium on Neutron Capture Therapy for Cancer, 2000.

McKeon FD, Kirschner MW, Caput D. Homologies in both primary and secondary structure between nuclear envelope and intermediate filament proteins. Nature 1986, **319**, 463-468.

Northcliffe LC, Schilling RF. Range and stopping-power tables for heavy ions. Nucl Data Tables A 1970, **7**, 233-463.

Otersen B, Haritz D, Grochulla F, Bergmann M, Sierralta W, Gabel D. Binding and immunohistochemical localization of $Na_2B_{12}H_{11}SH$ to tumor tissue of glioma patients in boron neutron capture therapy. In Mishima Y, Eds. Cancer Neutron Capture Therapy, New York, Plenum Press 1996, 627-632.

Otersen B, Haritz D, Grochulla F, Bergmann M, Sierralta W, Gabel D. Binding and distribution of $Na_2B_{12}H_{11}SH$ on cellular and subcellular level in tumor tissue of glioma patients in boron neutron capture therapy. J Neuro-Oncol 1997, **33**, 131-139.

Ott D, Hennig J, Ernst T. Human brain tumors: assessment with in vivo proton MR spectroscopy. Radiology 1993, **186**, 745-752.

Pollard KM, Chan EK, Grant BJ, Sullivan KF, Tan EM, Glass CA. In vitro posttranslational modification of lamin B cloned from a human T-cell line. Mol Cell Biol 1990, **10**, 2164-2175.

Probst W, Bauer R. Technik und biologische Anwendung der elektronenspektroskopischen Abbildung (ESI) und der Elektronen Energie-Verlust Spektroskopie (EELS). Verh. Dtsch. Zool. Ges. 1987, **80**, 119-128.

Reimer L, Zepke U, Moesch J, Schulze-Hillert S, Ross-Messemer M, Probst W, Weimer E. EELSpectroscopy. A Reference Handbook of Standard Data for Identification and Interpretation of Electron Energy Loss Spectra and for Generation of Electron Spectroscopic Images. Carl Zeiss, Oberkochen, Germany, 1992.

Taylor HJ, Goldhaber M. Detection of nuclear disintegration in a photographic emulsion. Nature 1935, **135**, 341.

E: Buffers

Incubation-buffer (pH 7.4)

Per 100 ml ddH_2O

1.6 g	Tris-HCl
2.0 g	Gelatine
0.85 g	NaCl
0.5 g	BSA
0.3 g	Na_2HPO_4
0.15 g	Glycine
0.09 g	KH_2PO_4
0.06 g	Tween 20
0.04 g	NaN_3
0.01 g	TritonX-100

TRIS-PBS (pH 7.4)

Per 7.5 l ddH_2O

60 g	Sodium chloride
20 g	Tris-HCl
10 g	Gelatine
7.4 g	Na_2HPO_4
2.5 g	Glycine
2.15 g	KH_2PO_4
1.25 g	Tween 20
1 g	NaN_3
0.25 g	TritonX-100

Mowiol

25 g	Glycerol
10 g	Mowiol 4-88 (Calbiochem 475904)
1 mg	1,4-Diazabicyclo[2.2.2]octane (DABCO)
2 mg	Sodium iodide
25 ml	ddH_2O
50 ml	0.2 M Tris-buffer (pH 8.5)

The solution was stirred for 12 h at room temperature. After sedimenting the mixture was heated to 50 °C for 10 min. Then the solution was clarified by a 15 min spin at 5000 x g. The supernatant was frozen in small aliquots at –18 °C.

F: Abbreviations

BPA	L-4-dihydroxyborylphenylalanine
BSH	Mercaptoundecahydro-*closo*-dodecaborate (2-)
CSLM	Confocal Scanning Laser Microscopy
ddH_2O	double distilled water
EGF	epidermal growth factor
EGFR	epidermal growth factor receptor
ESI	electron energy loss spectroscopy
GFAP	glial fibrillary acidic protein
GBM	Glioblastoma multiforme
ICP-MS	inductively coupled plasma mass spectrometry
MW	microwave
rt	room temperature
TEM	transmission electron microscopy
vWF	von Willebrand factor
X-PEEM	x-ray photoelectron emission spectromicroscopy